

Multi-Wavelength Identification of Galactic X-ray Sources

by

Reuben S. Gazer

A thesis submitted in partial fulfillment of the requirements for the degree of

Master of Science

Department of Physics
University of Alberta

© Reuben S. Gazer, 2018

Abstract

We explore the production and observation of high energy (X-ray and ultraviolet/UV) radiation in the context of Galactic, compact binary systems. At the end of the stellar lifecycle, a star collapses into one of three *compact objects* (COs) depending on the mass at the time of collapse: a white dwarf (WD), neutron star (NS) or a black hole (BH). These dense, stellar remnants are often found in close orbits ($a \sim R_{\odot}$) with another star whose atmosphere can flow to the CO, releasing massive amounts of gravitational energy in the process. These systems are known as *X-ray binaries* (XRBs) for the complex interaction of the stellar pair and constituent matter manifests in bright X-ray luminosities of $L_X \sim 10^{32} - 10^{42}$ erg/s making them among the brightest X-ray emitters in the sky. The formation and distribution of XRBs is still not fully understood, in part because a homogeneous sample of Galactic XRBs is not yet available due to selection effects biased towards bright and transient sources. The *Galactic Bulge Survey* (GBS) was designed to identify a large, quiescent population and found 1640 unique X-ray sources in 12 square degrees near the Galactic Plane. Most systems are still unclassified, specifically those in dense optical or infrared (IR) fields where the true source of X-ray emission can be visually ambiguous. We avoid this ambiguity for 269 of 1640 systems by using UV

data from *GALEX* to identify the correct optical/IR counterparts, making use of the low *GALEX* surface density (and high correlation with X-ray sources). We then create and model spectral energy distributions for each system. We identify a new group of 15 – 25 likely compact binary systems by their excess UV fluxes and classify ~ 150 GBS systems as nearby, chromospherically-active stars. Finally, we discuss our results in the context of the GBS and suggest future research directions.

Preface

All research in this thesis is original work by Reuben Samuel Gazer, under the supervision of Dr. Craig O. Heinke between September 2015 and November 2017 at the University of Alberta. All of the data used is publicly available online.

"I began to realize how important it was to be an enthusiast in life. If you are interested in something, no matter what it is, go at it full speed. Embrace it with both arms, hug it, love it and above all become passionate about it.

Lukewarm is no good."

Roald Dahl

Acknowledgements

I would like to thank first and foremost Craig O. Heinke for supervising me during this thesis. Craig is a wonderful teacher, and a selfless, kind human being. I would also like to thank the rest of the University of Alberta astrophysics group with specific thank-yous to Eric Koch, Arash Bahramian and Alex & Bailey Tetarenko for programming and general research aid.

Contents

1	Introduction	1
1.1	Ultraviolet & X-ray Radiation in Astrophysics	1
1.1.1	Single Stars	4
1.1.2	Compact Binary Systems	8
1.2	The Galactic Bulge Survey (GBS)	16
2	The Galactic Bulge Survey: a <i>GALEX</i> Ultraviolet Counterpart Catalogue	18
2.1	Introduction	19
2.1.1	The Galactic Bulge Survey: Purpose & Progress	19
2.1.2	SED Fitting the GBS via UV Counterparts	21
2.2	UV Counterparts to the GBS	23
2.2.1	<i>GALEX</i> : Photometry & Astrometry	24
2.2.2	<i>GALEX</i> : Data Collection & Reduction	26
2.2.3	<i>GALEX/Chandra</i> Counterpart Match Algorithm	27
2.2.4	Quantifying the <i>GALEX/Chandra</i> Chance-Match Probability	31
2.3	Optical & Infrared Counterparts to the GBS	34
2.3.1	Data: Optical Counterparts	35
2.3.2	Data: Infrared Counterparts	39
2.3.3	Complementary UV Data: <i>Swift</i> UVOT	41
2.4	Identification of Compact Binaries via the SED	42

2.4.1	SED Modeling and Goodness-of-Fit	42
2.4.2	Multi-Component Modeling: A Bayesian Approach	47
2.5	UV & X-ray Emission of Chromospherically Active Stars	48
2.6	Results & Discussion	54
2.6.1	Chromospherically Active Population	57
2.6.2	Poorly Fit, UV-Excess Systems	65
2.6.3	Individual Sources	66
2.7	Summary & Conclusions	94
3	Thesis Conclusions & Future Research Directions	96
Appendices		120
A	Full Chandra/Galex Dataset	121

List of Tables

2.1	Specifications of the <i>GALEX</i> NUV detector.	26
2.2	Expected numbers of <i>GALEX/Chandra</i> positional chance matches.	34
2.3	Spectral type vs. expected X-ray and optical fluxes.	54
2.4	Number of optical, infrared counterparts to <i>GALEX/Chandra</i> systems in each survey used.	55
2.5	Final list of UV excess sources.	67
A.1	Full <i>GALEX/Chandra</i> dataset.	130

List of Figures

1.1	Relation between Rossby Number (R_0), rotational period (P_{rot}), X-ray luminosity (L_X) for coronally active stars.	6
1.2	L_X as a function of stellar mass M_\odot for coronally active stars.	7
2.1	<i>GALEX</i> NUV filter transmission profile.	25
2.2	<i>GALEX</i> NUV coverage of the Galactic Bulge Survey.	28
2.3	Distribution of <i>Chandra</i> positional error.	30
2.4	Distribution of positional offsets between <i>GALEX</i> / <i>Chandra</i> matches.	33
2.5	VPHAS+ Galactic footprint.	38
2.6	Example of stellar template fitting for a single source, using two different values of $E(B - V)$	44
2.7	Synthetic observation of HD154712 from the BPGS spectral library, fitted with Pickles template spectra.	46
2.8	MCMC model of CX93, showing fitted model and corner plot for visualizing parameter degeneracy.	49
2.9	Synthetic observations and modelling of active binaries RS CVn, Algol and BY Dra.	52
2.10	Effectiveness of <i>GALEX</i> -matching algorithm (distribution of counterpart numbers).	56
2.11	$(J - H)$ vs. $(H - K)$ colour-colour diagram.	58
2.12	$(NUV - B)$ vs. $(B - V)$ colour-colour diagram.	59
2.13	$(J - H)$ vs. $(B - V)$ colour-colour diagram.	60

2.14 Distribution of best-fit spectral classes for the single stellar population.	62
2.15 Comparison of NUV excess levels for 5 systems to the M-dwarf NUV relation from Stelzer et al. (2013).	63
2.16 SEDs of known compact binaries in our dataset.	68
2.16 SEDs of 18 UV excess systems.	70
2.17 SED model of CX93 with MCMC (large figure).	72
2.18 SED model of CX118 with MCMC.	74
2.19 SED model of CX137 with MCMC.	76
2.20 SED model and optical image of CX388.	78
2.21 Optical image of CX398.	79
2.22 SED model of CX417 with MCMC.	81
2.23 IR and optical images of CX417.	82
2.24 IR and optical images of CX645.	85
2.25 IR and optical images of CX673.	87
2.26 IR and optical images of CX886.	88
2.27 3 different SED models for CX886.	89
2.28 Optical image of CX1029.	90
2.29 Optical image of CX1042.	91
2.30 Optical image of CX1229.	92
2.31 SED model of CXB208 with MCMC.	93

Chapter 1

Introduction

1.1 Ultraviolet & X-ray Radiation in Astrophysics

Light of shorter wavelengths than our optical spectrum ($\lambda \lesssim 320$ nm) is regarded here as *high energy* radiation. This is because it is light that is too energetic for the receptors in our eyes to process - just beyond the colour violet, the *ultraviolet* is the wavelength range between $10\text{ nm} \lesssim \lambda \lesssim 320\text{ nm}$ (*ultra* means ‘beyond’ in Latin). At even smaller and more energetic wavelengths is the *X-ray* regime between $0.1\text{ nm} \lesssim \lambda \lesssim 10\text{ nm}$. Like any part of the electromagnetic spectrum, UV and X-ray photons are emitted by astrophysical particles accelerating from forces, and all four fundamental forces are responsible for high energy astrophysical radiation. The majority of processes discussed in the context of Galactic X-ray sources originate from electromagnetic and gravitational forces.

In general, *Larmor’s Formula* describes the power emitted by a particle of charge q undergoing acceleration a (non-relativistic, $v \ll c$):

$$P = \frac{q^2 a^2}{6\pi\epsilon_0 c^3} \quad (\text{Watts}) \quad (1.1)$$

where $c \simeq 3 \times 10^8$ m/s (the speed of light) and $\epsilon_0 \simeq 8.854 \times 10^{-12}$ F m $^{-1}$. A careful consideration of the acceleration mechanism for each particle and a sum over all accelerating particles yields the volume emissivity j_ν . X-ray emission mechanisms usually require high energy electrons (large β , where $\beta = \frac{v}{c}$) and so the special relativistic formulation is useful:

$$P = \frac{2q^2\gamma^6}{3c} [\dot{\beta} - (\beta \times \dot{\beta})^2] \quad (\text{Watts}) \quad (1.2)$$

where $\gamma = (1 - \beta^2)^{-1/2}$.

There are a variety of X-ray emitting objects and associated processes spanning a range of X-ray luminosities L_X . Although our focus will be on *Galactic* X-ray emission we mention some extraGalactic X-ray sources here for completeness. X-ray point sources include both degenerate and non-degenerate stars, compact and non-compact binary systems, active Galactic nuclei (AGN) and star forming regions (e.g., Orion Nebula or h Per). Diffuse X-ray sources include supernovae remnants (e.g., Crab Nebula, Cassiopeia A), all types of galaxies, galaxy groups and clusters (e.g., Perseus Cluster, M87) and even planets (e.g., Jupiter) and comets (e.g., 73P/Schwassmann-Wachmann). The focus of this work is to identify compact binary systems and therefore the bulk of this discussion will be focussed on X-ray point sources.

The most basic production mechanism of high energy light is *thermal emission* from hot, optically thick matter where particles accelerate due to electromagnetic interactions from neighbouring particles. A star is roughly a blackbody emitter due to high temperature and densities (at least below the photosphere) and its light spectrum is governed broadly by *Planck's Law* or 'the blackbody function'

$$B(\lambda, T) = \frac{2hc^2}{\lambda^5} \frac{1}{e^{\frac{hc}{\lambda kT}} - 1} \quad (\text{W sr}^{-1} \text{ m}^{-3}) \quad (1.3)$$

where $h = 6.63 \times 10^{-34}$ m 2 kg s $^{-1}$ (Planck's constant), $k = 1.38 \times 10^{-23}$ m 2

kg s^{-1} (Boltzmann's constant) and T the effective temperature of the star in Kelvin. The Planck Distribution describes the spectral density of emitted photons in equilibrium and is the unique, stable such distribution (Planck 1914). It describes hot, dense matter like the thermal emission from a star or a hot, optically thick accretion disk in both CVs and X-ray binaries (XRBs). As temperature increases the peak of emission shifts to higher energies following Wien's Law:

$$\lambda_{peak} = \frac{b}{T} \quad (\text{m}) \quad (1.4)$$

where $b = 2.898 \times 10^{-3} \text{ m K}$. Stars peaking at the least energetic part of the UV spectrum ($\sim 320 \text{ nm}$) need to achieve effective temperatures of $T \simeq 9000 \text{ K}$ or an earlier spectral type than $\sim \text{A3V}$. To peak in the X-ray (say at 1 nm) the temperature needs to reach $T \sim 3 \times 10^6 \text{ K}$. These (effective) temperatures cannot be reached by non-compact stars in regular stellar evolution but are easily achieved in material liberating its energy in the steep gravitational potential of a CO. Thermal emission from a single non-degenerate star is usually insufficient to explain observed X-ray luminosities $L_X > 10^{29} \text{ erg/s}$ and it is non-blackbody processes responsible for X-ray emission in regular stars. Optically thin radiation from hot, ionized material is common in binary accretion scenarios and stellar atmospheres. The principal non-relativistic radiation mechanism from hot, ionized material is *thermal bremsstrahlung* or ‘braking radiation’, where high speed electrons accelerate around more massive protons in the plasma. The volume emissivity of thermal bremsstrahlung emission as a function of temperature is:

$$j_\nu(\nu) = C g(\nu, T, Z) Z^2 n_e n_i \frac{e^{-\frac{h\nu}{kT}}}{T^{\frac{1}{2}}} \quad (\text{W m}^{-3} \text{ Hz}^{-1}) \quad (1.5)$$

where $C = 6.8 \times 10^{-51} \text{ J m K}^{\frac{1}{2}}$, $g(\nu, T, Z)$ is the Gaunt factor (a quantum correction of order ~ 1), Z is the atomic number of the atomic species, n is density, and T temperature. For temperatures between $10^5 - 10^8 \text{ K}$ this

distribution peaks in the extreme ultraviolet (EUV) or soft X-ray.

1.1.1 Single Stars

Thermal emission from both optically thick and thin bodies explains a large portion of the spectral energy distribution of single stars. The stellar temperature profile $T(r)$ is generally a decreasing function of radius but inverts in the outermost region or *corona* of many cool stars (including the Sun); we observe spectral features only produced in temperatures of $10^6\text{-}10^7$ K (for example, transitions of the ionic species Fe-XIV at 5303 Å and Fe-X at 6374 Å in the Sun) prompting an explanation of some unknown coronal energy source. Temperature inversion and emission in excess of radiative equilibrium is more or less the definition of the corona itself (Hall, 2008).

The behaviour of hot, magnetically-confined coronal plasma is known as *chromospheric* or *coronal* activity observed as emission in excess of the black-body at short wavelengths (UV, X-ray, γ -Ray). All late-type stars (past $\sim A7$) are coronal X-ray emitters (Vaiana et al., 1981). Stellar coronae are physically extended, optically thin plasmas that are a source of both line and continuum UV/X-ray. They are highly ionized by the photospheric flux below and emit at $T \sim 10^7$ K soft-X-ray continuum via *thermal bremsstrahlung* (Section 1.1). The layer beneath the corona (the chromosphere) produces Ca II H & K emission lines in abundance and these lines are generally used as indicators of coronal activity levels (West et al., 2008).

The interaction of the coronal plasma and the stellar magnetic field is likely the source of coronal heating. Velocity shear from differential rotation between the convection cells and the radiative zone energetically drive large-scale, variable magnetic structures which thread high through the corona (the *dynamo* mechanism). These fields interact strongly with the plasma by induction, and production of magnetohydrodynamical (MHD) waves that heat the surroundings (Hall, 2008). The plasma and the magnetic field lines are both mag-

netic - the movement of either component induces complex changes in both. The short-timescale variability of the corona (seconds to minutes) reflects the timescale of changes in the magnetic field structure itself.

Although it is not our intent to study stellar rotators in general, a macro-connection between late-type stars and their induced X-ray luminosities is helpful. The ability for the dynamo to produce magnetic activity or the *dynamo efficiency* is typically characterized by the *Rossby Number* (Noyes et al., 1984) which combines the rotation rate P_{rot} and convective turnover time τ_c (the rotation rate of the convection cell):

$$R_0 = \frac{P_{rot}}{\tau_c} \quad (1.6)$$

Stellar activity typically increases with decreasing R_0 and it is observed that late-type stars saturate in their coronal X-ray emission at $R_0 \simeq 0.1$ (Vilhu, 1984; Stepien, 1994; Patten and Simon, 1996; Pizzolato et al., 2003) where higher rotation rates do not add any extra flux in the X-ray and in fact may decrease with a further increase in rotational frequency. The relation between R_0 , $R_X = L_X/L_{bol}$ and P_{rot} is shown in Figure 1.1 (Wright et al., 2011, Figure 2).

The convective turnover time can be estimated as a function of stellar mass following Wright et al. (2011) as a second-order log-log polynomial,

$$\log(\tau_c) = 1.16 - 1.49\log(M/M_\odot) - 0.54\log^2(M/M_\odot), \quad (1.7)$$

with an rms dispersion in $\log(\tau_c)$ -space of ~ 0.028 . This relation is valid for MS masses $0.09 < M/M_\odot < 1.36$ but is highly uncertain for $M < 0.15M_\odot$ due to a lack of data for the lowest-mass stars. Other parameterizations as functions of $V - K_s$ and $B - V$ exist but they are not nearly as tight, and even be piece-wise; convection may be driven primarily by the stellar mass and complex-colour dependencies on various stellar parameters make a $\tau(M/M_\odot)$

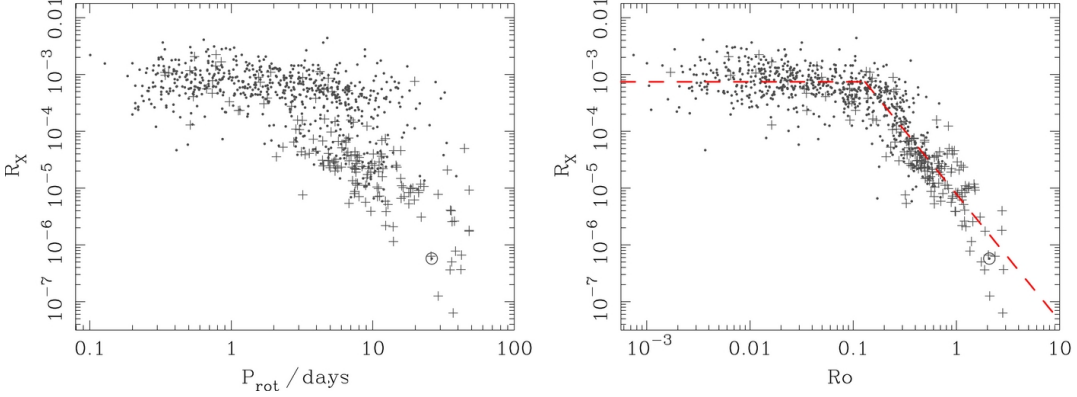


Figure 1.1: (left) $R_X = L_X/L_{bol}$ by rotational period and (right) by the Rossby number. Notice the parameterization with R_0 is far tighter than P_{rot} , and as expected X-ray luminosity increases with decreased rotational period or R_0 . The piece-wise, red dashed line represents the unsaturated (sloped) and saturated (flat) regimes (Wright et al., 2011, Figure 2).

parameterization most useful.

Summarily, the rotation period and stellar mass are connected via the Rossby number, which is itself connected to X-ray luminosity. We summarize this discussion by showing X-ray luminosity versus stellar mass (Figure 1.2) using Equations 1.6 and 1.7 together for some values of rotational period P_0 .

Stellar magnetic fields can undergo explosive, short-timescale changes (*magnetic reconnection*) that produce solar flares and coronal mass ejections that manifest as a burst of hard X-ray emission, followed by a soft rise from the X-ray heating of the upper atmosphere. Magnetic reconnection occurs when a magnetic field loop pinches in two after being highly stressed. The rapid change in the B field strength over only a few seconds creates an intense DC electric field E that accelerates electrons beyond ~ 20 keV (Hall, 2008). These electrons stream back into the stellar atmosphere and undergo (inefficient) Coulomb collisions with ambient protons, emitting a burst of hard X-rays - this process is known as *non-thermal bremsstrahlung* or *thick target bremsstrahlung*. A short burst of hard X-rays is almost always observed at the beginning of a flare event and is usually used as an indicator of the event itself. The hard X-rays heat and

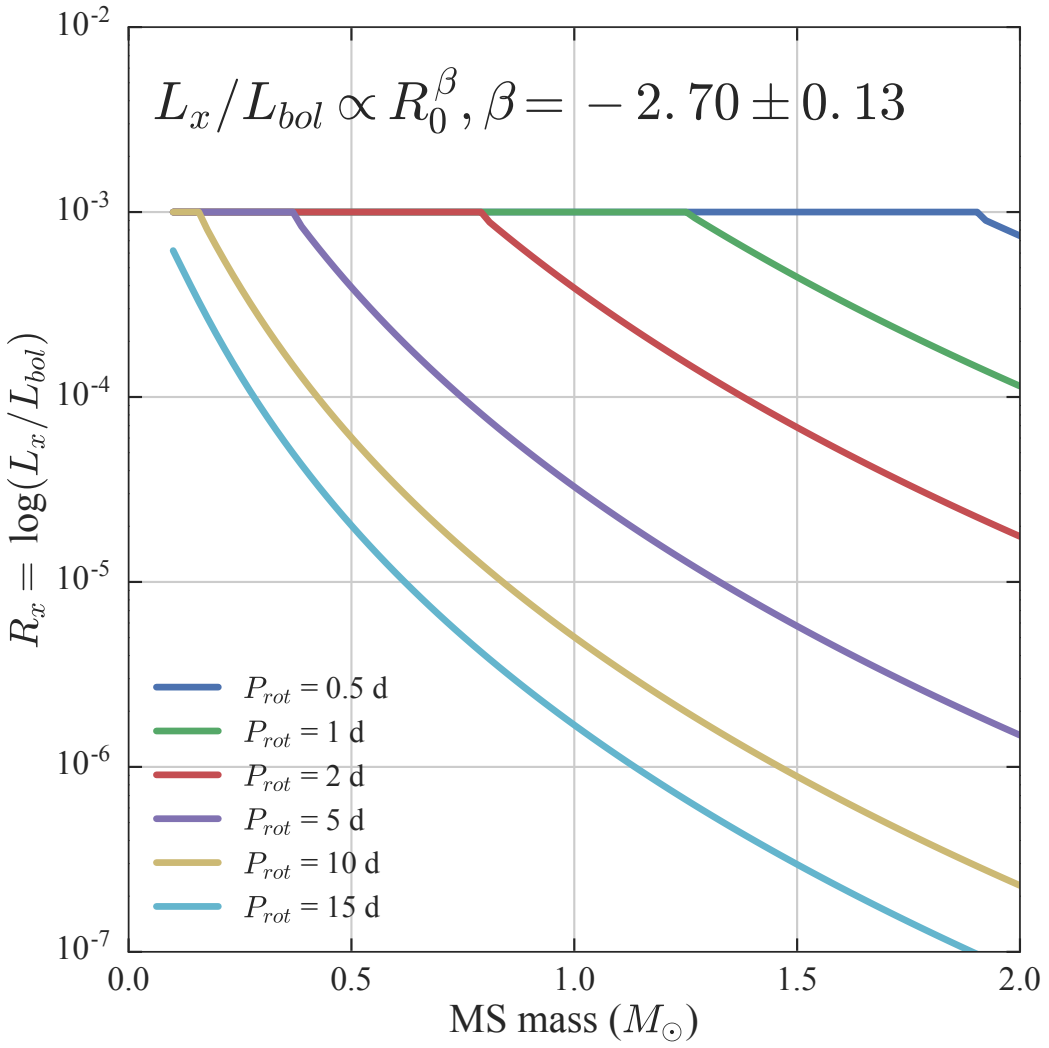


Figure 1.2: R_X as a function of stellar-mass for a few values of rotational period P_{rot} . Saturation occurs at $R_X = 10^{-3}$. Only $M_\odot > 0.1$ are shown, for the relationship is uncertain beyond this range (Wright et al., 2011). It appears that no stellar mass can saturate at a rotational period above $\sim 10 - 15$ d.

create a pressure gradient driving bulk plasma motion that emits soft X-rays in the process. This bulk flow is likely responsible for the time delay between the rise in hard versus soft X-rays immediately after a flare (Güdel, 2004). Non-thermal bremsstrahlung is thought to be the main contributor of hard X-rays in single-stellar atmospheres and their presence is often more sporadic (burst-like) than the soft coronal continuum.

In summary, single-stars are X-ray/UV emitters up to $L_X \sim 10^{30}$ erg/s due to their hot, coronal plasma interacting with the stellar magnetic field.

1.1.2 Compact Binary Systems

Formation of a Compact Object

All stars undergo *stellar evolution* where the temperature, composition, and radius of the star change over their lifetime. The outcome of stellar evolution in isolation is almost entirely determined by the initial mass of the star. In general, a star maintains a quasi-equilibrium between the inward pull of gravity and outward thermal pressure that originates from formation energy and ongoing nuclear fusion in the core.

A star spends the majority of its lifetime on the main-sequence (MS) fusing core H into He until H runs out and the burning equilibrium is disrupted. Without the core pressure from H fusion, the core begins to contract and H fusion is initiated in a shell around the predominantly He core, stabilizing the contraction. This shell burns hotter than the core-burning itself and increases the luminosity of the star leading to an envelope expansion. As each burning layer runs out of fuel, the resultant fusion products add to the core mass, shrinking it further, igniting the new shell layers and expanding the star while ascending the red giant branch (RGB). From here, the star moves through the horizontal branch (HB) and asymptotic giant branch (AGB), where large mass-loss can occur from stellar winds before the end of its life. What happens

next is strongly dependent on the core mass (\sim original mass - mass lost during lifetime): for stars with $M < 8M_{\odot}$ thermal pressure eventually becomes insufficient to balance gravity and the star contracts until it is supported by degenerate electron pressure, resulting from both Heisenberg's uncertainty and Pauli exclusion principles. Heisenberg's Uncertainty Principle states that the ignorance of a particle's momentum and position in space has a lower limit of roughly \hbar :

$$\Delta x \Delta p \geq \frac{\hbar}{2} \quad (1.8)$$

The core of a star with an initial mass $M < 8M_{\odot}$ can be supported by *electron degeneracy pressure*. Such a core is referred to as a *white dwarf* (WD). The Pauli exclusion principle forbids the electrons from occupying the same phase space cell manifesting as a resistive pressure. WDs are \sim the size of earth and typically $\sim 0.6M_{\odot}$ with densities of $\rho \sim 10^9$ kg/m³; binaries with a WD primary accreting from a companion are known as *cataclysmic variables* (CVs; see Section 1.1.2).

Electron degeneracy pressure cannot support the cores of stars of initial mass $M > 8M_{\odot}$ against collapse and instead *neutron* degeneracy pressure exists, leaving a *neutron star*. It is thought to be the size of a small city ($R \sim 10 - 15$ km) with average densities exceeding $\sim 10^{17}$ kg/m³. Neutrons are ~ 2000 times heavier than electrons and thus their momentum uncertainties Δp can be quite large. Thus, Δx can be much smaller than the electron allowing neutrons to spatially pack themselves more closely (neutron stars are \sim a factor of a billion more dense on average than WDs). If the stellar core mass is high enough ($M > 20M_{\odot}$) there exists no degenerate pressure strong enough to counter the gravitational collapse, and the star becomes a black hole.

Accretion in Compact Binaries

The deep gravitational wells of a CO can inject high energies into nearby material, including other stars. Binaries with one or more components consisting of a WD, NS or BH in a close orbit ($a \sim$ order of the donor's radius) are referred to here as *compact binary systems*. They can emit a copious amount of X-rays ($10^{30} \sim 10^{42}$ erg/s) and show distinct states of activity that dramatically change the emission behaviour. The movement of material from the companion star to the compact primary is known as *accretion*, and this process is responsible for the macroscopic behaviour of compact binaries. Different stages of accretion and the response of the mass ratio q and orbital separation a to these modes ultimately decides the long-term evolution of the binary.

There are two types of accreting binaries: *transient* systems that go in and out of outburst and *persistent* systems that are in constant outburst. The mass ratio $q = M_{CO}/M_{donor}$ and donor radial velocity K_2 are two fundamental binary parameters that describe the accretion. It is not our intent to review accretion theory entirely, a basic understanding of these parameters is helpful. The parameters q and K_2 are usually obtained in quiescence with optical or IR spectroscopy when the dimness of the accretion disk allows study of the companion. Combining K_2 and P_{orb} directly limits the value of q , where this relation is detailed by the *mass function* (derived from Kepler's 3rd Law):

$$f(M_1) = \frac{PK_2^3}{2\pi G} = \frac{M_1 \sin^3(i)}{(1+q)^2} \quad (1.9)$$

where i is the inclination (the angle between a line perpendicular to the system orbital plane and our line of sight, e.g., an edge-on system has inclination 90°); this parameter is often difficult to obtain. If the system in quiescence still has a large optical contribution from the disk, K_2 can be derived from its linear relation with the full-width-half-maximum (FWHM) of the $H\alpha$ line in the accretion disk (Casares, 2015, 2016). Persistent sources are constantly in

outburst and therefore bright in the optical, UV and X-ray. These bands are dominated by the CO and disk and are never in quiescence which wash out the companion’s spectral features. In these cases, the companion’s radial velocity can be derived by tracking a series of fluorescent emission lines from the X-ray irradiated companion face during certain parts of the orbit. These emission features from the companion face are known as *Bowen fluorescence transitions* (Casares et al., 2003, 2004; Sánchez et al., 2015).

Finally, the mass ratio q and semi-major axis a define the geometry of the gravitational potential in the system of two stars. It is this geometry that controls the accretion process; local extrema in the potential (*Lagrange points*) represent places where material can remain in a stable co-orbit or where matter can leave one star and be bound to the other. As the companion expands during stellar evolution, it may fill the volume around it known as the *Roche Lobe* which is the smallest surface of equipotential, defined by the scale radius R_L :

$$\frac{R_L}{a} \simeq \frac{2}{3^{4/3}} \left(\frac{q}{1+q} \right)^{1/3} \quad (1.10)$$

Material exceeding this volume is no longer bound to the donor; material preferentially leaves through the first Langrangian point (L1) at a distance $\sim R_L$ from the center of the donor. The ability for a star (at a particular part of its life cycle) to fill this lobe and lose mass depends solely on a and the mass ratio, q . The Coriolis force deflects the accretion stream into Keplerian motion around the primary, but the stream may couple to the field and accrete directly onto the primary if its magnetic field is strong enough. Small collisions of the streaming particles with each other (e.g., viscous friction) spread the orbital radii of the particles forming an accretion disk truncated at the Alfvén radius of the primary. The interactions between the donor, accretion stream/disk, magnetic field(s), stellar winds and compact object create the variety of high energy radiation we attribute with the name “X-ray binary”.

Here we review compact systems relevant to this thesis: CVs, symbiotics

and low-mass XRBs with specific focus on the systems appearance in the X-ray, UV and optical components of the spectral energy distribution (SED).

Cataclysmic Variables

Cataclysmic variables or CVs are close binary systems of a WD primary and a Roche-Lobe-filling donor, with orbital periods $75 \text{ min} < P_{orb} < 8 \text{ h}$ capable of X-ray luminosities of $L_X \simeq 10^{29} - 10^{33} \text{ erg/s}$ (Ritter and Kolb, 2003). The majority of CV donors are Roche-lobe-filling MS stars but there exist systems with a less massive WD donor (AM CVn) or a giant donor (symbiotic systems). The short and long-term behaviours of CVs depend primarily on the mass transfer rate \dot{M} and magnetic strength B of the WD and their interaction determines the accretion state (Lewin and van der Klis, 2006).

CVs with weak WD magnetic fields ($B \lesssim 10^4 \text{ G}$) are essentially ‘non-magnetic’; accreting material can accumulate in an *accretion disk* that interacts with the WD close to its surface, in a region called the *boundary layer*. This boundary layer is thought to be the primary source of both soft and hard X-rays in CVs. The accretion disk acts as a reservoir of gas and ultimately energy for the outburst behaviour of CVs and XRBs alike. Non-magnetic CVs can be in either quiescence or outburst, controlled by \dot{M} : when \dot{M} is low, the disk is cool and has a low viscosity. When the disk heats, its viscosity increases allowing movement of material inward towards the WD inducing direct accretion - this is the high \dot{M} regime. The inward movement of disk material liberates gravitational energy producing a bright, explosive outburst known as a *dwarf nova* (DN). *Nova-like* (NL) systems have a high enough \dot{M} that the disk is maintained in high temperature/viscosity equilibrium and does not exhibit typical DNe (Honeycutt, 2001). The accretion stream, disk and the boundary layer can in principle be seen in a spectral energy distribution (SED) and are inherently variable in the optical, UV and X-ray outside of that expected from orbital geometry changes on timescales $\tau \sim P_{orb}$. In short P_{orb} non-magnetic

CVs, the accretion disk usually contributes 40-75% of the observed optical light while the WD contributes 75-90% of observed UV (Szkody et al., 2017). Systems with disks (DNe or NLs) ostensibly can be identified by their SED given the large fractions of optical/UV light emitted from the WD and surrounding material.

If the WD B field is strong enough ($B > 10^4$ G) it either completely prevents an accretion disk from forming (a *polar* system) or truncates the disk at some distance from the WD (an *intermediate polar* system). In polars, the accretion stream couples to the magnetic field lines between the donor and the WD and is channeled to one or two regions near the WD surface. This produces a noticeable cyclotron spectrum from the IR to the UV (Wickramasinghe and Ferrario, 2000; Williams et al., 2007) from spiraling electrons in the B field and X-rays from shock heating at WD surface (Lewin and van der Klis, 2006). Polars are primarily soft X-ray sources, typically peaking in the EUV where instrument sensitivity is low and interstellar absorption is extremely high. This leaves polars far less studied than non-magnetic CVs. Although polars lack an accretion disk, the accretion stream and shock-spot near the WD surface can be incredibly bright, contributing \sim 50% of the total optical emission (Harrop-Allin et al., 1999).

In summary, both magnetic and non-magnetic CVs emit X-ray light beyond the active single-stellar emission discussed in Section 1.1.1. The emission of X-rays comes primarily from the WD surface, where direct accretion takes place. However, many components of the system emit relevant radiation: the boundary layer, the disk and/or magnetic field structure, the accretion stream and collision point and the irradiated companion face. In Section 1.1.2 we will explore how similar systems with a neutron star (NS) instead of a WD changes the system’s dynamics.

Symbiotic Stars

Symbiotic binary stars (SBs) are a distinct class of CV where a WD accretes the stellar winds of a red giant donor (Kenyon and Webbink, 1984; Sokoloski, 2003). These systems exhibit various outburst-like behaviours, probably related to Bondi-Hoyle type accretion onto the WD surface but this is not yet fully understood (Sion and Starrfield, 1994). We refer to those with a WD primary as SBs and those with a NS or BH primary as *symbiotic XRBS*. Unlike typical CVs, SB accretion is fed by the giant's wind where only a small portion is actually accreted (owing to the geometrical extent of the wind and the comparatively small cross-section of the WD). SBs show prominent emission features in low resolution spectroscopy (e.g., TiO features from the red giant photosphere and H I, He II and OIII in emission) thought to be emitted from H shell-burning on the WD surface and photoionization of the giant's wind. These emission features have been used historically to identify such systems, however there are SBs that show peculiar outburst behaviours, lack one or more distinct emission features or have a NS or BH primary making the definition of SBs broader than previously thought. Luna et al. (2013) adopt a more general definition of any compact object accreting enough material from a red giant companion to be observed at any wavelength, but we limit this summary to the most abundant WD SBs. In light of this updated definition, the known population of Galactic SBs is probably biased towards shell-burning types which show the aforementioned prominent optical lines in low-resolution spectroscopy (Mukai et al., 2016). Shell-burning SBs burn H steadily on the surface of the WD similar to post-novae behavior or supersoft X-ray emission, and show steady UV emission while *non-shell* burning systems show variable UV emission on short timescales, interpreted as a flickering of the accretion disk (Luna et al., 2013). UV timeseries data in combination with confident counterpart identification in IR surveys like *2MASS* and *WISE* could uncover previously unidentified SBs given recent advancements in near and mid IR

classifications of SBs (Akras et al., 2017).

Low Mass X-ray Binaries (LMXBs)

Low-mass XRBs (LMXBs) consist of a NS or BH primary with a low mass ($M \leq 1M_{\odot}$), Roche-Lobe-filling donor with short orbital periods (< 6 h) and X-ray luminosities between $10^{32} < L_X < 10^{39}$ erg/s. These are observed as steady X-ray systems; X-ray studies typically determine the primary properties and optical/IR studies determine the companion properties. LMXBs allow us to study various physical mechanisms that define the current Galactic population such as the common-envelope formation efficiency, gravitational wave emission, magnetic field evolution and strength in old NSs and the age of a stellar population in general.

The accretion disk mediates the accretion flow onto the NS/BH analogous to CVs (Section 1.1.2). van Paradijs and McClintock (1994) found that the absolute visual magnitudes of 18 LMXBs are between ~ 5 and ~ -5 , with such a large range attributed to the range of X-ray luminosities and accretion disk size. This indicates it is the reprocessing of X-rays through the disk that dominates the optical spectrum in outburst although it has been suggested an irradiated face of the companion could contribute to the optical (however this face may be shielded for large portions of the orbital cycle). Moreover, in a toy model assuming an isotropically-emitting blackbody disk (van Paradijs and McClintock, 1994) show that $L_V \propto L_X^{1/2} P^{2/3}$ where the dependence on orbital period reflects that smaller disks have higher average temperatures, and the blackbody distribution shifts a larger fraction of its flux into the UV at the expense of optical emission. In quiescence, the disk is cool and the optical spectrum is dominated by the donor ($V \sim 16 - 23$, Lewin and van der Klis, 2006), which can allow the measurement of $f(M)$ using spectral type, period and K_2 . The optical spectra of LMXBs show blue continua with broad, superimposed H and He emission lines that reflect the velocity dispersions in the inner disk

region. For persistent sources with NS primaries, there exists a tight correlation between absolute near-IR magnitude and orbital period (Revnivtsev et al., 2012) analogous to van Paradijs and McClintock (1994) for the optical V, with the assumption that the NIR could have a non-zero synchrotron contribution from a jet (Shahbaz et al., 2008).

Almost all Galactic BHs and many NSs are found in XRBs and the current sample of Galactic XRBs is dominated by bright ($L_X > 10^{36}$ erg/s) transient systems making it under-filled by those in long periods of quiescence. Quiescent LMXBs and CVs both have X-ray luminosities of $\sim 10^{30.5} - 10^{32.5}$ erg/s and are best identified with deep X-ray data and precise positional resolution (Grindlay et al., 2005), although distinguishing the two generally requires a direct mass measurement of the compact object. The deeper potential well of a NS or BH creates a larger L_X for a given \dot{M} and so F_X/F_{opt} is a useful discriminant; CVs are not thought to exceed $L_X \sim 10^{34}$ erg/s. Particularly quiet/distant systems produce low numbers of X-ray counts making statistical inference difficult.

1.2 The Galactic Bulge Survey (GBS)

In Chapter 2 we present our recent work with the Galactic Bulge Survey (GBS), a wide and shallow *Chandra* X-ray survey of 12 square degrees above and below the Galactic Plane (Jonker et al., 2011). The purpose of this survey was to homogenize the Galactic X-ray sample by uncovering > 100 new quiescent LMXBS to ultimately put constraints on the common-envelope evolution in XRBs and the mass distribution of BHs and NSs. The survey depth was chosen to optimize LMXB detections over foreground CVs and the survey is out of the plane enough to allow optical and IR follow-up. Spectral observations are crucial in deriving compact object masses - the $H\alpha$ shape and width can be used to identify the presence of an accretion disk or a BH-primary (Casares, 2015, 2016) and the aforementioned Bowen fluorescence transitions at $4640 - 4650\text{\AA}$

can identify the companion. The GBS photometric and spectroscopic follow-up is on-going and many compact systems have already been identified; however, many X-ray sources have multiple optical or IR counterparts within the positional error circle of *Chandra*. Greiss et al. (2013) and Wevers et al. (2016a) performed a matching analysis for the GBS in deep IR and optical observations, respectively. A UV analysis has not yet been completed, although some *Swift* pointings in the GBS region have been analyzed for *Swift* UVOT (Fielder et al., in prep). The extinction in the GBS region is lower than directly in the Galactic Plane, but not as low as sightlines outside of the main Galactic mass entirely. Accordingly, since UV radiation is preferentially absorbed by the interstellar medium over other bands a UV analysis will retrieve physically close objects, those in windows of particularly low extinction and those that are inherently UV bright. In Chapter 2, we perform a UV counterpart analysis using *GALEX* data in the near-UV and use the statistical likelihood of an X-ray/UV match to constrain optical and IR observations allowing multi-wavelength analysis for 269 GBS systems.

Chapter 2

The Galactic Bulge Survey: a *GALEX* Ultraviolet Counterpart Catalogue

Reuben S. Gazer¹, C.O. Heinke¹, P. Groot², Chinmaya Verma^{1,3}, S. Rowe^{1,4}

¹ *Dept. of Physics, University of Alberta, Edmonton, Canada, T6G 2R3*

² *Dept. of Astrophysics, Radboud University, Nijmegen, The Netherlands, NL-6500 GL*

³ *Dept. of Physics, Indian Institute of Technology, Kharagpur, India, 721302*

⁴ *Dept. of Physics & Astronomy, University of Leicester, Leicester, UK, LE1 7RH*

2.1 Introduction

2.1.1 The Galactic Bulge Survey: Purpose & Progress

The Galactic Bulge Survey (Jonker et al., 2011, 2014) was designed to identify a large sample of Galactic X-ray binaries (XRBs) in quiescence ($L_X \sim 10^{32-33}$ erg/s) using the *Chandra* X-ray Observatory (Weisskopf, 2012). The two main purposes of the GBS require a homogeneous sample of the Galactic X-ray population. The first GBS goal is to obtain a model-independent measure of neutron star (NS) and black hole (BH) masses to constrain the NS equation of state and BH mass distribution. Nearly all Galactic BHs and many NSs are found in binaries and to date the observational sample of Galactic XRBs is ostensibly dominated by bright, transient systems (Liu et al., 2001; van Paradijs and White, 1995). Bright ($L_X \geq 10^{36}$ erg/s) Galactic X-ray sources have been well-studied but may not accurately represent the larger population of NS and BH X-ray binaries (XRBs) with systems in outburst more well-studied than the quiescent population. Inferred global properties of the entire population could be skewed due to this transient selection bias, such as the BH-mass-period relationship (Lee et al., 2002; Knevitt et al., 2014) indicating a search for a larger *quiescent* binary population is needed. The GBS also aims to constrain uncertain steps in XRB evolution models, in particular the common envelope formation and evolution in the context of BH-XRB formation channels (Ivanova, 2011; Ivanova et al., 2013; Pavlovskii et al., 2017).

To achieve a large, quiescent, Galactic XRB population the survey needed to cover a substantial portion of the stellar mass of our Galaxy. To avoid heavy extinction (permitting study of the optical/IR counterparts) the survey focused on the Galactic Bulge above and below the plane at Galactic longitudes and latitudes between $-3^\circ \leq l \leq 3^\circ$ and $1^\circ \leq |b| \leq 2^\circ$ respectively. The GBS depth was chosen to optimize the detection of typical quiescent low-mass XRBs (qLMXBs) in the Galactic Bulge but not deeper to avoid picking up larger num-

bers of CVs and chromospherically active stars. However, the survey includes a volume of the Galactic Plane near the Sun and so will include a substantial number of intrinsically fainter X-ray sources in the near field. The high astrometric accuracy of *Chandra* ($0.6''$ at 90% confidence, for on-axis sources with reasonable numbers of counts) is necessary to enable identification of faint counterparts, as expected for qLMXBs in the Bulge and crowded fields. Flux-limited, Galactic X-ray surveys should preferentially sample young stars in the disk due to the decline in general X-ray emission with stellar age (Koenig et al., 2008; Vaiana et al., 1981, 1992). A number of surveys focused on faint, Galactic X-ray sources have confirmed this illustrating that active stars/binaries dominate $L_X < 10^{32}$ erg/s while CVs dominate $10^{32} < L_X < 10^{34}$ erg/s (Hands et al., 2004; Sazonov et al., 2006; Agüeros et al., 2009; Motch et al., 2010; Warwick, 2014). *Chandra* surveys have been particularly effective: the ChaMPlane survey (Grindlay et al., 2005; Koenig et al., 2008) obtained deep ($\geq 20 - 100$ ks) *Chandra* pointings near the Galactic Plane and discovered a population of coronally active systems: young MS stars, MS stars and active binaries like RS CVn and BY Dra. Ebisawa et al. (2005) took deeper observations and suggest their soft X-ray population is mostly Galactic late-type stars. These findings suggest that while many sources in our shallow *Chandra* dataset located at ~ 8 kpc are likely to be LMXBs, the nearby low-luminosity sources that show UV emission in *GALEX* will be dominated by coronally active systems.

The GBS found 1640 unique X-ray sources, a number in good agreement with initial population estimates (Jonker et al., 2011). The full Galactic distribution of X-ray emitter types is still unknown, but pre-survey estimates suggest ~ 700 non-compact stars/binaries, 600 CVs, 300 XRBs, possibly as many as a few hundred AGN (Britt et al., 2014) and some millisecond pulsars. To date, the GBS collaboration and other groups have identified counterparts in the optical, IR and radio. Bright optical counterparts usually suggest X-ray emission from nearby chromospherically active stars (Güdel, 2004). A number of these

counterparts were initially confirmed by Udalski et al. (2012) using OGLE lightcurves and Britt et al. (2014) using MOSAIC-II imaging. Hynes et al. (2012) matched Tycho-2 sources to the GBS, finding mostly coronally-active stars and a few potential quiescent HMXBs. Numerous accreting sources have been identified with optical spectroscopy, radial velocity analysis, variability or direct observation of dwarf novae as well a few AGN in the radio (Ratti et al., 2013; Britt et al., 2013; Maccarone et al., 2012). Rarer objects like an AM CVn (a CV with a white dwarf donor, Wevers et al., 2016b), a carbon star donor in a symbiotic binary (Hynes et al., 2014) and a possible accreting YSO (Britt et al., 2016) have been identified. Torres et al. (2014) found 23 accreting binaries in the GBS and Wevers et al. (2017) recently produced optical spectra for 26 systems. Many dimmer optical and IR counterparts have also been located, but the surface densities in these bands are far larger than one per *Chandra* positional error circle leaving many systems still unclassified. Wevers et al. (2016a) (herein W16) produced a detailed list of MOSAIC-II optical counterparts in SDSS r',i' and computed likelihoods for each source; despite this, many GBS systems have multiple, comparably-likely optical sources nearby often making companion identification unclear. Likewise, Greiss et al. (2013) (herein G13) matched the GBS to near-IR data with 2MASS, VVV and UKIDSS computing likelihoods in a similar fashion. Both analyses find that $\sim 70\%$ of GBS systems have more than a single counterpart in the *Chandra* error circle.

2.1.2 SED Fitting the GBS via UV Counterparts

Our aim is to locate unidentified compact binaries in the GBS by selecting photometric counterparts from these works (and other archival datasets) under a given condition of confidence to model spectral energy distributions (SEDs) from the NUV through the mid-IR. The presence of prominent UV excesses correlated with the X-ray observation could indicate high energy emission from a compact system. To assess the SED at all, we need to select a unique ph-

tometric set to model. First we identify near ultraviolet counterparts (NUV, $1750 \sim 2750\text{\AA}$) from archival *GALEX* data (Martin et al., 2005) and claim that any reasonably close *GALEX* source to a *Chandra* position is very likely the true, physical UV counterpart with little to no ambiguity. Unlike other wavebands, the average *GALEX* field density ($m_{NUV} < 23$) in the GBS region is 5×10^{-4} sources per square arcsecond or < 1 per test circle of $10''$ (the mean *Chandra* error across the GBS being $\sim 3''$). Contrary to the deep optical imaging of G13 and W16 in no case does the number density of *GALEX* sources exceed 1 per *Chandra* error circle across the whole survey. With this spatial confidence, we iteratively assume that any optical/IR source corresponding to the *GALEX* position is then likely the true physical match in that waveband. Positional-matching to *GALEX* is the primary condition of acceptance for data to be selected and modelled in this study.

We then model the selected data against blackbody curves and a library of single-stellar templates. Although blackbody fitting is generally not a robust identifier of exact spectral/luminosity types (without knowledge of distance or $E(B-V)$ in advance), it is useful as a macroscopic identifier of UV or IR excesses originating from the primary, disk, accretion flow/spot, cool stellar companion or the presence of dust. From these, the UV emission is assessed versus known empirical limits on single-stellar activity and sources with unexplainably large UV are selected for a final UV-excess catalogue. A poor single-stellar fit occurs for one of three primary reasons: there exist multiple emitting bodies, inherent variability between non-simultaneous observations or the use of an incorrect counterpart in any band. The full scope of the SED modeling procedure and discussion of goodness-of-fit tests is found in Section 2.4. In this way, we produce corroborating evidence of high energy emission for number of previously identified CVs/qLMXBs from the GBS collaboration (CX93, CX118, CX137, CX426, CX645) and identify a new population of potential compact binaries.

Reliable SED fitting may also help locate a possibly large, unidentified

population of symbiotic systems in the galaxy where a white dwarf (WD) ionizes winds from a red giant donor (Kenyon and Webbink, 1984; Sokoloski, 2003). The known population of symbiotic systems may be biased towards shell-burning types which typically exhibit steady UV emission, and prominent optical emission lines in low-resolution spectroscopy, lines that are used historically as a primarily identification characteristic of symbiotics. *Non-shell* burning systems do not show such lines, and exhibit variable UV emission on short timescales interpreted as a flickering of the accretion disk (Luna et al., 2013). Mukai et al. (2016) identified SU Lyncis as a non-shell burning symbiotic star and identify *Swift* UVOT UV variability on sub-minute timescales. SU Lyn was observed twice in *GALEX*, and shows a difference of $\Delta m_{NUV} \simeq 2$ between 2006-2007 observations. *GALEX* UV timeseries data is available with the *gPhoton* package (Million et al., 2016) with time-sampling on the order of 1 second. This indicates thats red-giant identification via the SED in combination with *gPhoton* data could reliably identify SU Lyn-like systems in the larger context of an unidentified symbiotic population.

We first present the *GALEX* data and the counterpart-matching technique (Section 2.2), then describe the optical and IR datasets used to compile the SEDs (Section 2.3). Then we outline SED modeling methods (Section 2.4) and discuss the limits of single-stellar emission in the UV and X-ray (Section 2.5). Finally, we show the population results and interpret each candidate compact binary (Section 2.6).

2.2 UV Counterparts to the GBS

Here we outline the identification of UV, optical and IR counterparts using the *GALEX* UV positions as a basepoint for iterative matching of the latter two. We describe the *GALEX* dataset and its related astrometry/photometry, the *GALEX/Chandra* matching method with associated chance-match statistics

and end with summaries of each queried optical and IR catalogue.

2.2.1 *GALEX*: Photometry & Astrometry

The Galaxy Evolution Explorer (*GALEX*, Martin et al., 2005; Groot et al. 2018, in prep) surveyed most of the sky in the NUV and FUV, covering the majority of the GBS region save regions of high NUV density/large NUV background (see Section 2.2.2). For our purposes we use the *GALEX* all-sky imaging survey (AIS, depth of $m_{AB} \sim 21$ covering 26000 square degrees) and medium imaging survey (MIS, depth of $m_{AB} \sim 23$ covering 1000 square degrees) with 5σ depths of 20.8 and 22.7 mags respectively. The AIS has patchy coverage within 20 degrees of the Galactic plane due to the NUV detector safety limits, while the MIS specifically covered positions matching the SDSS spectroscopic footprint. The *GALEX* field of view is 1.25 deg^2 and the NUV filter has an effective wavelength $\lambda_{eff} = 2271 \text{ \AA}$ with effective width $W_{eff} = 730 \text{ \AA}$. Due to an early failing of the FUV detector our data is only in the NUV band. The NUV detector has a bandwidth of $1771 - 2831 \text{ \AA}$ and full-width-half-max (FWHM) resolution of $5.3''$ (Figure 2.1 shows the transmission profile of this filter). All *GALEX* photometric specifications are listed in Table 1 for convenience and taken from Morrissey et al. (2007). The rms astrometric error of unsaturated *GALEX* sources is $r_{rms} \leq 1''$ throughout the entire *GALEX* mission but for bright (still unsaturated) sources with $S/N > 18$, within 0.6 degrees of the center of each field of view $R_{rms} = 0.49''$ (Martin et al., 2005). Aligning *GALEX* to the SDSS catalogue reveals positional offsets of $(0.7'', 1.4'', 3.4'') = (1\sigma, 2\sigma, 3\sigma)$ for AIS and $(0.9'', 1.9'', 3.6'') = (1\sigma, 2\sigma, 3\sigma)$ for MIS¹. The astrometry of the AIS is slightly better than the MIS possibly due to small errors in the spacecraft dither pattern which accumulate in the more exposed MIS images. In order to balance obtaining many true UV counterparts while reducing the number of

¹http://www.galex.caltech.edu/wiki/Main_Page

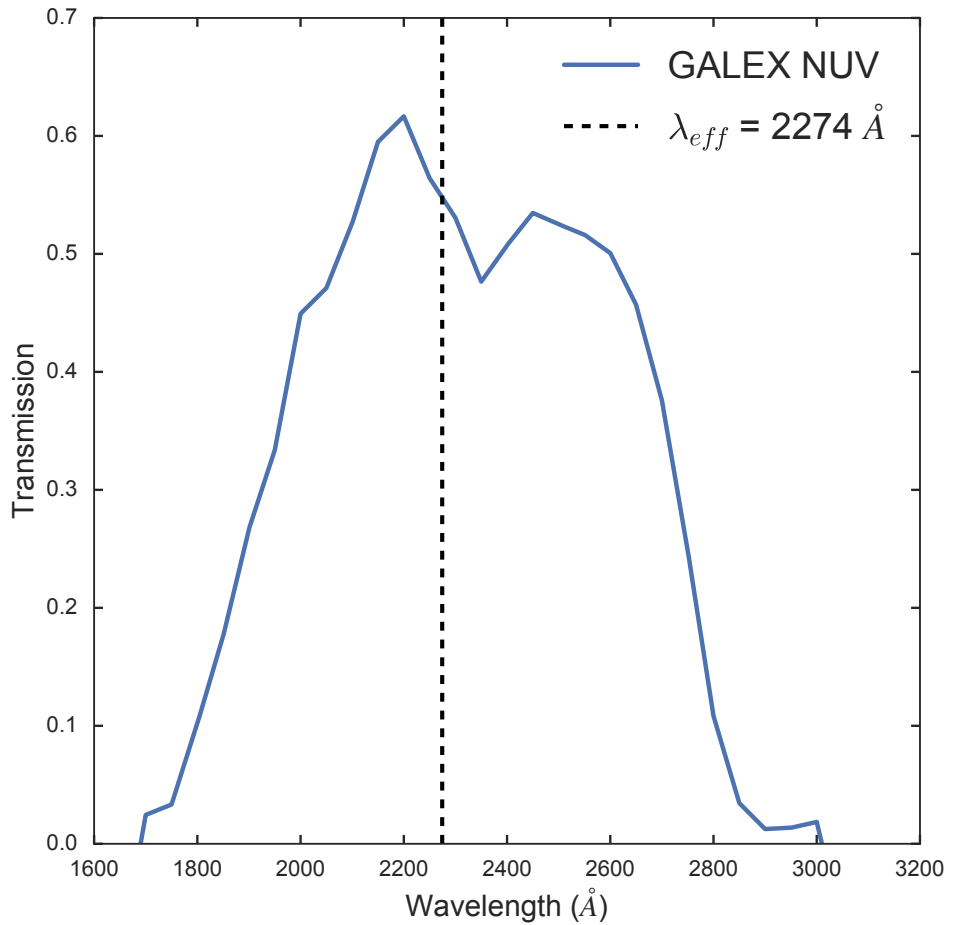


Figure 2.1: Near-ultraviolet (NUV) transmission band of *GALEX* with $\lambda_{eff} \simeq 2271 \text{\AA}$.

Table 2.1: Specifications of the *GALEX* NUV detector.

Item	<i>GALEX</i> NUV
Bandwidth	1771 - 2831 Å
Effective Wavelength	2271 Å
Field of View	1.24 deg
Peak Effective Area	61.7cm ²
Image Resolution	5.3" (FWHM)
Limiting Magnitude (5σ)	
AIS	20.8 AB mags
MIS	22.7 AB mags

false matches we use the 2σ error radii of each survey in quadrature with the 2σ *Chandra* positional errors. All *GALEX* data used in this work was taken in 2011. The predicted vs. measured count rates for the *GALEX* NUV detector diverge by $\sim 10\%$ at $m_{NUV} \sim 15$ or 311 cps (Morrissey et al., 2007). But, this divergence can be accounted for up to $m_{NUV} \simeq 10$ using the relation $\log(\text{MR}) = C_0 + C_1 \log(\text{PR}) + C_2 \log(\text{PR})^2$ where MR and PR are the measured and predicted count rates (respectively) and $(C_0, C_1, C_2) = (-0.314, 1.363, -0.103)$ (Morrissey et al., 2007). There are 23 *GALEX*-matched GBS sources saturated in the NUV band below $m_{NUV} < 15.0$, but all have $m_{NUV} > 10$ allowing us to correct each within our observed magnitude range.

2.2.2 *GALEX*: Data Collection & Reduction

We retrieved all *GALEX* data up to the most recent GR7 release in the spatial GBS limits by querying CasJobs². Retrieval coordinates were extended past the outermost region of the GBS to ensure edge sources were well surrounded by *GALEX*. The northern region of the survey is almost entirely covered by *GALEX*, but the southern has multiple gaps where saturation limits on the NUV detector restricted observations (see Figure 2.2). Strictly speaking, saturation in the NUV occurs where point sources are too bright

²<https://galex.stsci.edu/casjobs/>

$(F_\lambda > 6 \times 10^{-6} \text{ erg/s/cm}^2/\text{\AA}$ or 30 000 cts/s) or the sky background is too bright ($F_\lambda > 1.6 \times 10^{-11} \text{ erg/s/cm}^2/\text{\AA}$ or 80 000 cts/s). A unique *GALEX* source catalogue exists for regions where the *GALEX* explorer was operational in both the NUV and FUV (BCS Catalogue, Bianchi et al., 2014) but not for regions like the GBS where the FUV detector was inactive. Querying CasJobs yields many duplicate sources that appear in several *GALEX* fields of view and so the total number CasJobs returns highly overestimates the true number density.

Following the method outlined in Bianchi et al. (2014), we constructed a unique *GALEX* source catalogue in the GBS region by removing all sources that are within 2.5" of another ($\sim 2\sigma$ radial *GALEX* error). Within the more strict coordinate limits of the GBS there are ~ 95000 NUV sources before duplicate removal. After duplicate removal, there are ~ 81000 total NUV sources and an average *GALEX* source density of 5×10^{-4} sources per square arcsecond or < 1 per test radius of 10", while the mean *Chandra* error in the GBS is $\sim 3"$. The average surface density is found by dividing the total number of northern-region sources by the northern area, given the patchy southern coverage, assuming the surface densities in the north and south are equal.

2.2.3 *GALEX / Chandra* Counterpart Match Algorithm

For each GBS system we query the area within a unique search radius R_s defined by the quadrature sum of both X-ray and UV errors as well as spacecraft correction and a SDSS systematic offset term. The search error only differs from the quadrature radius defined in Wevers et al. (2016a) by the *GALEX* NUV term, but the R_s derivation is recapped for clarity. The first error term is the original 2σ *Chandra* positional error P (arcseconds) as a function of the number of X-ray counts C and the off-axis angle θ (Jonker et al., 2014; Evans

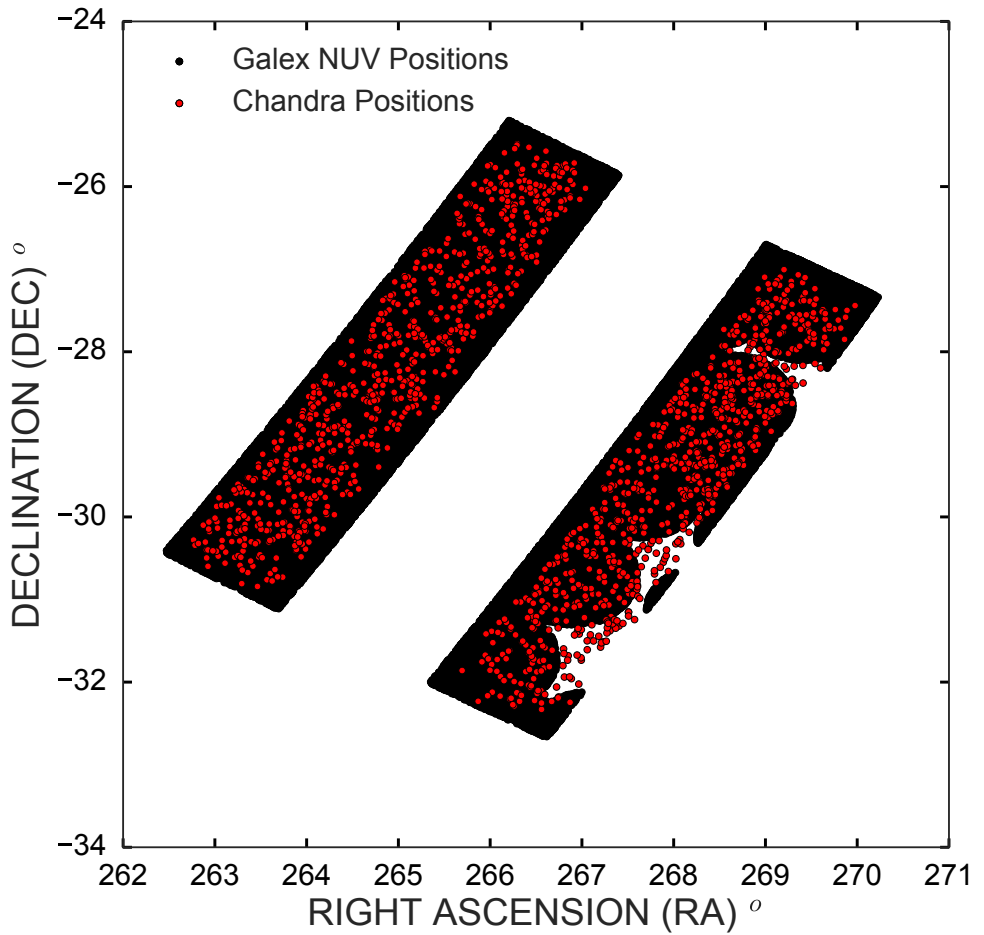


Figure 2.2: The *GALEX* NUV coverage of the Galactic Bulge Survey region. Black and red markers represent *GALEX* and *Chandra* positions respectively. The southern region has multiple, large gaps preventing a large number of *Chandra* sources from NUV match analysis.

et al., 2010):

$$\log(P) = \begin{cases} 0.1145\theta - 0.4957 \log C + 0.1932 & (\text{if } 0.0 \leq \log C \leq 2.1393) \\ 0.0968\theta - 0.2064 \log C - 0.4260 & (\text{if } 2.1393 \leq \log C \leq 3.3) \end{cases} \quad (2.1)$$

To this we add in quadrature the 2σ confidence level for the spacecraft pointing ($0.7''$) and the mean residual offset between SDSS observations and the *Chandra* source catalogue ($0.16''$ at 1σ , or $0.4085^{-1} \times 0.16''$ at 2σ , Primini et al., 2011). The final *Chandra* positional error becomes

$$R_X = \sqrt{P^2 + (0.7'')^2 + (0.4085^{-1} \times 0.16'')^2} \quad (2.2)$$

The distribution of R_X values is shown in Figure 2.3 with a mean value of $2.89''$. Finally, we add in quadrature the 3σ *GALEX* error radius $R_{UV}=3.0''$ (instead of 2σ to avoid skipping slightly distant UV matches in advance). The final search radius R_s is:

$$R_s = \sqrt{R_X^2 + R_{UV}^2} \quad (2.3)$$

Any *GALEX* object within this distance from a *Chandra* position is initially considered a real NUV counterpart, as the surface density is small (< 1 *GALEX* per $10''$ test radius circle) and $\langle R_s \rangle = 4.1''$. The distribution of *GALEX-Chandra* offsets is shown in Figure 2.4, and we find 222 sources with offsets $\Delta r < 3.0''$. Such small offsets lend more confidence to physical association between the X-ray and UV emitters in contrast to the optical and IR catalogues.

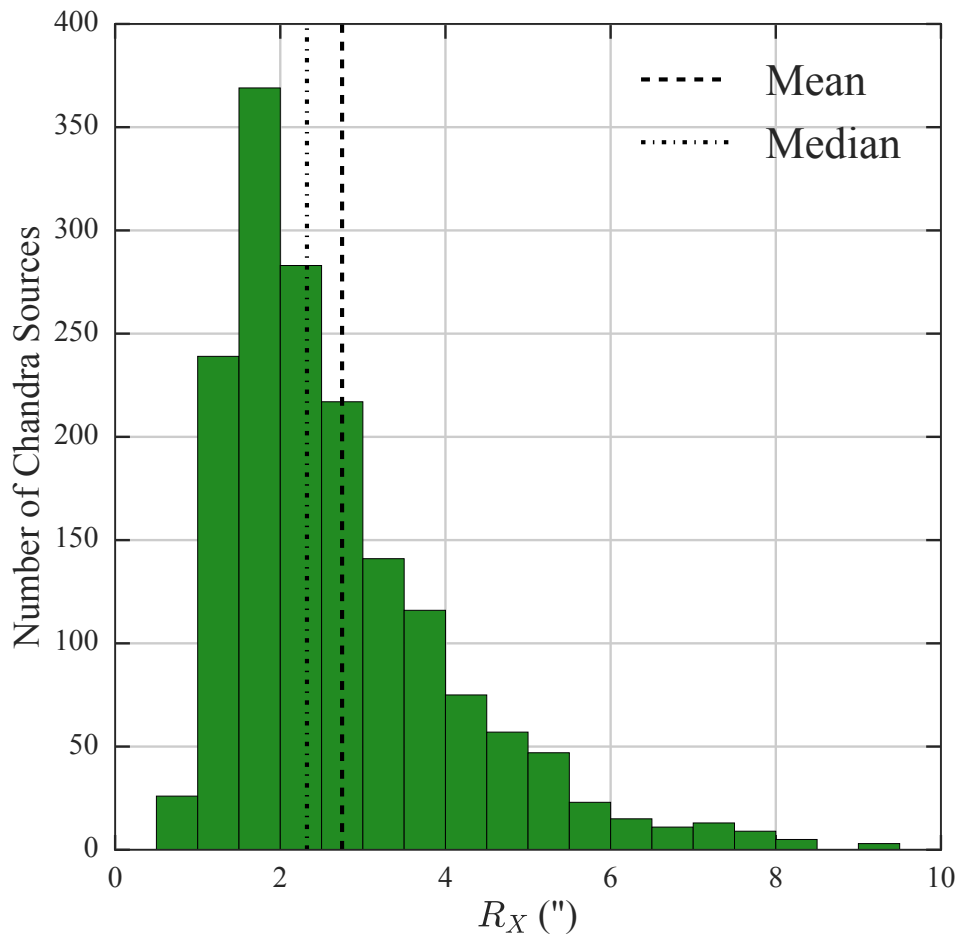


Figure 2.3: Distribution of *Chandra* positional error R_X for the 1640 GBS systems.

2.2.4 Quantifying the *GALEX/Chandra* Chance-Match Probability

By positional coincidence, some X-ray positions may have an interloping star in the same line of sight that is unassociated with the observed X-ray flux. The probability that a *GALEX* source is an interloper within R_s is found by shifting the entire unique *GALEX* source catalogue some amount Δd in a random direction (where the $\Delta d \gg R_s$) and observing the new number of *GALEX/Chandra* matches as a function of distance from *Chandra* positions. This method inherently preserves the spatial distribution of both *GALEX* and *Chandra* sources making this assessment relatively robust. We shift the *GALEX* set $\Delta d = 150''$ and repeat 1000 times to take an average. In general, this is a small set of 2D points (*Chandra* positions) within a much larger, denser field of ‘background’ 2D points (*GALEX*). Accordingly, we expect after shifting a linear relationship in the number of UV sources in R_s (as circular annuli increase in area $\propto r$) given by

$$N_{\text{false}}(r \pm dr) = (2\pi N_X \sigma_{UV})r = mr \quad (2.4)$$

where $N_X = 1640$ (total number of GBS objects) and $\sigma_{UV} \simeq 5 \times 10^{-4}$ arcsecond $^{-2}$, the average *GALEX* surface density here. These parameters define the expected, analytic slope to be $m = 2\pi N_X \sigma_{UV} \simeq 5$. This value is a slight overestimate given there are not 1640 sources within in the *GALEX* field; a large group of sources lie in regions lacking *GALEX* coverage in the southern fields (see Figure 2.2). We plot the distribution of matches at given offset r for both the true positions and the averaged shifted set in Figure 2.4 where each bin is 1'' in width. The large rise in matches at low offset indicates a population of real NUV counterparts in this initial distribution. Fitting the histogram of averaged, shifted offsets with a linear function anchored at (0,0) reveals the

number of expected chance *GALEX/Chandra* matches at offset r is

$$N_{\text{false}}(r) = (4.3 \pm 0.1)r \quad (2.5)$$

where the empirically derived slope has a standard error of 4.3 ± 0.1 . The cumulative number of chance matches in an offset range is the integral of Equation 2.5:

$$N_{\text{false}}(r_i < r < r_f) = 2.15r^2|_{r_i}^{r_f} \quad (2.6)$$

We tentatively separate each system into 3 groups, depending on their offset Δr : a high-confidence set (182 sources, where $\Delta r < 1.5''$, hereafter noted as ‘*GALEX Set 1*’), a medium-confidence set (55 sources, where $1.5'' < \Delta r < 3.0''$, hereafter noted as ‘*GALEX Set 2*’), a low-confidence set (43 sources, where $3.0'' < \Delta r < 7.45''$, hereafter noted as ‘*GALEX Set 3*’). The upper limit of $7.45''$ in *GALEX* Set 3 is simply because this is the farthest *GALEX* offset observed (except CX977 with $R_X \simeq 18''$ which we do not explore here). Large offsets are expected when the UV source is either unassociated with the X-ray emitter or when the *Chandra* data has particularly large errors. The expected number of chance matches in each *GALEX* Set is the cumulative function evaluated over the offset range multiplied by the fraction of *Chandra* sources with R_s at least that large. This latter point only affects Set 3 since the $R_{UV} = 3.0''$ is the lower bound on R_s , so the fractional-fix only applies to *GALEX* Set 3 (94%). Unfortunately, the number of expected UV interlopers in Set 3 exceeds the number observed making it difficult to argue that many (if any) of this group are real X-ray emitters. For these systems we refer the reader to Appendix A (the entire *GALEX/Chandra* set) for relevant photometry but do not discuss them individually leaving 222 sources from Sets 1 & 2 to identify with ~ 20 (10%) spurious detections. Final, expected chance match numbers in each offset range are displayed in Table 2.2.

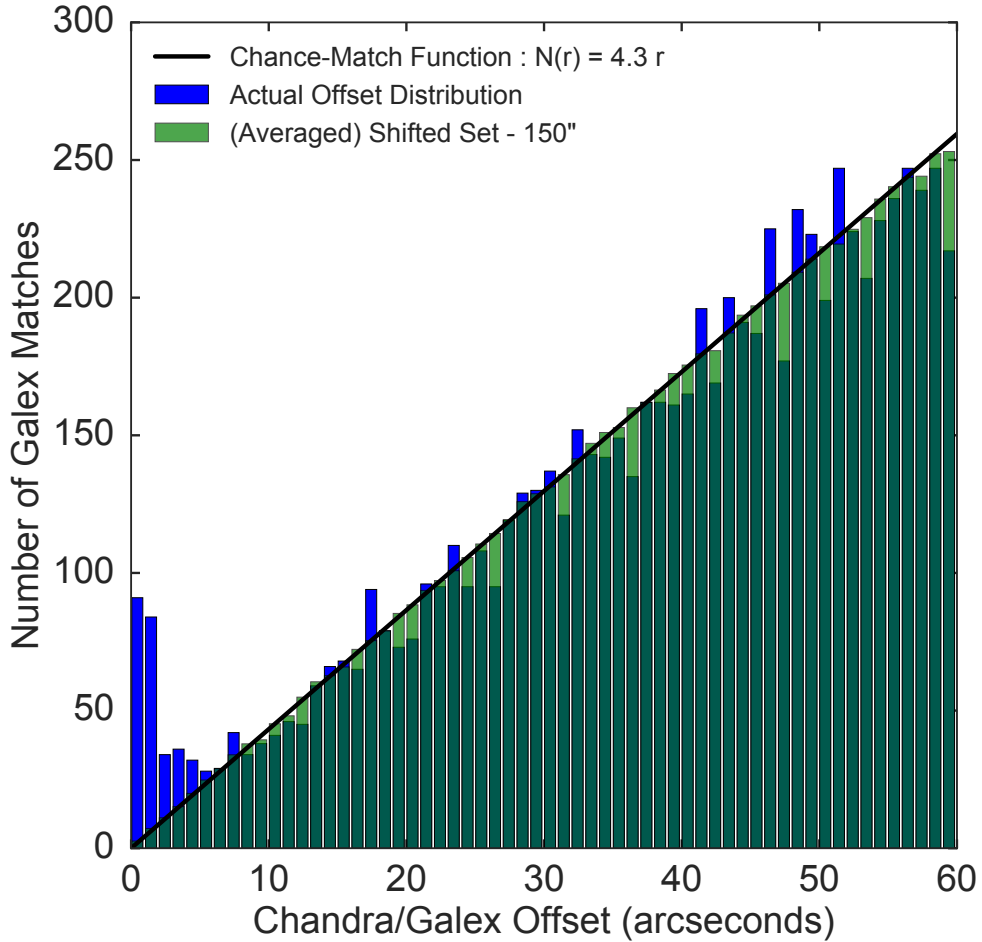


Figure 2.4: Distribution of radial offset ("") between *GALEX* and *Chandra* X-ray positions in the GBS. The blue histogram represents the actual spatial distributions of the two sets while the green histogram represents the matches between the randomly shifted sets. The black line is the best linear fit to the green, shifted histogram and depicts the expected number of false *GALEX/Chandra* matches at an offset of r arcseconds. The rise in the blue histogram between 0 and 5" represents a population of true NUV counterparts.

Table 2.2: The number of *GALEX* chance matches in each set defined by offset from the best-fit X-ray position. Numbers are computed using the cumulative function in Equation 2.6.

<i>GALEX</i> Set	Offset	Actual Matches	Expected Chance
1	$r < 1.5''$	138	4-5
2	$1.5'' < r < 3.0''$	84	15-16
3	$3.0'' < r < 7.45''$	47	50-53
TOTAL	$r < 7.45''$	269	69-74

2.3 Optical & Infrared Counterparts to the GBS

Optical and IR counterpart lists for the GBS have been produced in the SDSS r' and i' bands as well as standard J,H and K_s by Wevers et al. (2016a) (herein noted as W16) and Greiss et al. (2013) (herein noted as G13) respectively. In both papers, every potential match is assigned a false alarm probability (FAP), a function of both local brightness density and distance to the X-ray position that represents the % chance that an optical/IR point is an interloper. Many GBS systems have > 1 optical/IR sources within R_X with comparative FAPs - it is in these cases that using UV position is of utmost importance.

First, from these lists, we select those sources that also fall within the corresponding *GALEX* error radius which we will call R_{UV} ($3.0''$). We examine the following possibilities:

1. One source resides in R_{UV} : this source selected as the real counterpart
2. Multiple sources reside in R_{UV} : of these, the source with the lowest FAP from G13/W16 is selected as the real counterpart
3. No source resides in R_{UV} : the source with the lowest FAP from G13/W16 within R_X is taken to be the true counterpart (as would normally be done without regards to this UV-matching procedure)

When multiple sources are within R_{UV} , FAP values determine the selection of the counterpart, but for all other optical/IR datasets (outside of G13/W16) FAP values are not constructed or used. For those data, we select sources

corresponding to the W16 and G13 positions when these are available. If not, we select those that match closest to the *GALEX* position, and iteratively match each successive dataset to an already identified optical or IR source.

2.3.1 Data: Optical Counterparts

MOSAIC-II

W16 found optical counterparts within R_X in the GBS using the MOSAIC-II imager of the 4-m Victor M. Blanco telescope at CTIO, Chile in the bands r', i' and H α ($\lambda_{eff} = 6163, 7695, 6561 \text{ \AA}$ respectively). In the most (least) conservative estimates of W16, 954 (1160) out of 1640 total GBS sources have multiple counterparts within R_X . They compute two statistical quantities for each match: a FAP and a likelihood ratio (LR). The FAP is a function of the local brightness density around a GBS object and represents the probability that any particular optical source is not in fact the correct counterpart. Qualitatively, the FAP states that a source that is closer, and/or brighter than the average brightness of optical sources in the region around the GBS source is more likely to be the true counterpart. Thus a source with a lower FAP is more likely a true counterpart. The likelihood ratio, LR, is defined similar to that in Sutherland & Saunders (1992) and is the relative probability of finding the counterpart at a particular offset and magnitude versus a background source with the same characteristics. It is a function of magnitude m and Δr the distance between the X-ray position and the optical position. Qualitatively, it states that a source that is closer to the X-ray position is more likely to be the true counterpart. The bounds of the FAP are [0,1] and the bounds of the LR are [0,∞] as this is a relative probability. W16 finds that for the most (least) conservative estimates that in 91% (88%) of cases the counterpart with the lowest FAP also has the highest LR. Sources where these values do not agree can be visually explained on a circumstantial basis (such as a very bright

source being near the edge of the error circle). MOSAIC-II data is especially helpful in combination with VPHAS+, as they both have two similar bands in SDSS r' and i' lending confidence to any one optical source.

TYCHO-2

Many *GALEX*-matched GBS sources will be bright and/or close and likely have a Tycho-2 (Høg et al., 2000) optical counterparts. Tycho-2 has two filters B_T and V_T and surveys the sky with 99% completeness at $V < 11.0$ (and 90% at $V < 11.5$) capturing many bright and close systems. All J2000 positions of Tycho-2 sources in the GBS region are corrected using known proper motion values up to J2011 when *GALEX* observations were taken. Under the expectation that *GALEX* emitters are close, accounting for proper motion may be important, and we find a mean proper motion of $0.2''$ with a maximum 11 year motion of $3.3''$ for Tycho/*GALEX* matches. Hynes et al. (2012) (herein noted as H12) matched GBS sources to Tycho-2 and found 69 sources within $10''$ of *Chandra* X-ray positions. These 69 sources were reduced to a likely 60 Tycho-2/*Chandra* matches after removing chance matches and duplicate observations. Most of these are late-type single stars and we expect a large portion to be UV emitters - we find 48 initial Tycho-2/*GALEX* matches. CX59, CX77, CX388, CX622, and CXB93 do not show Tycho-2 matches in our algorithm but are quoted as such in H12 (we use true X-ray error radius of the *Chandra* position while H12 uses a $10''$ cut) and so images are manually inspected for each of these cases as to not miss any bright counterparts. We consider CX59, CXB93 and CX622 as true Tycho-2 matches and CX77, CX388 chance matches after an examination of the optical images with respect to the *GALEX* position.

The Tycho-2 filters are typically transformed to standard Johnson B and V using the linear transformation provided in Høg et al. (2000), but this is defined for unreddened main sequence stars and in reality depends on the luminosity class and reddening. For more accurate photometry we cubically interpolate

Table 2 of Bessell (2000) which accounts for empirical differences in $(B - V)$ and $(B_T - V_T)$ that are largest for $0.25 < (B_T - V_T) < 1.5$ (see Fig. 4 of Bessell, 2000).

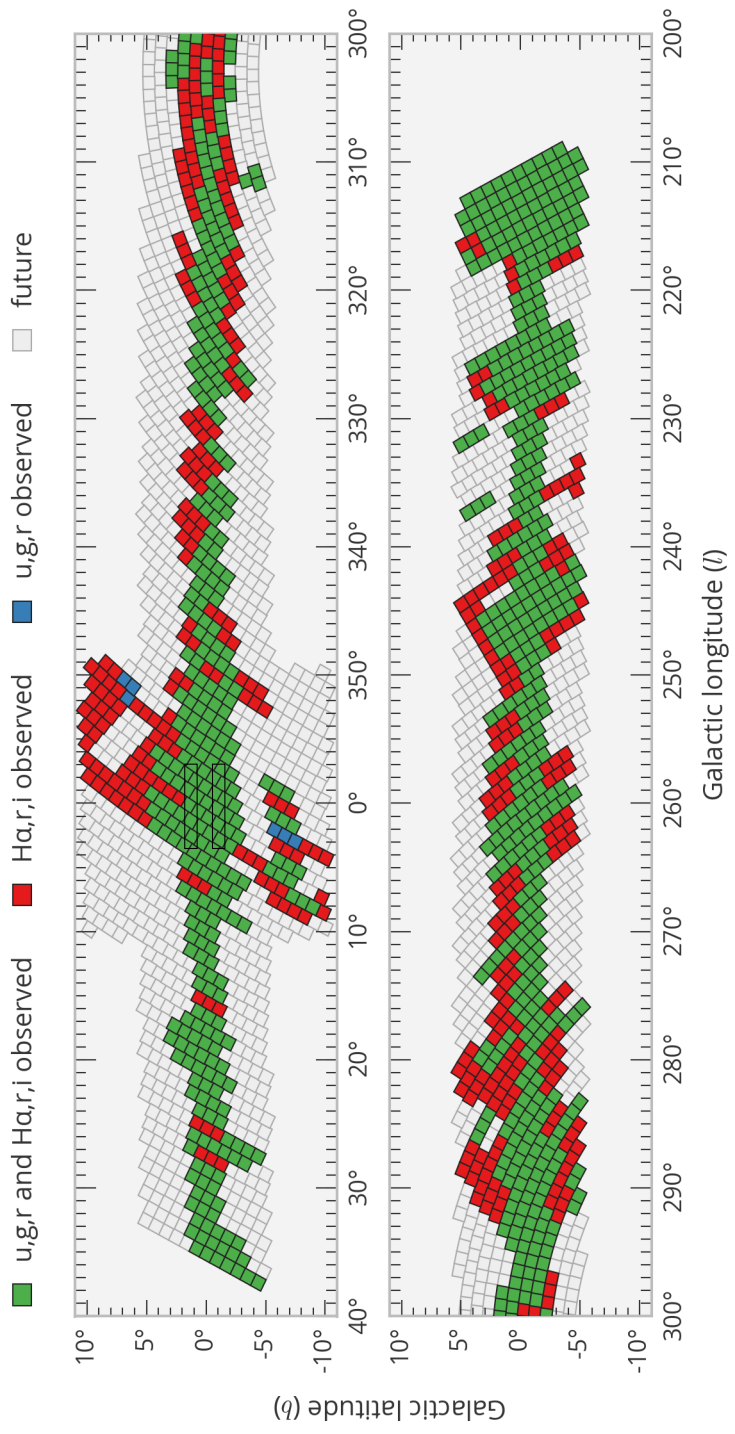
VPHAS+

Many sources are not bright enough to be Tycho-2 sources ($V \geq 11.5$) but are saturated in MOSAIC-II r' and i' data ($r' < 17.0, i' < 16.0$). This leaves some SEDs with large gaps between the NUV and NIR. Given a single datapoint in the NUV and a much higher chance match probability in the NIR, a lack of optical data leaves the SED heavily unconstrained.

The VST Photometric H α Survey of the Southern Galactic Plane and Bulge (VPHAS+, Drew et al., 2014) surveyed the southern Milky Way in SDSS u, g', r', i' as well as H α at ~ 1 arcsec angular resolution at a depth of $\simeq 20$ mags and a typical astrometric error of 1''. The survey's purpose was to optimize a search for complex and/or small nebulae of all types like ultra-compact and compact HII regions, nebulae from YSOs and PNe and even extended emission from D-type symbiotic stars and supernova remnants. It also adds greater depth to H α emission line candidates enveloping all types of massive stars, pre-main sequence stars, active stars and compact binaries. VPHAS+ covers the entirety of the GBS region (see Figure 2.5). VPHAS+ survey field acquisition began on 2011 December 28 using the OmegaCAM imager (Kuijken, 2011) on the VST which provides a field size of a full square degree captured on a 4×8 CCD mosaic. Calibration is done by observing standard star fields observed each night (e.g., Landolt, 1992). VPHAS+ data is initially sent to the ESO raw data archive in Garching for first processing followed by reduction at the Cambridge Astronomical Survey Unit (CASU³).

³<http://casu.ast.cam.ac.uk/>

Figure 2.5: The VPHAS+ footprint. The GBS region is shown as two black, bolded boxes in the upper portion and is wholly covered by this survey (Drew et al., 2014).



APASS

Along with Tycho-2, MOSAIC-II and VPHAS+ we query the on-going AAVSO All Sky Photometric Survey (APASS, Henden et al., 2009) observations in Johnson B, V and SDSS g', r' and i' with ~ 2.5 arcsecond angular resolution to a depth of ~ 17 mag. The survey's purpose is to fill the completeness limit between Tycho-2 observations at $V_T \sim 11$ and NIR surveys like SDSS, PanSTARRS, VISTA and VST at saturation limits of $V \sim 15$. This catalogue⁴ contains 60 million stars over roughly 99% of the sky in over 400000 total images, although the survey is still in completion. APASS saturation limits are magnitudes > 10 in the B, V, g', r' bands and > 9.5 in i'. Northern observations were taken at Dark Ridge Observatory at Weed, NM, USA and southern observations at CTIO. All processing is done via an automated software pipeline at both the observing site and AAVSO. Observations were taken using a 20 cm telescope using Apogee U16m CCD cameras with 7-position filter wheels. The overlap between SDSS g', r' and i' bands between VPHAS+ and APASS allows a greater certainty of confidence for a given optical counterpart given their different angular resolution values. In some cases we retrieve different fluxes for a source between the same SDSS bands in the 2 surveys, which either indicates variability or a confusion of sources between the catalogues.

2.3.2 Data: Infrared Counterparts

2MASS, VVV, UKIDSS

G13 compiled near-IR (NIR) counterparts within $10''$ of each GBS system from archival searches of Two Micron All Sky Survey (2MASS, Skrutskie et al., 2006), VISTA Variables in the Via Lactea (VVV, Minniti et al., 2010) and the United Kingdom IR Telescope Deep Sky Survey (UKIDSS, Lucas et al., 2008). Every GBS system has at least one NIR counterpart, while $\sim 71\%$ of the GBS have

⁴<https://www.aavso.org/apass>

> 1 NIR counterparts. For scale, the mean number of NIR matches is 6 with a maximum of 30 within $10''$. Each source has an associated FAP for each source similar to that of W16, using the brightness relative to the local brightness density as well as distance to the best-fit X-ray position. Reasonably, G13 find that in 98.7% of cases the closest source to the X-ray position has the lowest FAP (the 1.3% left are brighter sources slightly farther from the X-ray position, like W16). Sources with the lowest FAP are noted as the most likely match in G13. We find that most *GALEX*-matched GBS sources have a low-FAP 2MASS counterpart in the standard J, H & K_s bands. The computed FAP values depend on the K_s band flux; 4% of the VVV matches do not have a K_s magnitudes and thus do not have a FAP value listed, usually due to saturation in one or multiple bands. We also find this NIR catalogue is incomplete; we find visually-obvious, catalogued 2MASS sources within $10''$ of some systems that are not in the G13 catalogue. We produce an updated, external list of 2MASS sources as reference. If a VVV source with no FAP value is picked by the algorithm, we replace it with its missing 2MASS counterpart if possible for unsaturated multi-band photometry.

In Section 2.6 we will use the J, H, K_s colours to infer properties of potential donors. As a reference, we use main-sequence 2MASS colours from the online compilation by Eric Mamajek⁵, and convert all VVV colours to 2MASS using the linear transformation parameters given by Equations 2 & 4 in Soto et al., 2013.

WISE & GLIMPSE-3D

Mid-IR counterparts can be useful for SED fitting given the large number of unique bands available in surveys like WISE & GLIMPSE. The Wide-field IR Survey Explorer (WISE, Wright et al., 2010) data were extracted for systems in the bands W1, W2, W3 & W4 ($\lambda_{eff} = 3.4, 4.6, 12, 22\mu m$ respectively) us-

⁵http://www.pas.rochester.edu/~emamajek/EEM_dwarf_UBVIJHK_colours_Teff.txt

ing the TOPCAT package (Taylor, 2013). This is done after cross-matching our set with G13 in which many sources have 2MASS counterparts. Since 2MASS sources are often previously correlated with a WISE source in the IRSA database a confident 2MASS counterpart lends confidence to the corresponding WISE match and vice-versa. WISE is also deeper than 2MASS by roughly a factor of 4 in the limiting flux (see Table 1 of Thiessen et al. 2016) and so we anticipate many sources in 2MASS will also have a WISE match. Unfortunately the wide PSFs of the W3 and W4 filters (roughly 7'', 12'' respectively) provide large blending effects and in many cases we are not confident in selecting a match. In a similar fashion, we matched the Galactic Legacy IR Mid-Plane Survey Extraordinaire (GLIMPSE-3D, Benjamin et al., 2003; Churchwell et al., 2009) data to *Chandra* positions in 4 Spitzer mid-IR bands ($\lambda_{eff} = 3.6, 4.5, 5.8, 8.0\mu m$) using the TOPCAT package. Like WISE, these data usually contains a corresponding 2MASS source and in the majority of cases this matches the lowest FAP 2MASS counterpart in G13 data. Finally, the wavelengths of WISE & GLIMPSE filters exceed the wavelength range of stellar templates, which extend only slightly past the 2MASS K_s band. Accordingly these surveys are used for blackbody fitting, but not *spectral* fitting.

2.3.3 Complementary UV Data: *Swift* UVOT

After a final UV-excess dataset has been extracted, each system is manually checked in *Swift* Ultraviolet Telescope (UVOT⁶, Roming et al., 2005) images for matches in 6 bands (UV bands UVW1, UVM2, UVW1 at $\lambda_{eff} = 2030, 2228, 2589 \text{ \AA}$ and optical and U, B, and V). UVOT is co-aligned with the *Swift* X-ray Telescope (XRT, Burrows et al., 2005) and can provide simultaneous X-ray, UV and optical measurements (170 – 650 nm) in a $17' \times 17'$ window. We find only 5-10 sources in these pointings, but where they exist the UV filters

⁶https://Swift.gsfc.nasa.gov/about_Swift/uvot_desc.html

add significant information to the SED: the UVW2 filter constrains the FUV and ultimately $E(B - V)$, while the UVM2 filter is close enough to *GALEX* to suggest time variability when mutually inconsistent. Lastly, Fielder et al. (2018, in prep) conducted a similar analysis to ours using *Swift* pointings but their coverage of the GBS is fairly small.

2.4 Identification of Compact Binaries via the SED

2.4.1 SED Modeling and Goodness-of-Fit

The main goal of this work is to identify potential compact binaries via SED analysis. We aim to observe and classify NUV emission in excess of empirically observed upper limits on single-stellar systems indicative of compact binaries. We identify both a set of compact systems and a much more numerous set of likely close, active late-type stars. It is the former that the bulk of discussion will be focused on, but we stress the importance of classifying a large number of single-stars: it significantly reduces the total number of identifications in the GBS, while singling out those systems worthy of spectroscopic follow-up. It also allows a more efficient allocation of telescopic time for future observations.

Initially we try modeling each source as a single star using stellar templates from the Pickles (1998) Library spanning the UV to the IR, in combination with the Python package `pysynphot` (Lim et al., 2015) for a robust manipulation of spectra in combination with extinction and bandpass integration. The only free parameters in modeling a source at a given spectral type are the normalization N and $E(B - V)$. We model each system over a range of fixed $E(B - V)$ from 0 to 1 in steps of 0.1 (with the standard Galactic extinction curve, $R_v = 3.1$ (Cardelli et al., 1989). For each source, at a fixed $E(B - V)$, we compute the best normalization N for all 131 Pickles templates and select that with the

lowest χ^2 statistic. To simulate the reality of a filter observing a total flux over its filter width, as integrate each flux value over the transmission profile of the appropriate filter. Unless mentioned otherwise, all fitting procedures with measured fluxes integrate over the filter. We repeat this procedure *excluding* the *GALEX* NUV point to assess the importance of this filter observation on our interpretation of the source. If a fit is effectively unchanged with the NUV point, the NUV emission is likely photospheric in origin. Our use of 269 sources, 131 templates, 10 extinction values with and without UV yields $\sim 7.3 \times 10^4$ initial models.

Frequentist SED curve-fitting assumes each fit parameter is fully independent with a Gaussian prior distribution. In reality temperature T , normalization N and extinction are mutually degenerate and can make SED interpretation ambiguous in cases when priors are wide. For a single template or blackbody fit the degeneracy manifests as an exchange between T and N as extinction rises; we retrieve hotter stellar fits for high extinction. To show this, consider the SED-modeling results of CX22 (Figure 2.6): it is statistically well-fit by both a K0V and G5V, but at different $E(B - V)$ values. In this case, we claim that CX22 is consistent with a single-stellar template, despite not knowing the true $E(B - V)$ value in advance. A Bayesian approach can be helpful, especially when we know one or more parameters to some reasonable accuracy (e.g., distance/extinction, donor temperature from the IR, etc.) We discuss the Bayesian binary-fitting methods for the final set in Section 2.4.2. In the future, accurately calibrated distance estimates will be available from Gaia parallaxes (Gaia Collaboration et al., 2016) which will constrain $E(B - V)$ and normalization using current dust maps (e.g., The 3D Milky Way Dust Map, Green et al., 2015). Spectral goodness-of-fit is found by minimization of χ^2 , and in some cases we obtain (with survey-quoted photometric error) a reduced chi-squared value less than the threshold value for 90% confidence and a given number of degrees of freedom. However, we do not reasonably expect to reach such pre-

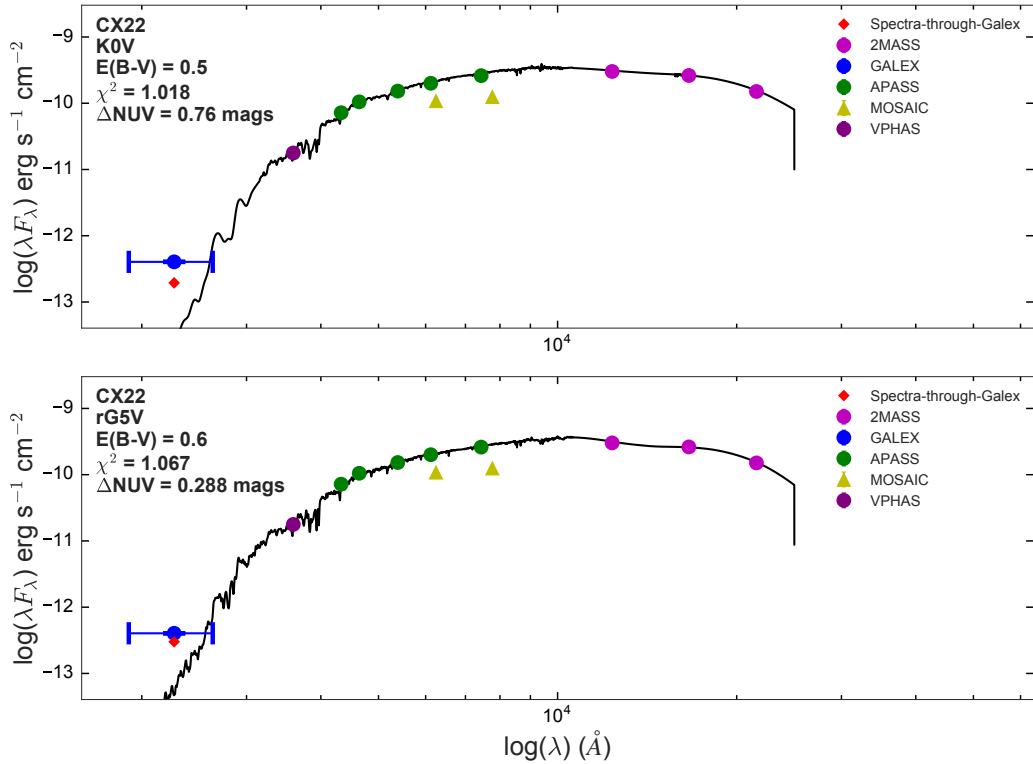


Figure 2.6: GBS source CX22 is well-fit ($\chi_{\nu}^2 < 1.67$ for 8 dof) by a single stellar template at two different values of $E(B-V)$ (K0V for 0.5 and a metal-rich G5V for 0.6) though with different spectral types and normalization, displaying the degeneracy between temperature, normalization and $E(B-V)$. Saturated points are represented as triangles. The red diamond is the spectrum flux folded through the *GALEX* NUV filter and the blue, observed *GALEX* point is displayed with a horizontal bar showing the effective width of the filter ($\simeq 730\text{\AA}$). Photometric errors are the original, survey-quoted errors. CX22 is consistent with a single-stellar X-ray/UV emitter with 57 X-ray counts in *Chandra* and a slight NUV excess beyond photospheric emission due to an active chromosphere.

cision even for known single-stars for several reasons. Given the observational bias of our data towards active single stars, cool binaries and compact systems, photometric variability if on the scale of photometric errors can skew spectral fitting. Despite this, it is often clear from previously identified periodicity or variability in prior collaboration papers that, in combination with a scattered optical/UV section of the SED, a system is binary in origin. Optical variability has already been recognized in many GBS sources - Udalski et al. (2012) found 209 optically variable GBS sources while Hynes et al. (2012) found 10-20 Tycho-2 matches in the All-Sky Automated Survey (ASAS) Catalog of variable stars (Pojmanski, 2002). Britt et al. (2014) studied optically faint, variable counterparts yielding 165 sources with a range of physical interpretations.

Physical stellar differences in radius, temperature and metallicity within a common spectral type can reduce the accuracy and precision of photometric inferences. To show this, we consider a simulated observation of a K4V spectrum from the Bruzual-Gunn-Persson-Stryker Atlas (BGPS, available in the `pysynphot` STScI package, Gunn and Stryker, 1983; Lim et al., 2015) over 8 bandpasses (*GALEX* NUV, APASS B, V, r, i and 2MASS J, H, K_s). Treating this source as if we observed it in the *GALEX*/GBS dataset, we determine the fit spectrum from a different spectral library, the Pickles Library, using simulated photometric errors of 1% of the F_λ value in each band (typical of actual survey errors in our work). Figure 2.7 shows the result with the top/bottom fits without and with *GALEX* NUV, respectively. The best-fit Pickles template in each case was *not* a K4V despite our simulated observations coming from a K4V template from another library; the reduced chi-squared statistic is poor, despite this simulated observation originating from a known single star. This leads us to conclude that precision of SED-fitting with template libraries may be only accurate to within a few spectral sub-types. Nevertheless our intent is not to make claims about spectral types to the degree that a fine spectrum would but find reasonable fits to single-stellar templates. As well as photomet-

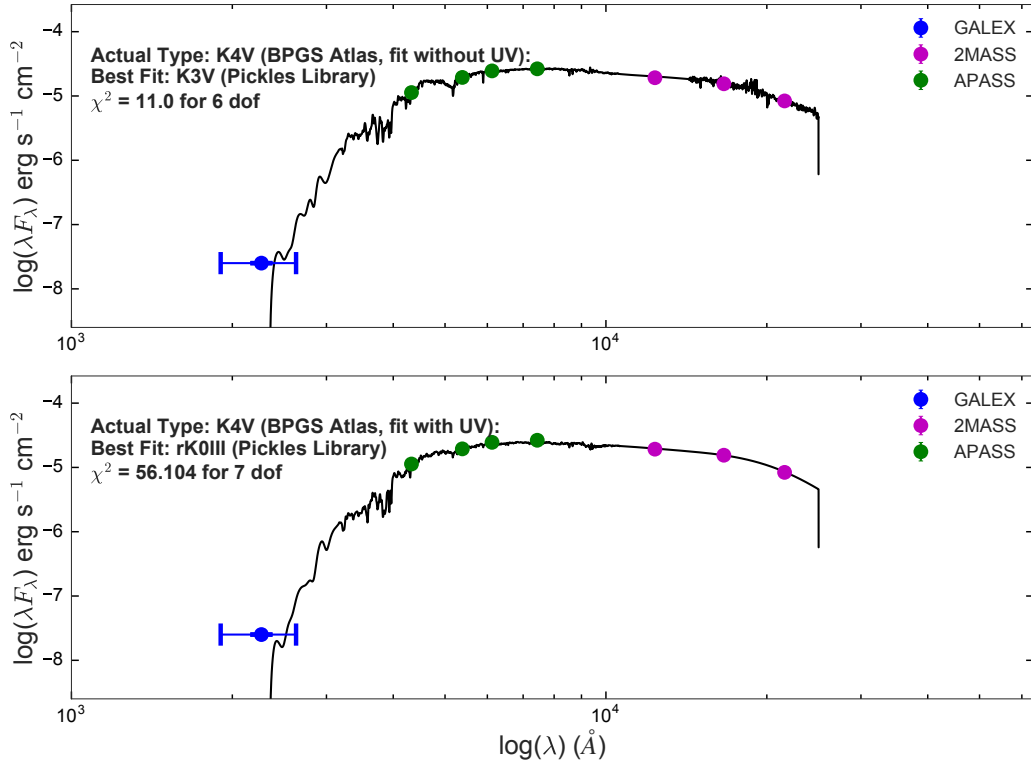


Figure 2.7: Spectrum for the star HD154712 from the BGPS Library was artificially observed through 7-8 bands from the UV through the IR, and fit with templates from the Pickles Library. Despite being a simulated observation from a template K4V, the best fit with and without UV (top, bottom respectively) are a metal-rich K0III and a K3V displaying the scatter even in a single spectral type between template libraries.

ric variability and physical variations in stellar characteristics, the step-size of the extinction range, underestimated photometric errors and systematic differences between surveys also affect the chi-squared statistic to the point where a single star may be unable to be confidently identified as such by this alone.

To mitigate the effect of all discussed errors, we increase all photometric errors *below* 0.1 magnitudes up to 0.1 leaving all those larger than 0.1 intact. We choose 0.1 as this limit as it is the largest mean error of all of the surveys; Tycho-2 has a mean error of 0.1 mag across all catalogued stars and 0.013 mag for $V < 9.5$. The empirical mean error of Tycho-2 stars matched in our survey is also $\simeq 0.1$. Most importantly, we believe this will mitigate the systematic differences between the errors quoted in each survey, as well as leaving errors that are known to be even larger than 0.1 to represent a relative ignorance in these values. Finally, systems that are well-fit (by the χ^2 statistic) with all photometric points, including the UV, are considered plausible single-stellar sources. Systems that are only well-fit *without* the UV point have their UV excess compared to the power-law relation (Equation 2.7) to determine if chromospheric activity can account for such activity levels. Systems poorly-fit in both cases are set aside and examined on a case-by-case basis.

2.4.2 Multi-Component Modeling: A Bayesian Approach

For those sources that show signs of binarity in final UV-excess sources, we model the two-body system to assess the plausibility of two emitting bodies (hot and cold components) using a Markov-Chain Monte-Carlo technique (MCMC) with the python package *emcee* (Foreman-Mackey et al., 2013). MCMC algorithms are good for one primary problem: effectively sampling an unknown posterior distribution, such as the likelihood of some photometric data fitting a given emission model. We employ MCMC fitting with 5 fitted parameters: temperature T , normalization N (for both bodies) and extinction $E(B - V)$. Prior distributions are chosen as wide Gaussian distributions centered at the

best-fit parameter values derived from a frequentist approach (assuming no extinction). A Bayesian approach is well-suited for this model considering the heavy degeneracies in T , N and $E(B - V)$; frequentist approaches may settle into local minima of the parameter space before sampling wider combinations of the fit parameters. To show the level of degeneracy for the two-body system, we show in Figure 2.8 a known CV (CX93, Ratti et al., 2013) where we have used the suggested K5V donor in combination with a hot component, fitting for T_{bb} , N_{bb} , N_{spec} and $E(B - V)$. The ‘corner plot’ (Foreman-Mackey, 2016) of the combined Bayesian posteriors is shown on the right with the best-fit parameters shown; note the contoured correlations in parameter space. Two-body modeling is quite sensitive to the SDSS u’ band, as well as any alternate information available via *Swift* UVOT. It is difficult to retrieve sensible two-body fits if *only* the UV is in excess without a correlated rise in the optical *into* the UV region.

2.5 UV & X-ray Emission of Chromospherically Active Stars

A large fraction of *GALEX/Chandra* systems will be chromospherically active, late-type MS stars. Late MS dwarfs are X-ray emitters up to $L_X \sim 10^{31}$ erg/s in large part due to the interaction of the coronal/chromospheric plasma with large-scale stellar magnetic fields. These active systems can be observed as SEDs that are well-fit in all points *excluding* the NUV; coronal activity and its effect on the NUV is probably poorly sampled in template libraries. Chromospheric processes span the length of the entire electromagnetic spectrum (see Hall, 2008 for a thorough review): of direct importance are the UV and X-ray. Soft, thermal X-rays are emitted in hot coronae (10^7 K) while the hardest X-ray emission probably stems from flare events (like that of the Sun) where energetic electrons stream back through the ambient chromosphere after mag-

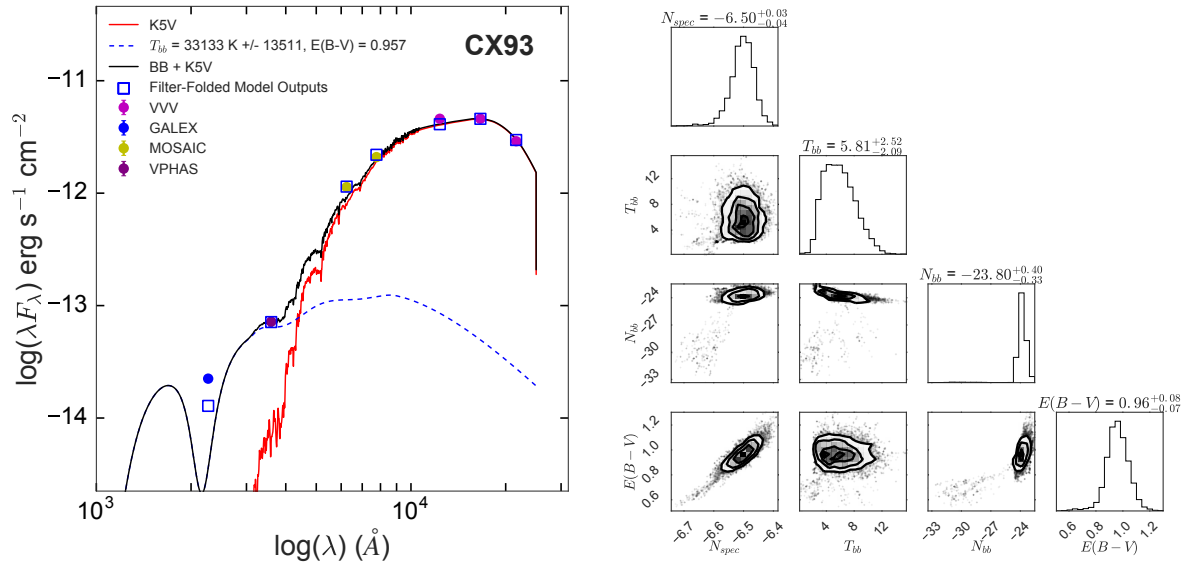


Figure 2.8: (left) The MCMC model of the low accretion-state CV CX93 (Ratti et al., 2013) with a hot blackbody primary and K5V donor spectrum. (right) The triangle plot of fit parameters, showing the sampled parameter space combinations. Temperature is in T_\odot , and each normalization value N is actually the logarithm of the value.

netic reconnection (thick-target bremsstrahlung). Strong optical emission in the form of H α and Ca II H & K emission line cores are found in active stars from a combination of the temperature inversion and lower ion densities in the chromosphere, and these emission cores often constitute the definition of late-type activity (West et al., 2008) summarized by the activity index R'\$_{HK}\$. The production of chromospheric activity by the stellar dynamo is still not fully understood in the context of rapidly rotating stars but it is well-observed that the ratio log(L_X/L_{bol}) saturates at ~ -3.0 (Vilhu and Rucinski, 1983; Vilhu, 1984)) with a ‘supersaturated’ regime wherein the X-ray luminosity decreases with increasing rotation rate past the saturation point (Prosser et al., 1996). It is unclear what the expected range of NUV excess for all MS stars should be, partially as a result of the relative paucity of detailed study in the UV regime from heavy intraGalactic extinction. The coronal X-ray emission from the close F-M dwarf population appears to have no specific relation to spectral class, but a lower cut-off of surface X-ray flux at log(F_X) ~ 3.7 exists across the whole set (Figure 8 of Schmitt, 1997). Then, the *ratio* of X-ray flux to optical is largest for M-type increasing to K, G then F. M-dwarf stars only produce a small fraction of their blackbody emission in the NUV (or optical for that matter) from the photosphere. Assuming the coronal NUV and X-ray emission are positively correlated (e.g., they are both related to the same base mechanism of production), we expect M-dwarfs to exhibit the highest NUV excess *relative to its photosphere* for any X-ray luminosity. M-dwarf stars also have the largest convective turnover time τ_c on average, meaning that at similar rotation rates to other stars M-dwarfs will have lower Rossby numbers and thus be more active. For the final set of compact binary candidates, we need to rule out stellar activity as the driver of UV excesses. To do so we use the range of M-dwarf NUV excesses as a working upper limit. Stelzer et al. (2013) studied the X-ray and *GALEX* NUV emission from M-dwarfs within 10 pc of the sun in both the FUV and NUV and found that all M-dwarfs have a chromopsheric

component in the *GALEX* NUV filter and generally that chromospheric, not photospheric emission dominates the *GALEX* NUV observations. Ultimately, they derive a power-law between the surface X-ray and surface (excess) NUV flux of the 46 M-dwarf sample:

$$\log(F_{UV}) = (0.80 \pm 0.36) + (0.83 \pm 0.06)\log(F_X) \quad (2.7)$$

Note here that the surface NUV is the *excess* NUV flux after subtraction of the photospheric contribution. We also note the updating of these values in the erratum Stelzer et al. (2014) from the original paper. To assess the UV excess of a source, we choose a companion using the IR colours and convert the observed X-ray and UV fluxes into that at the surface using the stellar radius and assuming a test distance of 100 pc. M-dwarfs show the largest NUV excesses relative to the photosphere, while there is no strong dependence of X-ray flux with spectral type. Active, non-M class systems should span the range of the X-axis in Figure 2.15 but fall short of the log-log relation in the Y. It should be noted that X-ray emission from A-M *giants* has been observed at a few 10^{27} erg/s and possibly some up to $\sim 10^{28}$ erg/s (Hunsch et al., 1998b,a) though this is considerably less than observations of dwarfs. There exists an X-ray dividing line at \sim K3 where giants to the *left* in the HR diagram are observed in the X-ray while rightward are not (Linsky et al., 1979) although a few possible exceptions have been observed (e.g., γ Dra, a K5III at $L_X \simeq 2.8 \times 10^{27}$ erg/s, Reimers et al., 1996). Chromospherically active stars are also found in binaries where one or both stars are magnetically-active: the detached RS CVn stars (F-K), Algols (semi-detached, B5-F2V + G-K IV/III), BY Dra (dG/dK/dM stars) and the contact WUMa stars (F-KV) (Walter et al., 1980; Barden, 1985; Strassmeier et al., 1988; Sahade et al., 1993). All systems are capable of producing $L_X \sim 10^{29} - 10^{31}$ erg/s and consist of one or more coronally active stars. They are prominent UV and H α emitters and show

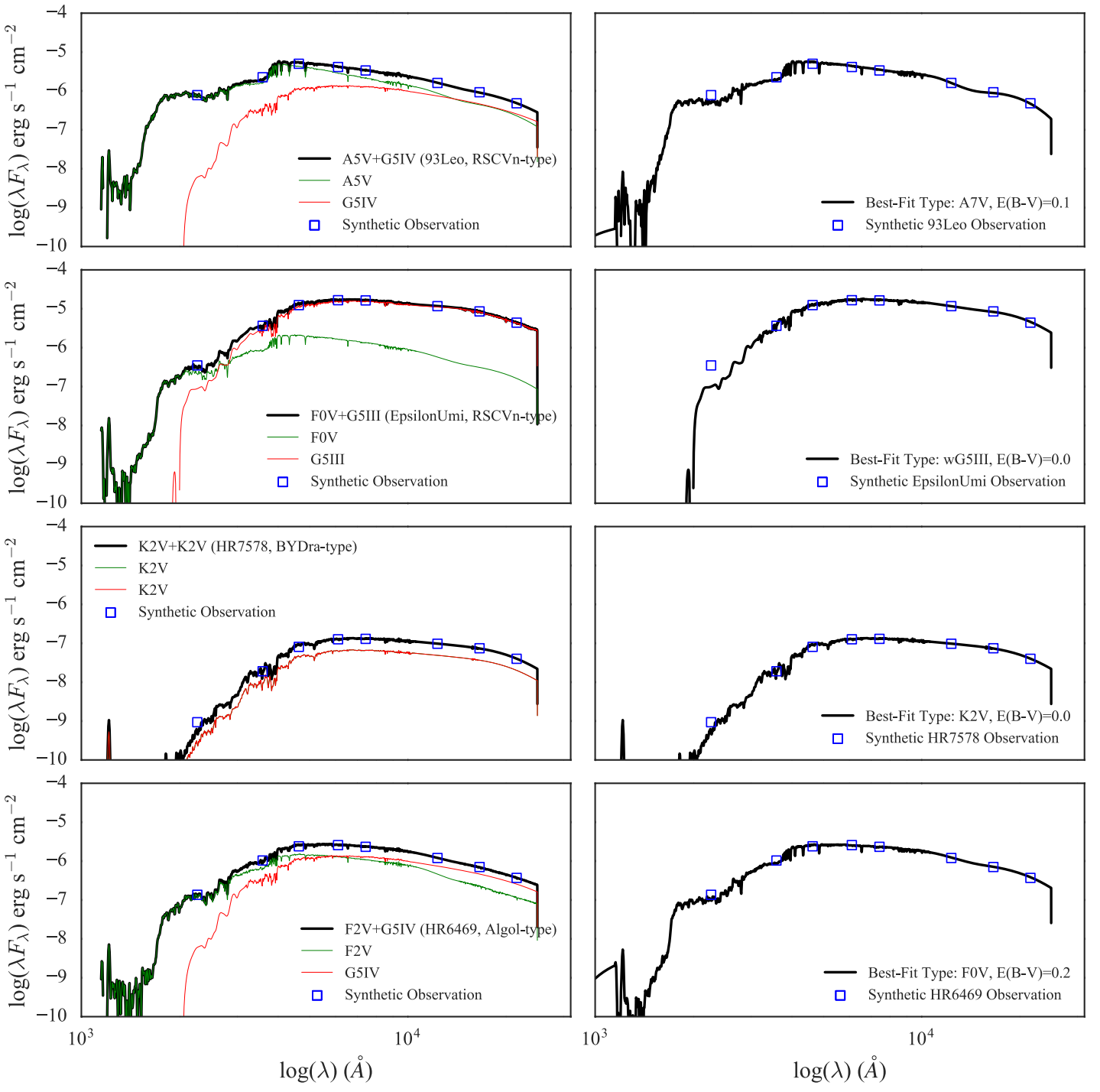


Figure 2.9: Each plot in the left column represents a synthetic RS CVn, Algol or BY Dra (see legends). The blue squares are simulated photometry in *GALEX*, VPHAS+ optical and 2MASS IR. The right plots are the corresponding spectral fits to said data, and reveal that the summed flux can manifest as a single star or show a UV-excess (e.g., Epsilon Umi) in this analysis. In combination with expected variability allows us to conclude that active, non-compact binaries may not be conclusively identified in this study.

an enhanced presence of starspots that can be periodically observed (Eaton and Hall, 1979; Udalski et al., 2012). We claim that our SED-modeling may not be sensitive enough to directly identify the presence of a cool secondary in an RS CVn-like system: they are inherently variable (on the scale of ~ 0.5 mags) in the optical meaning the optical and UV may be poorly fit with non-simultaneous observations. And, apart from the expected UV excess the two stars may sum to a final curve that still *looks* like one star; the least luminous of the pair may be washed out in the final spectrum, especially since the Pickles templates only extend up to about 2MASS K_s (~ 21600 Å) and cool M-dwarf companions contribute the majority of their flux redward of K_s . To test this sensitivity we simulated a few known active binary systems in `pysynphot` and produce synthetic observations in *GALEX*, VPHAS u', g', r' and i' as well as 2MASS J, H and K_s . Re-fitting the synthetic photometric data confirms that the least luminous component is completely or partially hidden, and that many will only be indistinguishable from a single coronally active star. In the case of Epsilon Umi, the G5III dominates the IR and most of the optical over the F5V companion due to its size. The resulting synthetic photometry returns a G5III with a visually-obvious UV excess. This indicates that giants with UV excess could theoretically be RS CVn-like systems harbouring a smaller, hotter *dwarf* companion. The results of this procedure are shown in Figure 2.9.

If a confident spectral type (or even a range) is determined for any source, we can compare the theoretical X-ray emission to that observed with *Chandra*. Agüeros et al. (2009) computed mean $\log(F_X/F_V)$ values (with 2σ upper/lower limits) for F, G, K and M main sequence stars (sample sizes 142, 99, 89 and 40 respectively) using RASS/SDSS data with known spectral types from SIMBAD as shown in Table 2.3 where $\log(F_X/F_V) = \log(F_X) + 0.4V + 5.37$ as defined in Maccacaro et al. (1988), where V is the V-band optical magnitude. Exactly which magnitude system being used is unclear as Agüeros et al. (2009) use V from the SIMBAD database, but this differs depending on the instru-

Table 2.3: Expected X-ray to optical fluxes from Agüeros et al. (2009) where $\log(F_X/F_V) = \log(F_X) + 0.4V + 5.37$.

Type	Mean	2σ (upper)	2σ (lower)
F	-3.72	-4.86	-2.58
G	-3.31	-4.45	-2.17
K	-3.13	-4.70	-1.57
M	-1.57	-3.07	-0.07

ment/survey SIMBAD quotes. We adopt V band magnitudes in the AB system like all other magnitudes in this work and compute errors on this ratio using the V-band error and the error on X-ray counts as given by $\sigma_N = 1 + \sqrt{N + 0.75}$ (Gehrels, 1986). To convert *Chandra* X-ray counts in the 0.5-8.0 keV band to flux values we assume most emission to be of hot, chromospheric plasma. We use the WebPIMMS calculator⁷ for *Chandra* Cycle 9 ACIS-I at 1 count / 2ks, and a Plasma/APEC model assuming Galactic $N_H = 10^{21} \text{ cm}^{-2}$, solar abundance metallicity, an unabsorbed spectrum at $\log(T) = 7.10$ output into the comparable *ROSAT* filter in Agüeros et al. (2009) of 0.1-2.4 keV yielding $1.06 \times 10^{-14} \text{ erg/cm}^2/\text{s}/\text{photon}$. Jonker et al. (2011) used a value of $7.76 \times 10^{-15} \text{ ergs/cm}^2/\text{s}/\text{photon}$ as a rough estimate of *Chandra* counts-to-flux conversion, but assumed a power law emission model and $N_H = 10^{22} \text{ cm}^{-2}$ to represent CO emission across a farther extent of the Galaxy.

2.6 Results & Discussion

The effectiveness of using the *GALEX* position to reduce both optical and IR ambiguity is shown in Figure 2.10 where this Figure includes all 269 *GALEX/Chandra* matches. Prior to this analysis, only 40 of 269 *GALEX/Chandra* sources had a single 2MASS counterpart in the X-ray circle while none had a single VVV counterpart (VVV is deeper). After matching to the *GALEX* position, 210 of 269 sources have a single 2MASS counterpart and 80 in VVV, effectively reduc-

⁷<https://heasarc.gsfc.nasa.gov/cgi-bin/Tools/w3pimms/w3pimms.pl>

Table 2.4: The number of *GALEX/Chandra* systems with a counterpart in a given survey. The decrease down the table is a combination of decreasing depth, differences in coverage and larger IR surface densities than optical.

Survey	Counterparts (/269)
2MASS/VVV	253
VPHAS+	224
MOSAIC-II	167
APASS	135
WISE	101
GLIMPSE-3D	71
Tycho-2	48

ing the ambiguity of these data. We note that the Greiss et al. (2013) dataset lacked a number of 2MASS sources, possibly due to the catalogue creation before updated 2MASS results. For the shown 2MASS distribution we show the results matched to a query of the most recent 2MASS data in TOPCAT.

The number of matches in each survey is shown in Table 2.4 and reflects the decreasing depth towards the bottom of the table. Of 269 *GALEX/Chandra* matches, 223 have offsets $< 3.0''$ where the number of expected chance *GALEX/Chandra* interlopers $N_{ch} = 15 - 20$ (see Table 2.2). There are 47 systems with $\Delta r > 3.0''$ but $N_{ch} = 50 - 53$ here and so it is likely that most or all are unassociated with the X-ray emission altogether. For this reason we do not attempt source interpretation and refer readers to Appendix A for all associated photometric data, including this set.

Of the ‘good’ 223 systems, there are 148 well-fit *including* UV (single stellar systems, Section 2.6.1), 14 well-fit *excluding* UV and 61 unfit altogether even after inflating errors lower than 0.1 mag (Section 2.4).

The degeneracy between stellar temperature and normalization shifts the fitted spectral type towards hotter stars as $E(B-V)$ is raised for each fit. This can be visualized in colour-colour diagrams where a hypothetical reddening of a point shifts it along the vector with the slope $E(A-B)/E(C-D)$ (where the colours $A - B$ and $C - D$ are the x and y axes, respectively). These are shown

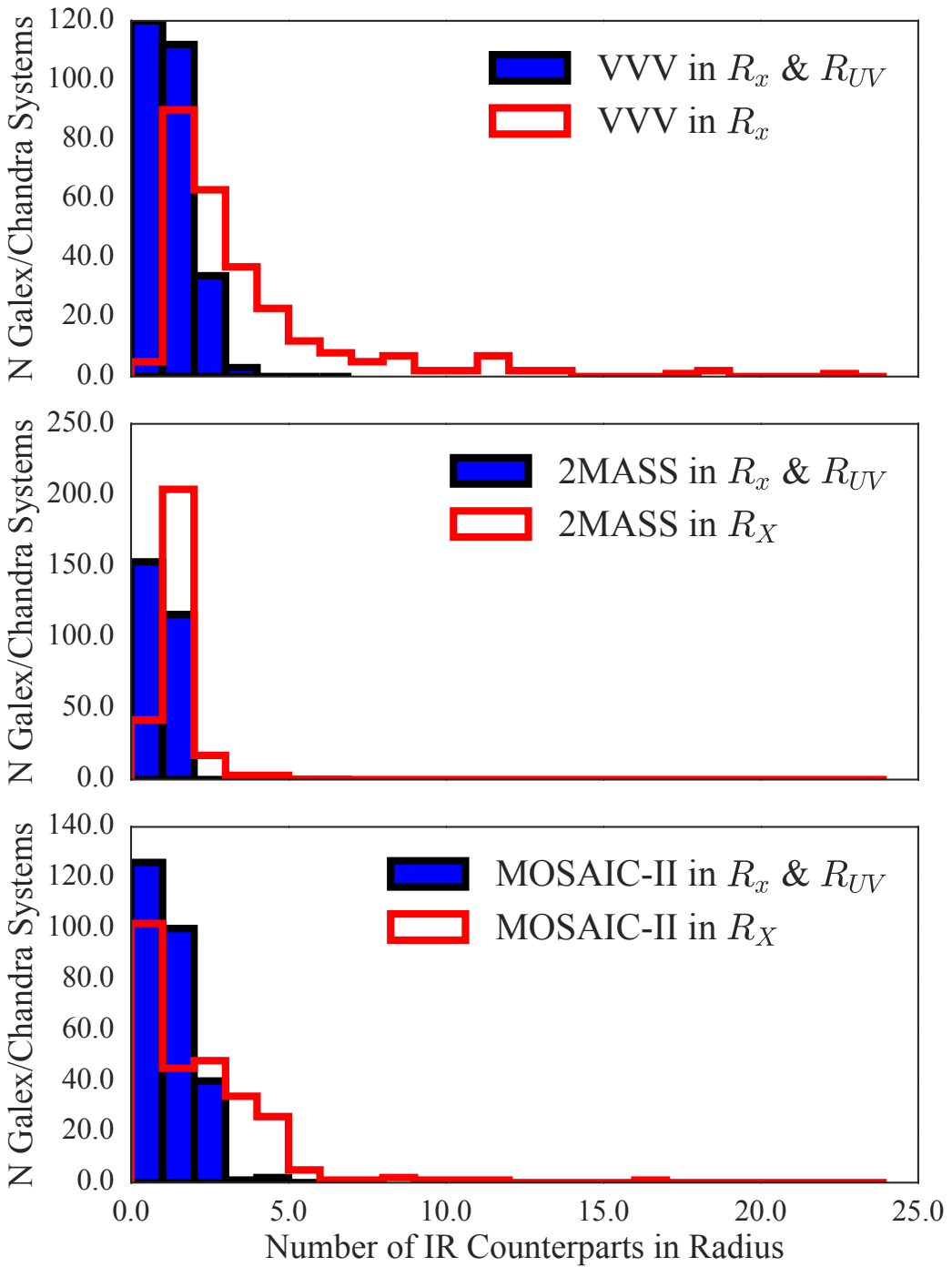


Figure 2.10: The distribution of the *GALEX/Chandra* systems with N counterparts in VVV, 2MASS and MOSAIC-II in the X-ray circle R_X and the corresponding R_{UV} . The shift of the distributions leftward indicates the *GALEX*-matching-algorithm effectively reduces the ambiguity of optical and IR counterparts matching. For those systems which still have > 1 to choose from, we opt for the source with the lowest false alarm probability (FAP) as calculated in the 2MASS/VVV and MOSAIC-II datasets (Greiss et al., 2013 and Wevers et al., 2016a respectively).

in Figures 2.12, 2.11 and 2.13 for those sources with B and V observations and include all systems in the *GALEX/Chandra* dataset with observations in those particular combination of bands (less than the whole set). Theoretical colours for A-M types are taken from the Pickles Library with synthetic observations using `pysynphot` and plotted overtop. We computed reddening vectors using relations between absolute extinction $A_{NUV} = 1.51A_V$ (Allen's Astrophysical Quantities, Cox, 2000) yielding $E(NUV - B) = 0.589 \times E(B - V)$ and $E(J - H) = 0.334 \times E(B - V)$ assuming the Cardelli extinction curve with $R_V = 3.1$. For clarity, only visual outliers have errorbars/annotation and all magnitudes are in the AB system.

The $(NUV - B)$ vs. $(B - V)$ diagram reveals a population of F-K stars with various reddening values, indicated by the population below the MS track. Since this plot is only a subset of available sources (namely those with B and V data) the lack of observed M-types is due to their optical faintness in Tycho-2 and APASS: the hottest/brightest M-dwarf M0V has an upper limit of $d \sim 400\text{pc}$ for the APASS limiting magnitude of $m \simeq 17$. The $(J - H)$ vs. $(H - K)$ separates the theoretical K/M luminosity classes, but the direction of change is parallel to the reddening vector. Both $(J - H)$ plots show some systems with IR excesses indicating the presence of a circumstellar material, a positional blend or a cooler binary companion (e.g., an RS CVn). Outliers to the right of the diagram are good candidates for active binaries, where the K_s -band excess may indicate the cool companion.

2.6.1 Chromospherically Active Population

The *GALEX/Chandra* dataset is dominated by a local, chromospherically active population supporting the findings of other Galactic X-ray surveys with Einstein, *Chandra*, ROSAT and XMM (Koenig et al., 2008; Motch et al., 2010; Vaiana et al., 1981; Sazonov et al., 2006; Schmitt, 1997). This also supports the coronal population in SDSS/*GALEX* matching (Smith et al., 2014) that

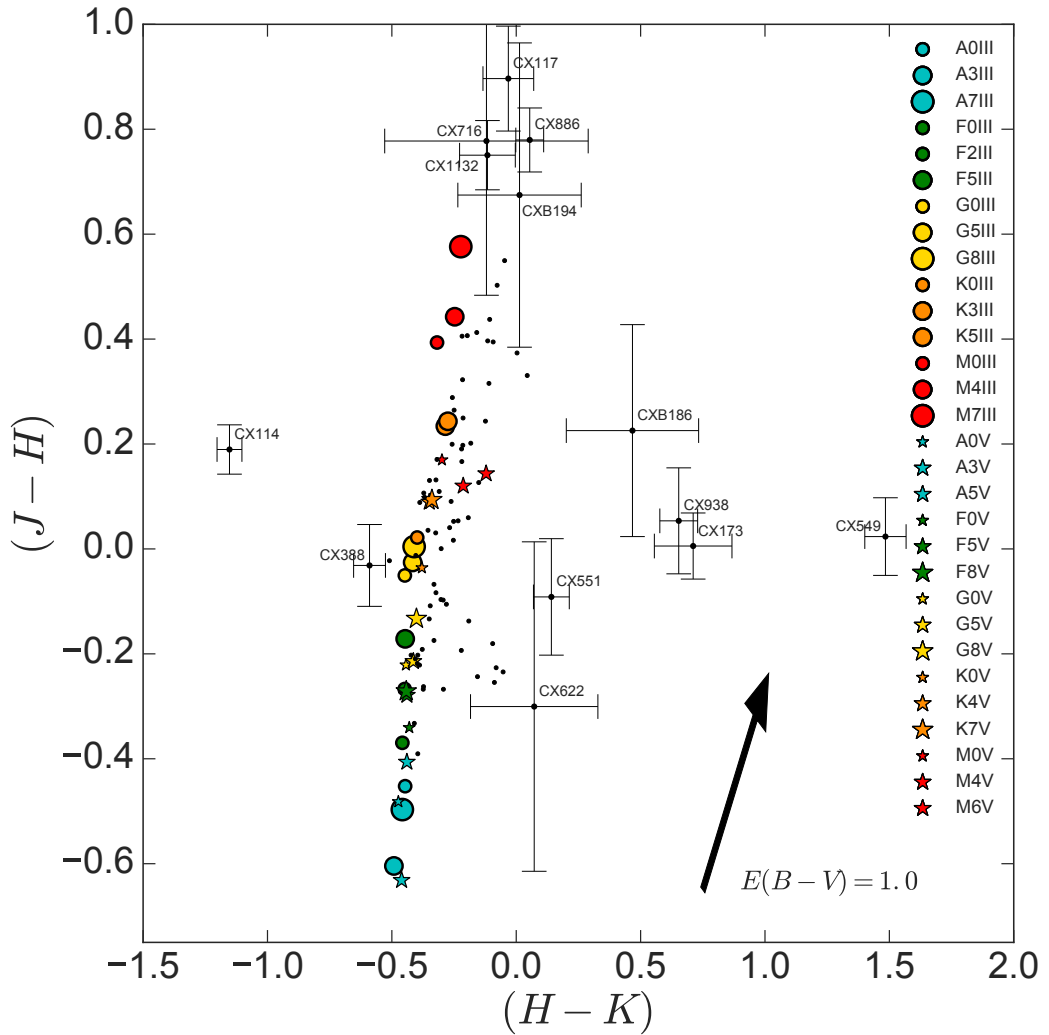


Figure 2.11: $(J-H)$ vs. $(H-K)$ colour-colour diagram for 106 sources in the GBS with either 2MASS or VVV J, H, K_s data. Main sequence and giant stars are plotted from sample spectra in the Pickles Library (Pickles, 1998).

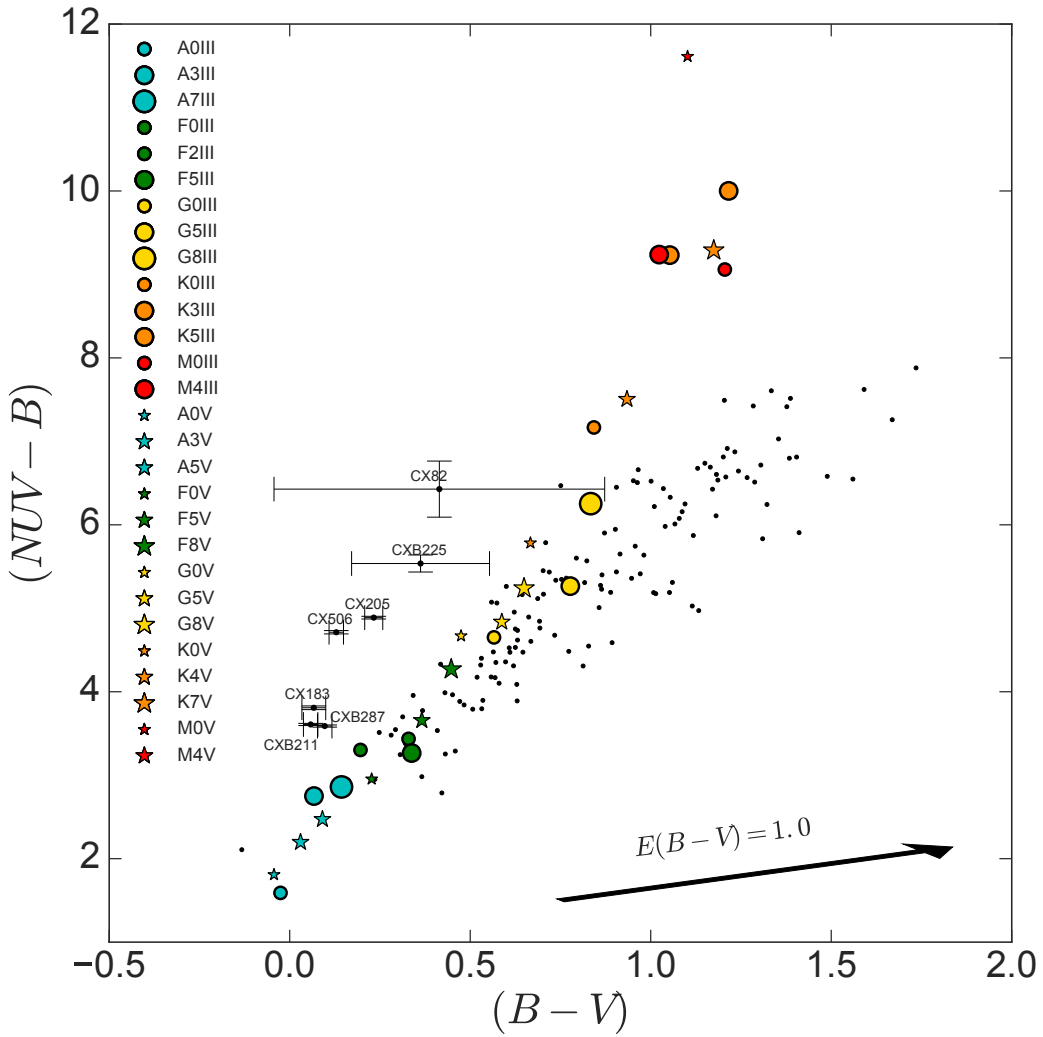


Figure 2.12: $(NUV-B)$ vs. $(B-V)$ colour-colour diagram for 142 sources in the GBS with corresponding counterparts in B and V. Main sequence and giant stars are plotted from sample spectrum in the Pickles Library (Pickles, 1998). B and V data are from either APASS or Tycho-2.

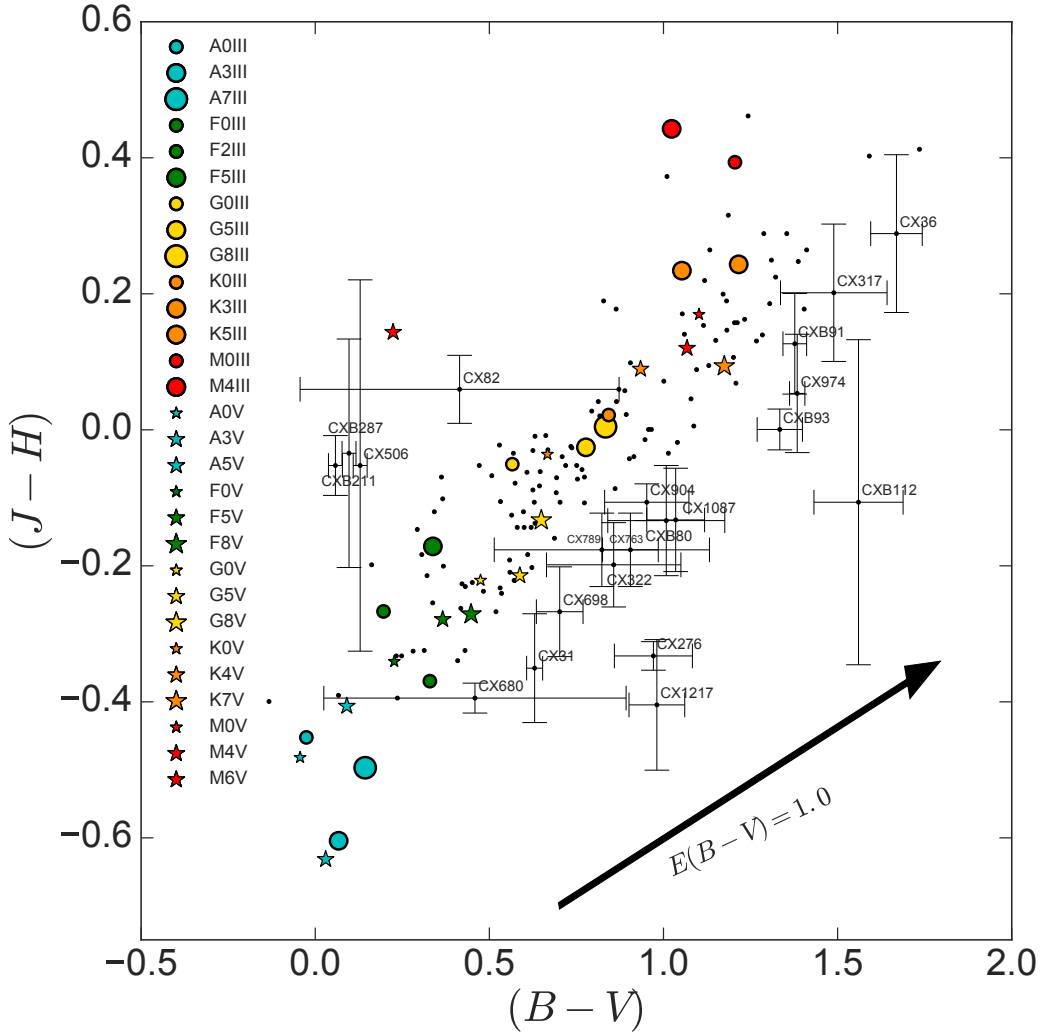


Figure 2.13: $(J-H)$ vs. $(B-V)$ colour-colour diagram for 141 sources in the GBS with corresponding counterparts in J, H, B and V. Main sequence and giant stars are plotted from sample spectrum in the Pickles Library (Pickles, 1998). B and V data are from either APASS or Tycho-2 and J/H from 2MASS/VVV.

are blue, show large UV-excesses and metallic line weakening with most F-K type.

There are 148 systems that are successfully fit by a Pickles template at some 0.1 interval between $0 < E(B - V) < 1$. In this way, we claim each system is plausibly single-stellar and that the X-ray and UV emission is coronal. In some cases, a system is well-fit by a different spectrum at a different $E(B - V)$ value - the takeaway is that each is *plausibly* a single star. Any of these systems could harbour a cooler companion (RS CVn or Algol-type) whose low luminosity effectively erases it from the SED (see Section 2.5) and so many of these stars also could be active binaries.

The distribution of best-fit spectral types peaks in the G class, followed by F, A, B, K and M (Figure 2.14). We combine this distribution with the extinction value at that particular best-fit model, showing B stars only at high $E(B - V)$ and M stars only at very low $E(B - V)$. This reflects that we see hotter and brighter stars at farther distances and are still observing near the Galactic Plane reducing the number of optically-dim K/M stars. Moreover, particularly active stars probably won't fit the UV regime of the Pickles spectra anyhow - this is corroborated by the observation of multiple active M-dwarfs in the UV-excess set (Section 2.6.2).

Coronal activity is driven by rotation, and magnetic braking reduces this rotation over time. Indeed, it has been known that activity levels anti-correlate with age (Hall, 2008; Güdel, 2004) suggesting this sampled population is young or is UV-enhanced by the presence of a cool secondary. Pace and Pasquini (2004) found that the levels of coronal activity decrease rapidly through 0.5-1.6 Gyr and then more or less plateau, removing the ability to use activity as an age indicator for stars older than 1.6 Gyr. Other recent work suggests it is no longer clear magnetic activity in the form of optical/X-ray flares or chromospheric UV is a reliable age indicator or vice-versa; active coronal UV fluxes are found in both very young stars and those as old as the

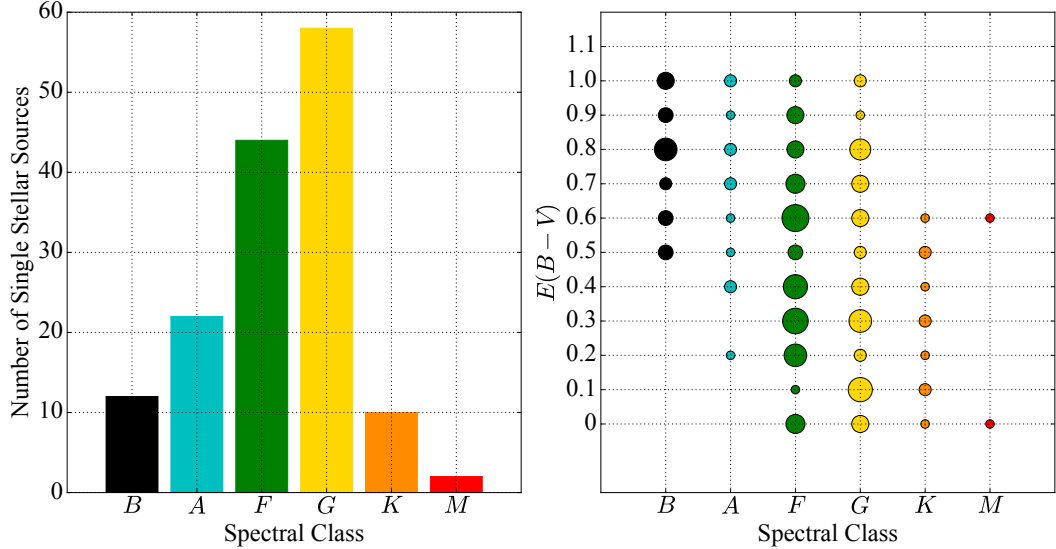


Figure 2.14: For the single-stellar population, (left) the distribution of spectral classes from the best-fit spectral modeling. (right) The distribution and frequency of $E(B - V)$ for each spectral class. The size of the circle represents the number of sources occupying that class and $E(B - V)$.

Hyades (Soderblom, 2010). There are 14 sources that are well-fit *without* the inclusion of the *GALEX* NUV datapoint. Each SED is analyzed manually: 5 show a pure NUV excess, 3 lack optical data between NUV and J,H,K, 3 are poorly fit in the IR, 1 is a known CV/qLMXB. The UV excesses in the first 5 are measured against the derived upper limits on M-dwarf activity (Equation 2.7) by converting observed X-ray/UV fluxes to surface fluxes using the stellar radius R of the best-fit spectral type and place the source at $d = 100$ pc. Figure 2.15 shows the result - note that the original data had an rms spread in y-space of ~ 0.5 units. CXB130 and CX662 show UV excesses comfortably attributed to coronal activity, and spectral fitting shows they are likely both M-dwarfs anyhow. If a single source, CX10 is best-fit as a highly-active FV star which supports its initial classification. We retrieve best-fit types of F5-F8V for $E(B - V) = 0.4 - 0.7$, and the surface UV excess is relatively large (Figure 2.15). Hynes et al. (2012) re-analyzed CX10 with RAVE Data and suggest a mildly-evolved G7V at $E(B - V) = 0.37 \pm 0.08$. Using the observed V magni-

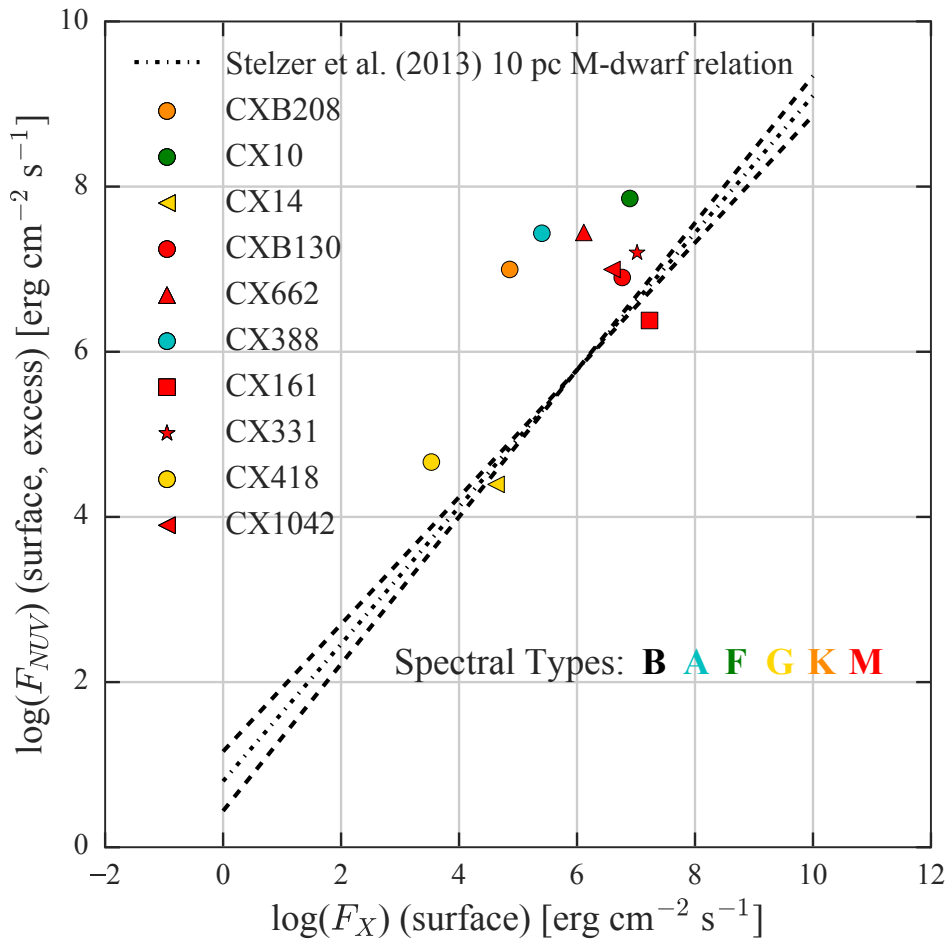


Figure 2.15: Plotted are 5 systems against the power-law relation for M-dwarf activity to assess plausibility of being a compact system instead. The rms scatter of the original data (Stelzer et al., 2014) in y-space from the best-fit line is ~ 0.5 units.

tude and X-ray flux, $\log(fx/f_{bol} \simeq -3.47)$ which lies in the ranges of both F and G stars (Table 2.3). Our modeling shows CX10 is best-fit as a G7/G8V only when $E(B - V) = 0.3$ ($\chi^2_\nu = 1.367$) but this is not the overall best-fit; its surface UV excess is much larger assuming a G-type. Nonetheless, CX10 is plausibly a highly-active (and likely rapidly rotating) F/G star.

CX716 and CX1132 do not have any optical counterparts identified by our process, and CX551 only has saturated MOSAIC-II data. CX716 has only one listed counterpart in Greiss et al. (2013), a VVV source $1.49''$ away with $J = 17.647$ with errors of 0.1-0.2. The IR colours suggest an M7III-M8III for all $E(B - V) < 1.0$; as mentioned in Section 2.3.2, G13’s catalogue is incomplete misses some 2MASS observations, most of which were corrected for. Checking both SDSS and 2MASS images there is a bright optical counterpart $\sim 2 - 3''$ away with a brighter corresponding 2MASS observation of $J = 13.591$. In the $(J - H, H - K)$ plane this brighter source could be a reddened B star and astrometrically it appears it is probably the source of UV emission, while the X-ray emitter could be a background source ($R_X \sim 1.18''$).

CX1132 may be a WD+MIII symbiotic system due to its optical faintness and IR colours (see Figure 2.11) and we suggest spectroscopic follow-up. CX551 does not appear in any other optical catalogue we surveyed, leaving the SED fairly unconstrained. However, it appears with an obvious optical counterpart in SDSS images indicating that a counterpart exists but neither APASS or VPHAS covered this region. It is an outlier in the $(J - H, H - K)$ diagram suggesting an IR blend or a heavily reddened A star; formally, the best-fit with all included points is an A7V at $E(B - V) \simeq 0.9$ ($\chi^2_\nu = 2.853$) which supports its IR colours. Lastly, the *GALEX* flux exceeds the comparable UVM2 filter by ~ 1.6 mags indicating inherent UV variability between observation times uncharacteristic of A stars with little to no convective region and thus limited coronal activity. We suggest CX551 as a target for spectroscopic follow-up.

In CX174, CX253 and CX839 it is the IR that becomes poorly fit when

NUV is excluded. ‘Loose’ modeling of J, H, K_s bands occurs with the $\sim 0.1\text{mag}$ shifted-errors at the expense of more numerous optical observations, primarily at higher $E(B - V)$ forcing the curve down into the optical region - the NUV point heavily constrains the shape of the optical and its inclusion prevents this behaviour. CX253 is particularly crowded and has two nearby bright stars straddling the X-ray circle; the IR is either a blend or does not match the optical. CX174 and CX839 are active binaries: they have similar H and K behaviour which, after checking the images, appears to be real and indicative of a cooler companion.

2.6.2 Poorly Fit, UV-Excess Systems

The 61 poorly-fit sources theoretically are a mix of compact binaries (identified by UV-excess), cool binaries (identified by IR-excess), systems with too few optical/IR data or a particularly dense error circle where the algorithm does not converge. We present 30 systems that cannot be fit primarily from large UV fluxes or visual binarity, and suggest this set as targets for spectroscopic follow-up. Figure 2.16 shows each SED with best-fit blackbody curves overtop (for $E(B - V) < 1$) to guide the eye and Table 2.5 summarizes their system properties. 7 systems have been previously identified as compact binaries either by the GBS collaboration or from literature, and their SEDs are shown separately (Figure 2.16). All SEDs have mutually consistent survey colour-coding and saturated points are plotted as triangles in their appropriate colours. For individual spectral fitting, filter-integrated fluxes (the flux-per-band one would observe given some fitted model parameters) are plotted as blue squares.

All NUV counterparts to these outliers have preferentially dim apparent magnitudes ($< 20\text{mags}; 2.5$); both known and currently unknown compact systems are on average more distant than the dominant population of active stars and thus quite UV extinct. SDSS (r’ - i’) is taken from MOSAIC-II data when given and from VPHAS when saturated or not available. Where

large optical variability is present in the SED, colour has little meaning as it differs between surveys - these are left out. (J - H) and (H - K) colours are in native 2MASS magnitudes. These systems are preferentially covered in r' and i' instead of B and V because VPHAS covered a larger region of the sky than APASS and Tycho-2 covers only a handful of bright sources.

2.6.3 Individual Sources

The main tools for interpretation of the poorly-fit systems are the results from spectral fitting (particularly in the IR), previous observations of variability and a proper combination of distance and extinction A_λ . Any distances derived from $E(B - V)$ and vice versa use the 3D Milky Way Dust Map from Green et al. (2015). Absolute magnitudes on the main sequence are quoted from Eric Mamajek's online table⁸ and giant colours from Allen's Astrophysical Quantities (Cox, 2000) and Li et al. (2016) for recent IR observations of M-giants in the case of possible symbiotics.

CX21: Quiescent CV

CX21 was identified as a quiescent CV by Britt et al. (2014) from its strong optical flickering (1.0 mag on hour timescales) and its hardness ratios in *Chandra* (-0.38, [2.5-8]-[0.3-2.5]/[0.3-8.0] keV) and *ROSAT* (+0.28, [0.9-2.0]-[0.5-0.9]/[0.5-2.0] keV) both consistent with thermal bremsstrahlung emission from hot plasma. They interpret the strong optical flickering as large contributions of an accretion flow or disk to the optical region, possibly indicating an accreting system. In the SED we observe both a large NUV excess and large-scale optical and UV variability; $\Delta\lambda_{eff}$ between *GALEX* and UVOT filters is only 300Å and vary in magnitude by nearly 3.0 magnitudes while MOSAIC-II and VPHAS data report differences of $\simeq 0.6$ mag in the same filters r' and i'. These

⁸http://www.pas.rochester.edu/~emamajek/EEM_dwarf_UBVIJHK_colours_Teff.txt

GBS ID	N_X	R_X	RA_{glx}	DEC_{glx}	Δr	m_{NUV}	$r' - i'$	J - H	H - K	Comments
CX21	60	2.007	265.390778	-28.676401	1.37	20.7 ± 0.1	-	0.43	0.4	CV ²
CX33	42	1.251	267.148504	-29.958356	2.037	12.257 ± 0.005	-	0.25	0.38	B0 Ve ⁸
CX93	20	1.329	266.186765	-26.057844	2.177	23.3 ± 0.5	1.15	0.79	-0.26	CV ³
CX117	17	2.035	265.173378	-27.634151	1.574	21.9 ± 0.5	2.25	1.38	0.43	Symbiotic ¹
CX118	17	2.211	264.709079	-28.802424	1.004	22.9 ± 0.4	0.96	0.86	0.02	CV ⁴
CX137	15	4.217	268.971861	-28.276128	0.905	20.7 ± 0.2	0.49	0.71	-0.47	CV/qLMXB ⁵
CX161	13	1.228	264.967673	-28.573608	0.344	23.5 ± 0.4	1.61	0.94	0.5	Active Star ¹
CX331	8	1.719	264.097632	-29.375786	1.856	21.4 ± 0.4	1.4	0.81	0.11	Active Star ¹
CX361	7	5.885	267.781933	-29.677008	0.262	18.33 ± 0.03	-	0.82	-0.22	AM CVn ⁶
CX388	7	1.105	264.247887	-29.101394	2.921	16.51 ± 0.03	-	0.45	-0.12	?
CX398	7	1.519	263.438657	-29.53755	2.105	21.4 ± 0.4	1.57	-	-0.1	Symbiotic ¹
CX417	6	1.579	268.616152	-28.130233	1.993	15.256 ± 0.006	0.18	0.67	0.25	CV ¹
CX418	6	2.173	268.576593	-28.678196	1.231	19.34 ± 0.07	0.69	0.78	0.04	CV ¹
CX426	6	1.259	268.150211	-29.327683	0.17	20.4 ± 0.2	0.39	0.94	-0.22	CV ²
CX495	6	2.664	263.698702	-29.587028	1.784	22.6 ± 0.7	1.56	0.84	-0.08	M-dwarf/CV ¹
CX497	6	1.844	263.592864	-30.084866	2.752	22.0 ± 0.5	0.68	0.74	0.22	Active Star ¹
CX551	5	1.452	266.826059	-30.510148	1.622	22.7 ± 0.4	-	0.39	0.61	?
CX645	5	1.64	266.639173	-26.387221	0.457	22.6 ± 0.3	-	0.92	0.17	CV/qLMXB ²
CX662	4	1.675	269.175691	-27.764842	0.951	19.3 ± 0.1	0.78	0.7	0.15	Active Star ¹
CX673	4	3.076	268.868341	-28.393448	0.435	22.0 ± 0.3	1.5	-	-0.11	?
CX886	3	6.569	266.283183	-27.193868	1.606	22.0 ± 0.4	2.48	0.99	0.2	?
CX1029	3	3.962	266.341768	-26.015778	2.049	22.6 ± 0.5	1.44	0.82	-0.09	?
CX1042	3	4.364	266.15106	-26.294039	2.377	21.9 ± 0.3	1.4	0.75	-0.11	Active Star ¹
CX1132	3	1.31	264.770372	-29.134083	2.67	23.3 ± 0.4	-	0.98	-0.09	Symbiotic ¹
CX1229	3	1.943	267.986795	-28.696417	1.755	21.9 ± 0.3	-	0.88	0.37	?
CXB10	53	1.052	269.635005	-27.878853	0.173	20.4 ± 0.2	-	1.27	0.56	CV ⁷
CXB186	5	5.143	268.541988	-29.430703	1.776	21.1 ± 0.3	1.03	0.71	0.93	?
CXB202	5	4.148	263.306701	-30.412676	2.232	21.8 ± 0.4	1.05	0.82	-0.23	?
CXB208	5	5.14	268.422191	-29.922248	0.713	16.94 ± 0.01	-	0.70	0.21	Symbiotic CV ¹
CXB223	4	2.559	269.134064	-28.714223	2.966	21.6 ± 0.4	1.32	0.98	0.39	?

Table 2.5: UV excess sources from *GALEX/Chandra* matching in the GBS. Columns (L to R): colloquial GBS name, number of observed *Chandra* X-ray counts, *Chandra* X-ray error as derived in Section 2.2.3, RA and DEC of the *GALEX* NUV counterpart, offset between *GALEX/Chandra* positions, *GALEX* magnitude in AB system, SDSS r' - i' colour, 2MASS J,H,K colours. Superscript references: (1) this paper, (2) Britt et al. (2014), (3) Ratti et al. (2013), (4) Wevers et al. (2017), (5) Torres et al. (2014) , (6) Wevers et al. (2016b), (7) Mróz et al. (2015), (8) Hynes et al. (2012).

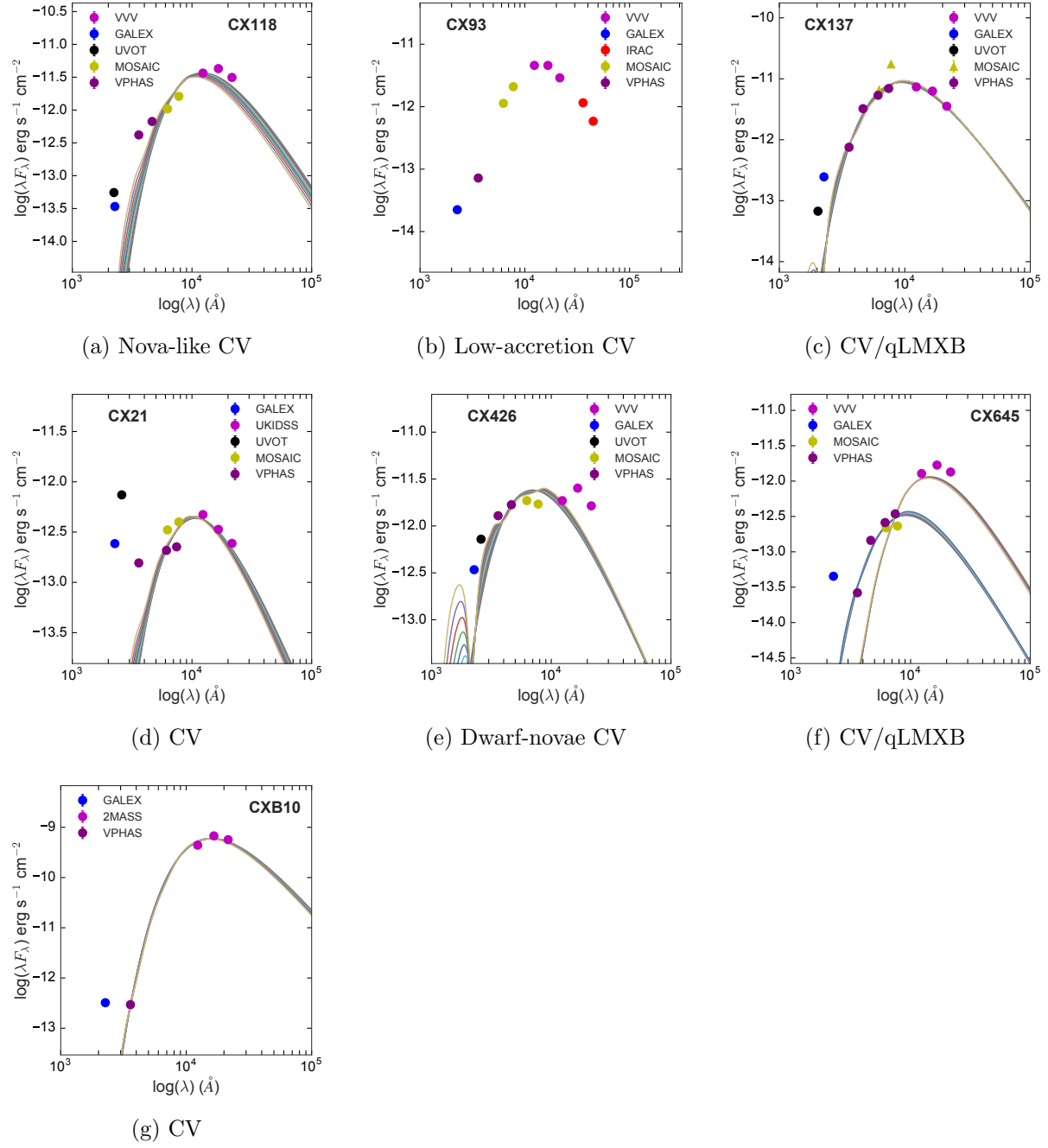
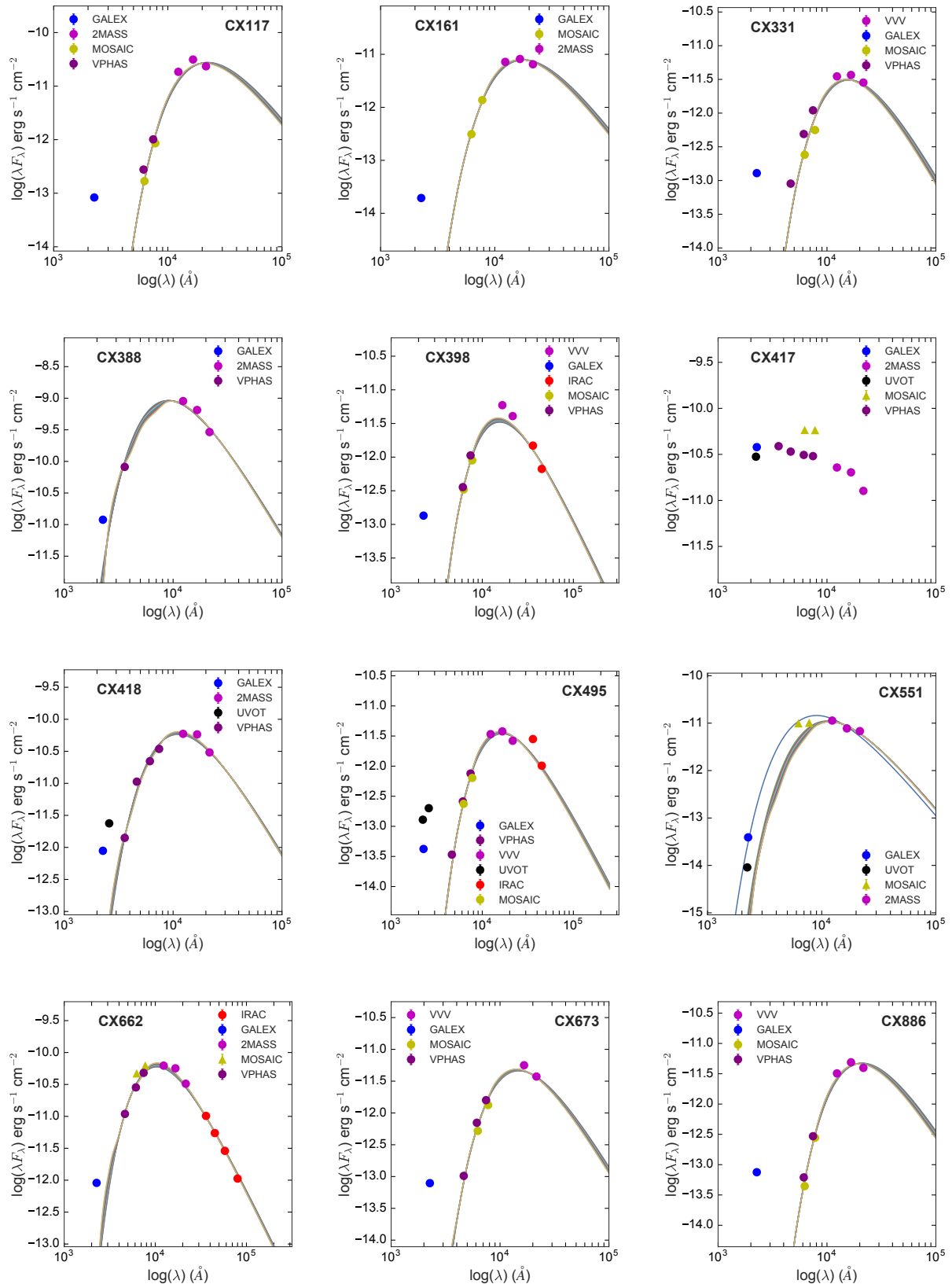


Figure 2.16: Known compact binaries in the UV-excess dataset. Best-fit blackbody curves for $0.0 < E(B - V) < 1.0$ in steps of 0.1 are overplotted to show the general broadness of the SEDs with a single-stellar profile. Saturated points are shown as triangles at their survey quoted magnitudes.



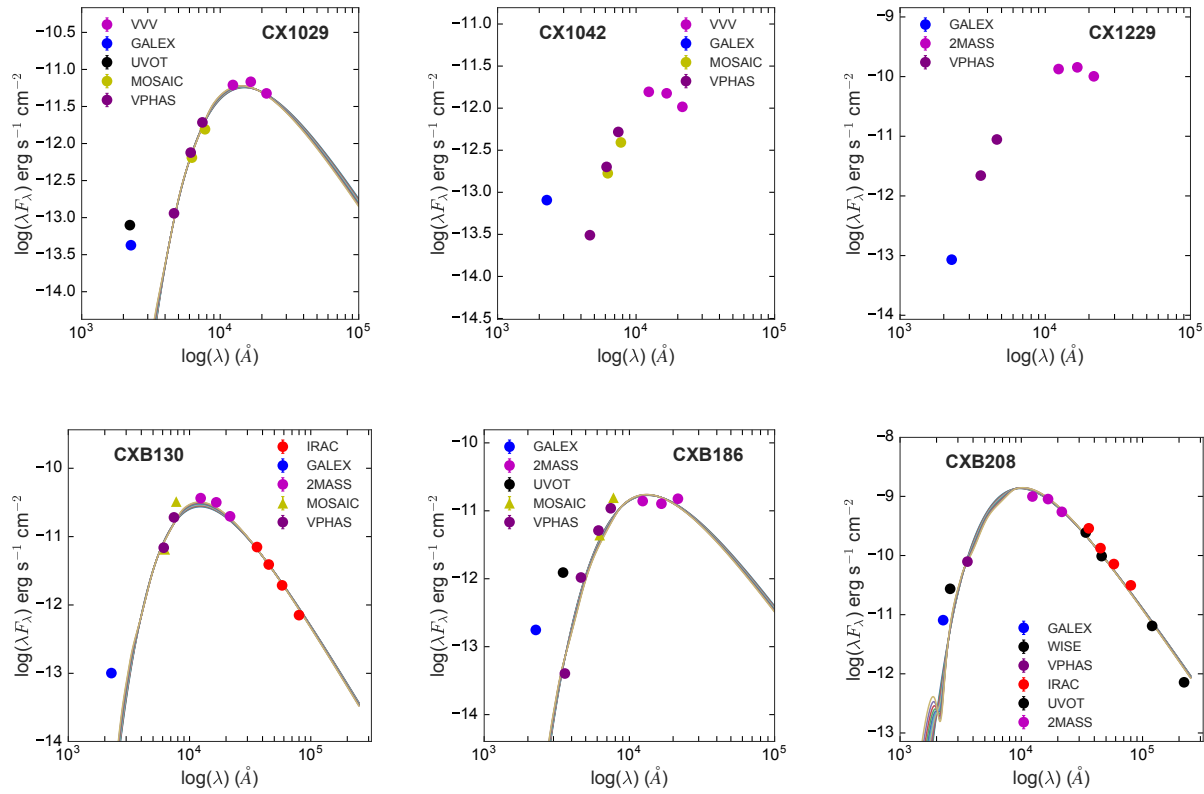


Figure 2.16: New UV-excess sources from Table 2.5.

brightness differences support the interpretation of CX21 as an accreting CV.

CX33: Bulge Be Star

CX33 corresponds to HD 316341, a known Be star (noted in Hynes et al., 2012). They infer that $E(B - V) = 0.8$ and $d = 1.3$ kpc and $L_X = 8 \times 10^{31}$ erg/s, but updated dust maps indicates this is a fairly low-extinction line of sight: at this extinction, $d \sim 8.5 - 8.6$ kpc. It is an ASAS variable (NSV 23882, All Sky Automated Survey⁹) showing substantial variability including outbursts of magnitude ~ 0.5 with a recurrence time of about 200 days. They also report an infrared excess in 2MASS which we confirm via the SED (specifically, the K band; see SED). CX33 was poorly fit specifically due to B and g detections in the APASS survey which sharply contradict the B and V observations from Tycho-2 despite being only milliarcseconds apart. The noted ASAS variability can account for this change as it is roughly 0.5 magnitudes, and we have no other reason to believe the SED shows binarity. Re-modeling the system *without* APASS yields multiple successful fits, all B-type; formally the best fit is a B2IV at $E(B - V) = 0.9$ although another successful fit exists for a B3III at $E(B - V) = 0.8$. At ~ 8.5 kpc it would lie in the Bulge with $L_X = 3.9 \times 10^{33}$ erg/s, indicating CX33 could be either a closer, normal Be star or possibly a Bulge binary system.

CX93: Low Accretion-State CV

Ratti et al. (2013) identified CX93 as a long period CV in a low accretion state with a spectrum dominated by a K5V (+/- one spectral type) companion for $E(B - V) \simeq 0.65 \pm 0.2$ (Ratti et al., 2013). We find a statistically good fit ($\chi^2_\nu = 0.9$) for a small, hot blackbody of 33000K + a K5V at $E(B - V) = 0.975 \pm 0.083$ despite a small underestimation of the NUV flux

⁹www.astrouw.edu.pl/asas/

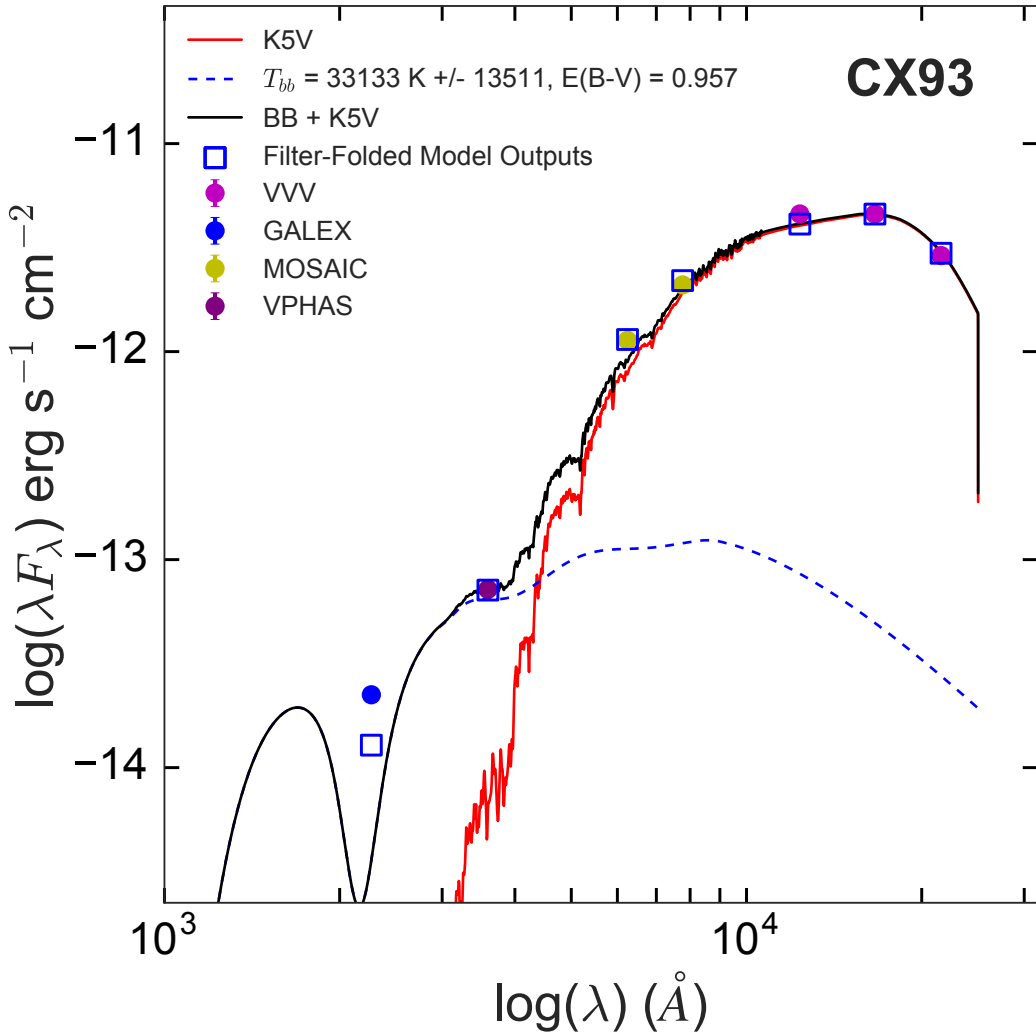


Figure 2.17: CX93 modelled with MCMC as a K5V + hot blackbody component.

(Figure 2.17). The hot component is fairly unconstrained in temperature due to the mutual degeneracy of normalization, E(B-V) and temperature but is necessary to explain the extensive *GALEX* and VPHAS u' fluxes.

CX117: WD+MIII Symbiotic System

CX117 is observed with 17 *Chandra* counts for a total X-ray flux of 1.802×10^{-13} erg/cm²/s. Britt et al. (2014) classify it as non-variable in SDSS r' using the MOSAIC-II imager. Its *GALEX* NUV counterpart is 1.57" away and is also

found in VPHAS, MOSAIC and 2MASS. Its IR colours strongly suggest a reddened, late MIII or a heavily reddened M-dwarf at $E(B - V) \sim 1.5$ (Figure 2.11) corresponding to $d \sim 3$ kpc. We do not expect to see M-dwarfs past ~ 50 pc and thus such high reddenings rule out a dwarf. Assuming an M0III with $E(B - V) = 1.0$, the Milky Way Dust Map predicts a distance of $2 - 2.5$ kpc; using the measured $m_J = 14.2$ in combination with $M_J = -1.65$ the distance modulus suggests $d \simeq 2 - 2.5$ kpc only when $E(B - V) = 1.1 - 1.3$. The agreement of these two independent spectral interpretations lends confidence to an MIII type, and we suggest CX117 is likely a symbiotic system.

CX118: Nova-like CV

CX118 was identified as a nova-like CV at $E(B - V) = 0.8$ or $d = 1.2 - 1.8$ kpc with the optical light dominated by the accretion flow emission (Wevers et al., 2017). Spectroscopy was unable to reveal photospheric lines in either the WD or donor. The SED shows signs of binarity (specifically in the optical) and we test a simple double blackbody model shown (Figure 2.18) and observe that the optical region includes a large fraction of its flux from the hot component, in agreement with a hot accretion disk in an NL system. The model overestimates the *GALEX* flux but underestimates UVM2 by $\simeq 0.8$ mags despite the filter's position centered in the UV-extinction bump that may indicate large-scale UV variability. CX118 also shows optical variability of $\simeq 0.7$ magnitudes over the timescale of a few days (Britt et al., 2014). We find a single IR counterpart in the *GALEX* circle with a quoted FAP of 0.2% (Greiss et al., 2013) and its position in $(J - H, H - K)$ suggests an M1-3III giant at $E(B - V) \lesssim 0.4$ and a mid-KIII at higher extinction. Assuming $d = 1.2 - 1.8$ kpc and computing the absolute J magnitude with the distance modulus (with $m_J = 15.062$) we find $M_J = 13.1$ to 14.1 for the lower and upper distances respectively, corresponding to a brown dwarf \sim L4-L7V. However, the double blackbody model indicates the hot component contributes a non-negligible amount in the IR and so IR

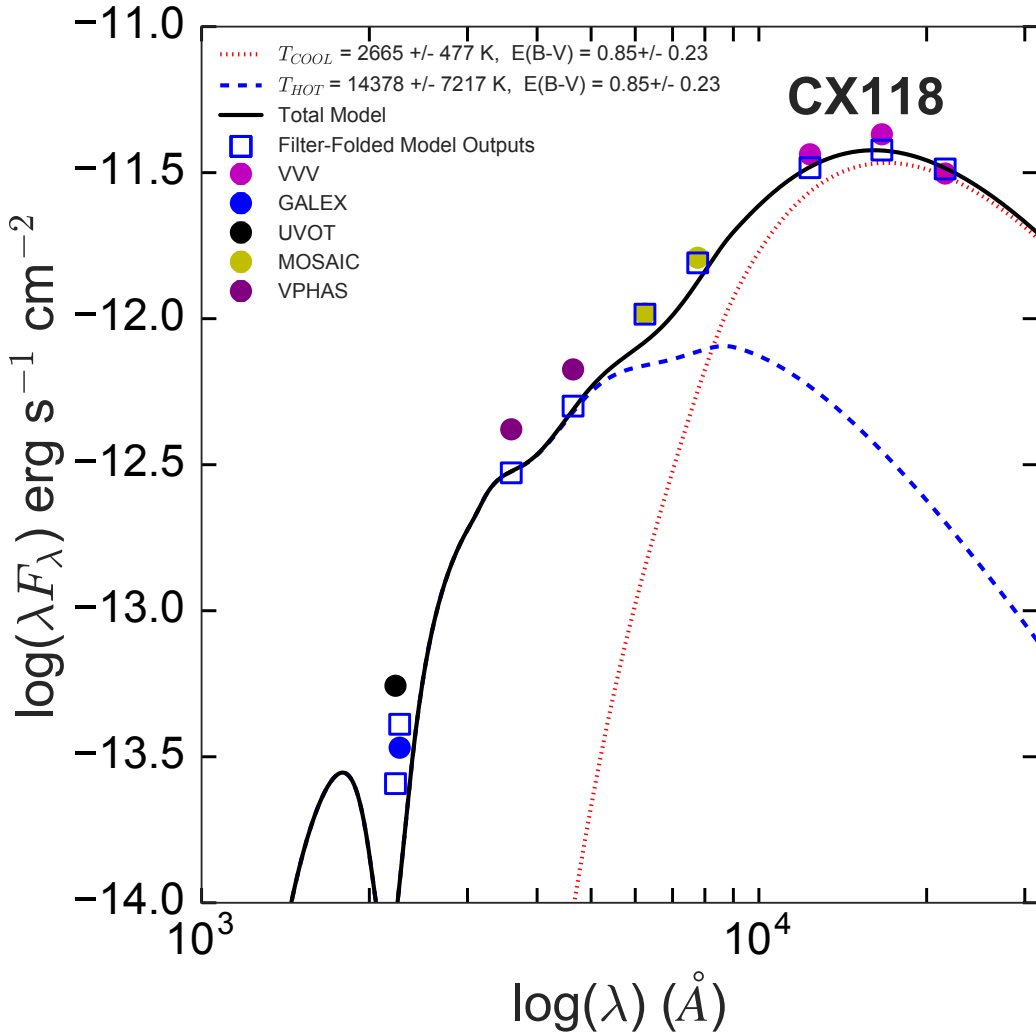


Figure 2.18: CX118 modelled with MCMC as a two blackbody system.

colours may not represent the donor.

CX137: CV/qLMXB

CX137 is a low accretion state CV or qLMXB (Torres et al., 2014) due to broad H α emission (FWHM and EW, 960 km/s and 6.5 Å respectively), a sinusoidal light curve with a period of 0.2 days (a period initially quoted by Udalski et al., 2012) and the presence of photospheric lines reminiscent of a late G/K star. Low optical flickering likely means the optical light is companion-dominated

following the suggestion of Torres et al. (2014) of a K5V companion; we also find only small NUV variations over 100 minutes of (non-contiguous) *GALEX* time-series data using the *gPhoton* package, meaning the NUV emission is likely dominated by the compact object and/or an accretion disk. We test a K5V + blackbody model where modelled parameters are normalizations, blackbody temperature and E(B-V) using the Markov-Chain Monte-Carlo package *emcee* (Foreman-Mackey, 2016). The SED (Figure 2.16) looks like two bodies: we test MCMC modelling with two blackbodies finding a possible hot component at $T_{bb} \simeq 10000$ K although the temperature is fairly unconstrained (see Figure 2.19). The UVOT data point is well below the *GALEX* datapoint and this may be due to non-simultaneous data or inherent variability.

CX161: Chromospherically-Saturated M-dwarf

CX161 has a very close *GALEX* counterpart at an offset of 0.344''. Britt et al. (2014) indicated this source is probably an M dwarf flare star with a period of 3.32 days (they observed a flare event). Formally, the best fit with and without UV is an M6V and the UV excess is exceptionally large (9+ mags). It is at the upper end of the M-dwarf relation in Figure 2.15 indicating a rapidly rotating M-dwarf, and assuming the observed period is due to rotation from observed starspots, $P_{rot} \sim 3.32$ d and thus $R_0 = P_{rot}/\tau_c \simeq 0.07$ (as $\log(\tau_c = 1.67)$ from Equation 1.7 using the M6V mass). Recalling saturation in late-types occurs at $R_0 \simeq 0.1$ (Stepien, 1994) and activity increases with decreasing R_0 , our work supports the identification by Britt et al. (2014) that CX161 is an M-dwarf flare star.

CX331: Active M-Dwarf / RS CVn

CX331 was identified as a variable source with an optical light-curve similar to a spotted star or RS CVn, with an period of 18.215 days and $I = 17.277$ (Udalski et al., 2012). The SED shows a difference of ~ 0.75 mags in VPHAS

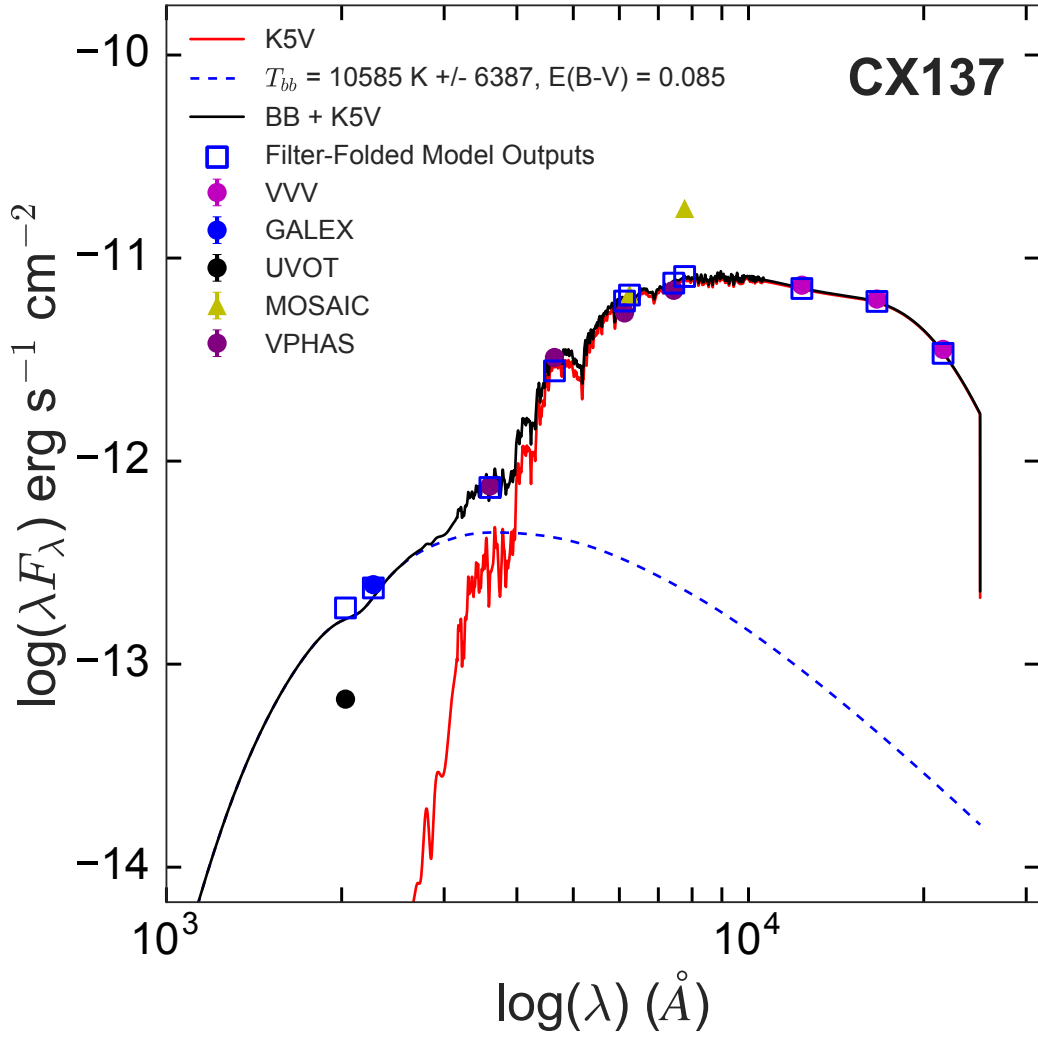


Figure 2.19: CX137 modelled with MCMC as a K5V + hot blackbody component.

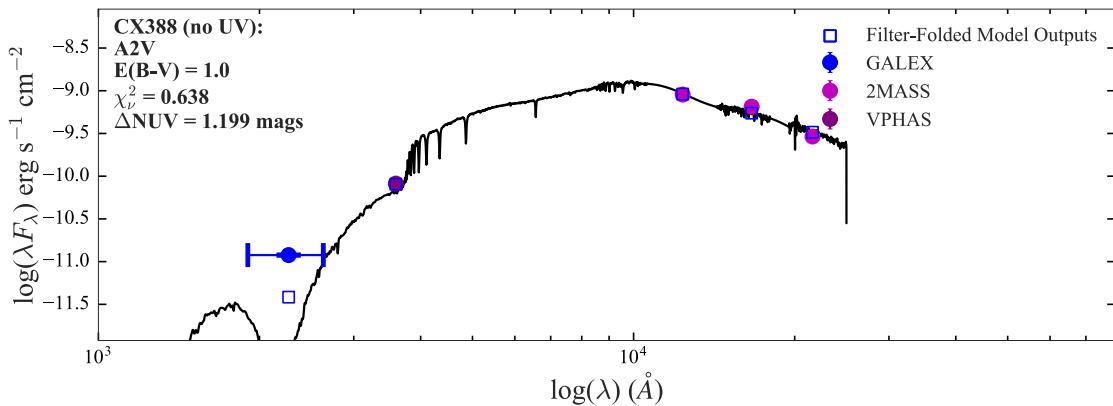
and MOSAIC r' and i' bands that could be attributed to orbital variability in the RS CVn interpretation. The chromospheric UV excess is not larger than that expected for active M-dwarfs in general and the IR colours suggest a reddened ($\sim 0.2 - 0.5$) MV or a MIII with little to no extinction (Figure 2.11) although they may be blended from binarity. Both the UV excess and observed variability supports the RS CVn interpretation with an M-type cool component.

CX388: ?

CX388 appears to be quite variable in both optical and near UV. SDSS imaging (from ds9) shows an oblong feature (Figure 2.20) that may be two or more sources in the line of sight. This is confirmed by Hynes et al. (2012) who note a nearby Tycho-2 source as an interloper ($R_X \simeq 1.1''$), and this source corresponds spatially with the *Swift* UVOT data and we believe the *GALEX* circle as well. However, UVOT's positional error is only $\sim 0.1''$, and we believe the Tycho-2, *GALEX* and UVOT data correspond to one system while 2MASS/VPHAS/*Chandra* are another. The latter system is well-fit without the UV as an A2V at $E(B - V) = 1.0$ ($\chi^2_\nu = 0.638$) corresponding to $d \simeq 2.66$ kpc (see Figure 2.20). However, working back the absolute magnitude from the distance modulus and extinction does not match this interpretation.

CX398: WD+MIII Symbiotic System

CX398 has relatively large errors on both H and K band observations in VVV (0.18 and 0.2 respectively; Greiss et al., 2013) and spectral fitting cannot produce any reasonable chi-squared values with or without the UV. Checking the optical and IR images confirms that these datapoints indeed satisfy the same emitter, and the shape of the optical/IR broadly suggests a mid-MIII suggesting CX398's X-ray and UV emission could be from a WD interaction in a symbiotic system.



CX388: DSS/STSCI

(ds9, zscale+power)

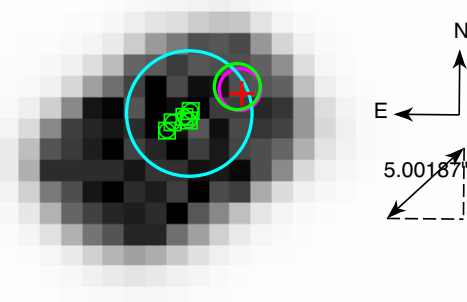


Figure 2.20: (top) Best-fit spectrum of CX388, without fitting *GALEX* UV. UVOT data was not included in the initial fitting procedures. (bottom) Optical SDSS image of CX388 using ds9. Data shown are *Chandra* (green circle, 1.1"), *GALEX* (cyan circle, 3.0"), VPHAS (magenta circle), 2MASS (red cross), UVOT (green squares).

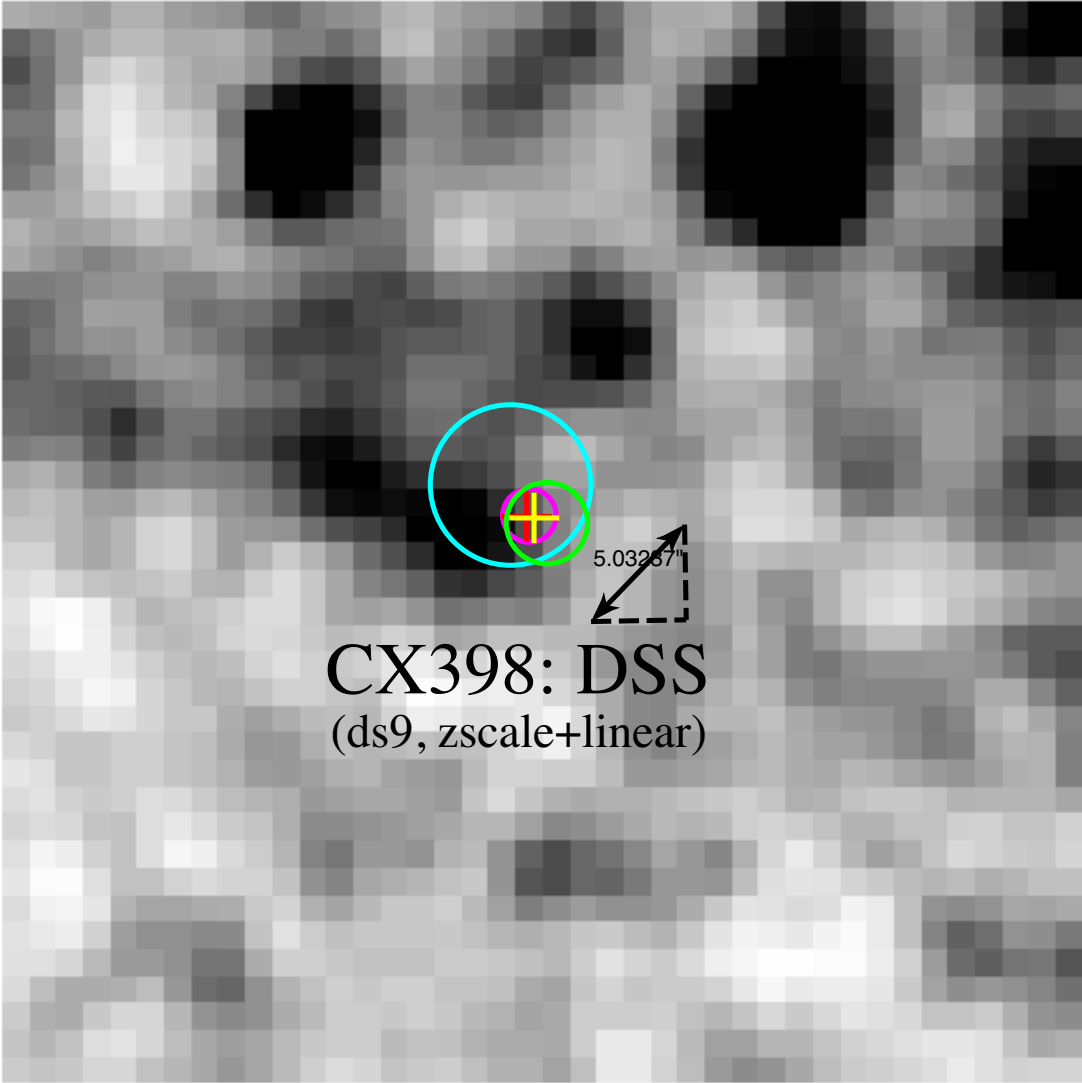


Figure 2.21: Optical SDSS image of CX398 using ds9. Data shown are *Chandra* (green circle, 1.52"), *GALEX* (cyan circle, 3.0"), *VPHAS* (magenta circle), *MOSAIC-II* (yellow cross) and *VVV* (red cross).

CX417: Nova-like CV?

CX417 is an optically periodic source with a period $p = 0.95923$ d (I band, Udalski et al., 2012). Its SED is bimodal with the hot component's UV flux exceeding the IR flux from the cool companion. Figure 2.22 shows CX417 is well-modelled by a cool star (4100 ± 150 K) and a larger, hotter component (30000 ± 7000 K) possibly indicating the presence of a hot and optically-thick accretion disk. A disk temperature of ~ 30000 K means it would be in a consistently high \dot{M} state; the boundary layer in high \dot{M} nova-like CVs is found to have its X-ray spectrum thermalized with an approximate blackbody temperature of $kT_{bb} \sim (GM_{WD}\dot{M}/8\pi\sigma R_{WD}^3)^{1/4} \sim 10\text{eV}$ or $T_{bb} \sim 10^4$ K (Lewin and van der Klis, 2006, chap. 10.2.2) putting this disc in the right range for nova-likes. Assuming all liberated energy is thermalized and $\dot{M} \sim \dot{M}_{crit} \simeq 10^{-10} M_\odot \text{yr}^{-1}$ (Patterson et al., 1984), $L \sim 10^{33}$ erg/s which is in the correct range for accreting CVs but slightly high for nova-likes. Lastly, assuming the observed periodicity is the orbital period P_{orb} indicates a (slightly evolved) solar-like donor. We conclude that CX417 is plausibly a nova-like CV.

CX418: CV / Symbiotic System

CX418 is decently fit without UV as a G5III ($\chi_\nu^2 = 1.887$) at $E(B - V) = 0.6$ and its IR colours suggest G or early KIII companion. Figure 2.15 indicates its UV-excess flux is considerable, and it lies along the expected line for the nearby M-dwarf population. This indicates that, if a giant, the UV is more active than is represented by the merged Pickles template of such giants. Assuming a G5III at $E(B - V) = 0.6$ yields $d = 5 - 5.1$ kpc (this is a relatively low-extinction sightline) from the Milky Way Dust Map, which is corroborated by a distance modulus computation. A distance of 5 kpc yields $L_X \sim 2 \times 10^{32}$ erg/s indicating this is either a CV or a symbiotic system.

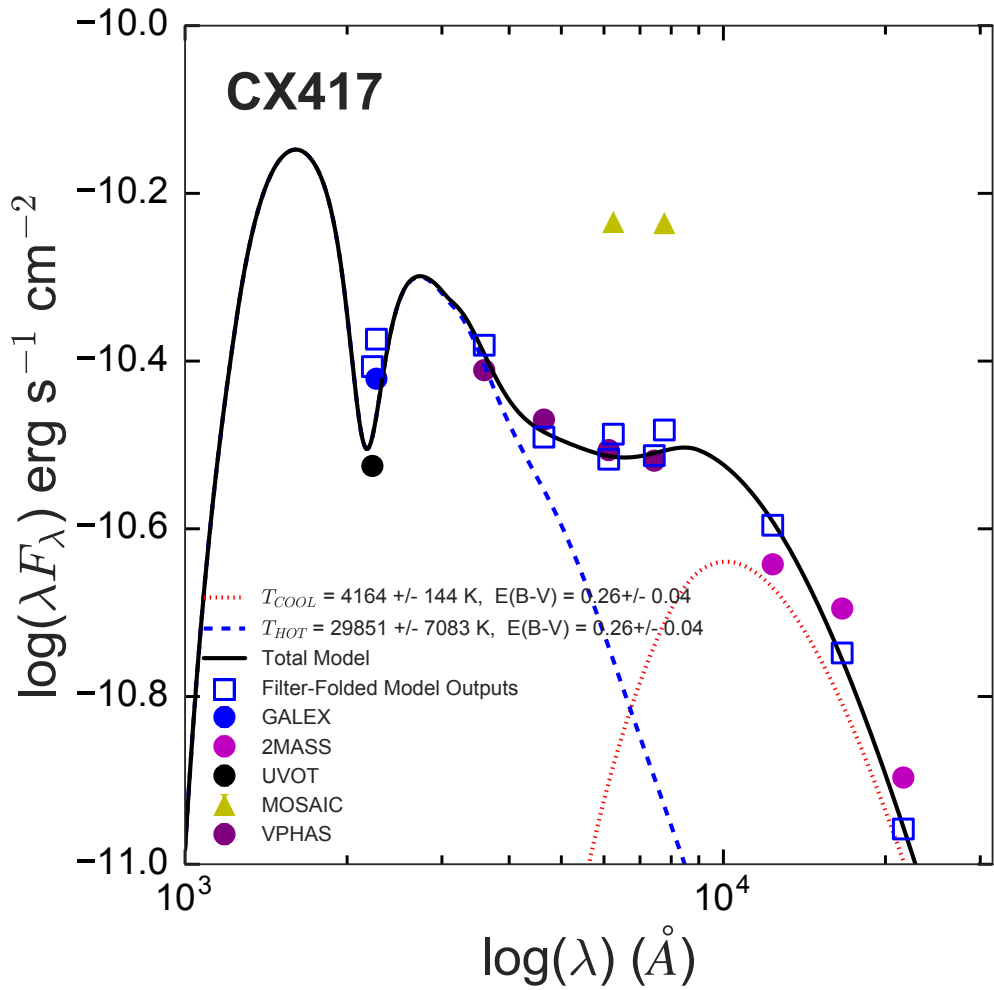


Figure 2.22: CX417 modelled using MCMC as a system of two blackbodies with extinction.

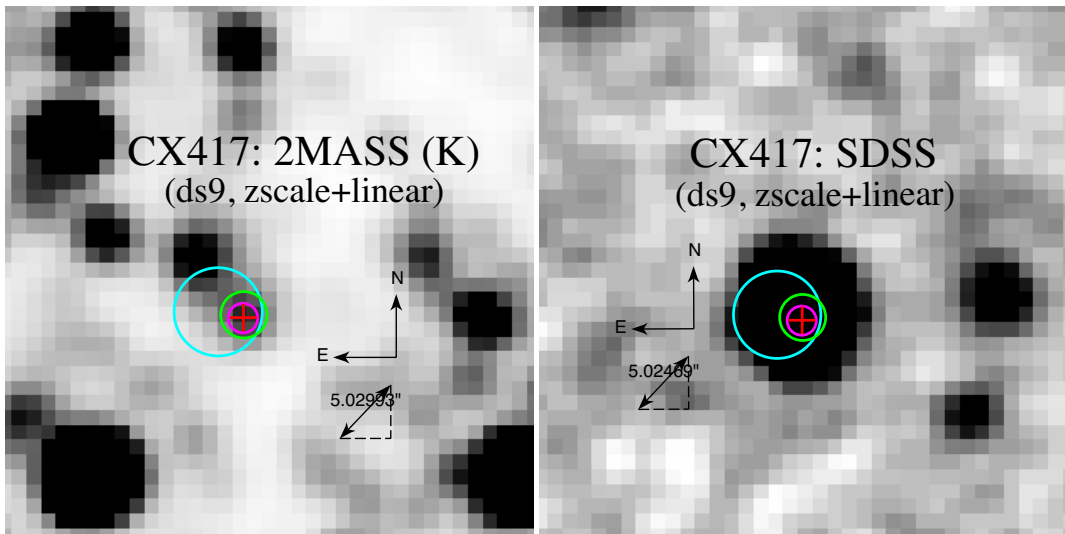


Figure 2.23: (left) 2MASS K_s and (right) SDSS image of CX417. Data shown are *Chandra* (green circle, 1.1"), *GALEX* (cyan circle, 3.0"), VPHAS (magenta circle), 2MASS (red cross), UVOT (green squares). The (comparatively brighter) IR source in the upper left of the *GALEX* circle is not revealed in the optical image. The optical brightness of X-ray position suggests the presence of nova-like accretion disk.

CX426: Dwarf Nova CV

CX426 is a CV undergoing dwarf nova bursts (Britt et al., 2014; Udalski et al., 2012). The VVV data shows a prominent rise in the H band, although the VVV source is farthest from the X-ray and *GALEX* position and may not be physically associated.

CX495: M-dwarf, Possible CV

CX495 was quoted as a periodic source with $P = 0.48629$ days by Udalski et al. (2012) and its IR colours and spectral fitting suggest an M5V or M5III at $E(B - V) = 0.3 - 0.4$ (from spectral fitting) although the photometric errors on J and H are large (0.24 and 0.36 mags respectively). The UVOT and *GALEX* fluxes suggest inherent variability that could be associated with coronal flaring from an M-dwarf or flare-like events in an WD + MIII symbiotic. Assuming distances of 100, 500 and 800 pc the distance modulus (with the appropriate A_λ values for each distance from Green et al., 2015) returns absolute J magnitudes in the range of M0-M8V; at 800pc, $L_X = 4.9 \times 10^{30}$ erg/s, well within the range of active M-dwarfs. An M-dwarf with $P_{rot} = 0.48629$ d would be a saturated rotator with $\log(L_X/L_{bol}) \simeq 0.3$ capable of strong flaring supporting the distance modulus result. Photometrically, an MIII requires $d > 3 - 4$ kpc corresponding to $E(B - V) > 1.6$ from the dust map, making an M-dwarf interpretation much more likely. CX495 is either a single, flaring M-dwarf or an M-dwarf/WD CV system.

CX497: Active Star

CX497 is a periodic source with $P = 3.4961$ days and noted as a possible spotted star (Udalski et al., 2012). The SED resembles a single star and the UV excess is not overwhelming; it doesn't statistically fit any one model but there is little evidence of binarity or a coupled rise in the optical. The IR colours are difficult to interpret uniquely given unknown $E(B - V)$, but CX497

is formally best fit as an F5V at $E(B - V) = 1.0$ ($\chi^2_\nu = 1.755$). The 3D Milky Way Extinction Map does not cover CX497's position (so we cannot infer distance from $E(B - V)$), but assuming a relatively nearby 1kpc (5kpc) yields $L_X \sim 8 \times 10^{30}$ erg/s ($L_X \sim 2 \times 10^{32}$ erg/s) within the range of active stars. CX497 is a single, chromospherically-active dwarf.

CX551: ?

CX551 is saturated in MOSAIC-II and otherwise has no data in other optical bands. Its IR colours place it to the right of the MS-curve in Figure 2.11 indicating either a real IR excess in the K_s band or a positional blend. We have no other information on CX551.

CX645: CV/qLMXB

CX645 was suggested as a possible CV/qLMXB due to the detection of eclipses, ~ 1 mag flare events and large, aperiodic variability (Britt et al., 2014). The SED shows a discrepancy between VPHAS and MOSAIC-II which reflects this inherent variability. Greiss et al. (2013) identify 3 VVV sources within 2.2" and we initially identified one at edge of the X-ray circle ($\sim 1.64''$) (see Figure 2.24). This VVV source may be unrelated to the optical emission - the image shows the VPHAS/MOSAIC-II correspond to the same position but VVV sits slightly outside this region. As well, the IR fluxes are far brighter in the SED and indicate this is likely an interloping IR source. A check of the 2MASS catalogue reveals no sources in the *GALEX* circle; if VVV did not pick it up the upper limit of the donor IR is $K_s \geq 17.5$ mag (Minniti et al., 2010). The lack of an IR counterpart means this source is quite blue (suggested as well by Britt et al., 2014) where the blue continuum is disk-dominated.

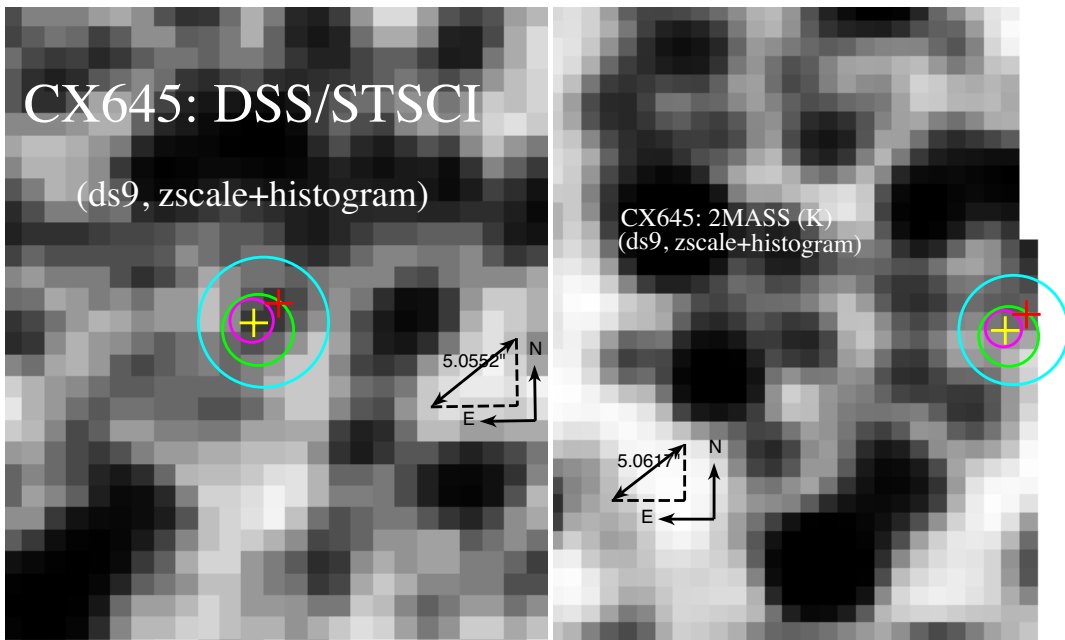


Figure 2.24: (left) DSS optical and (right) 2MASS K_s image of CX645. Data shown are *Chandra* (green circle, $1.64''$), *GALEX* (cyan circle, $3.0''$), VPHAS (magenta circle), 2MASS (red cross) and MOSAIC-II (yellow cross). The right image is the returned 2MASS image in the ds9 query, despite it not being centered perfectly.

CX662: Active M-Dwarf

CX662 has a close *GALEX* match 0.95" away and fits a variety of late-type profiles (without UV) at multiple extinction values. The general shape of the SED resembles a single stellar source with only a moderate UV excess. Although not in the data table of Udalski et al. (2012), Simbad indicates CX662 as an OGLE-IV bulge source (OGLE BLG504.22 107804) with $V - I = 1.859$. This optical colour assuming $E(B - V) \sim 0$ suggests an M0V-M1V and its position in Figure 2.11 supports this interpretation. Assuming a distance of 100 pc yields $E(B - V) \sim 0$ and the distance modulus returns an absolute magnitude $M_J \simeq 7.9$ suggesting an M3V-M3.5V. We conclude CX662 is likely an active, early M-dwarf with no signs of binarity or a compact object.

CX673: ?

CX673 is difficult to interpret because it has an optical detection but is comparatively very dim in the IR ($K_s > 17.5$). Neither of the two VVV counterparts from Greiss et al. (2013) appear to coincide with the optical emission in VPHAS/MOSAIC. Figure 2.25 shows the single VVV source in the *GALEX* circle and the closest known 2MASS source taken from the ds9 catalogues. $r' - i' \simeq 1.3 - 1.4$ in both optical surveys suggesting the optical component is an M-dwarf with modest activity but its non-detection in VVV places a lower limit on the infrared brightness of $K_s > 17.5$ (Minniti et al., 2010).

CX886: ?

The 2MASS and DSS images of CX886 (Figure 2.26) show that the *GALEX* position encapsulates the VPHAS/MOSAIC point (with $r' - i' = 2.23 \pm 0.06$) at the edge of its 3" error circle that may be unassociated with the UV point entirely. The *Chandra* circle is fairly large at $R_X = 6.57"$, and Greiss et al. (2013) lists 3 VVV sources within $\sim 2.5"$. The ‘chosen’ counterpart matches

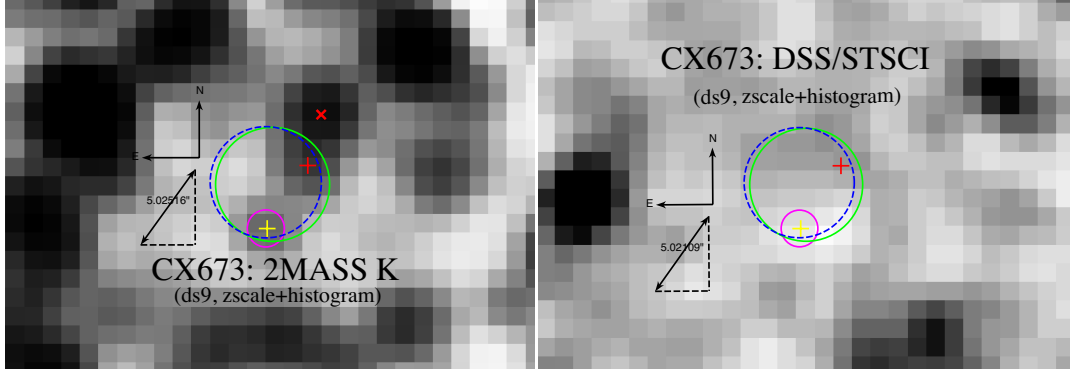


Figure 2.25: (left) 2MASS K_s and (right) DSS optical image of CX673. Data shown are *Chandra* (green circle, $3.076''$), *GALEX* (blue, dashed circle, $3.0''$), VPHAS (magenta circle), VVV (red +) and MOSAIC-II (yellow +). The red X is the closest 2MASS source to this system, and does not appear within either the *GALEX* or *Chandra* circles.

the *GALEX* position, but is $\sim 3''$ from the VPHAS/MOSAIC source. The X-ray, UV and the VVV source may be a single emitter, while the optical points are an interloper. Assuming this case, an SED fit (with only *GALEX* and VVV) strongly suggests an M8-M9III giant at $E(B - V) < 1.0$ or an M-dwarf at $E(B - V) \sim 1 - 2$ (see Figures 2.11 and 2.27), but at such low extinction we would expect to pick up an MIII in the optical.

Testing an M5V ($M_J = 10.14$, AB mags) at $E(B - V) = 1.0$ ($d = 2.77\text{kpc}$) returns a simulated $m_J > 24$ which is far too dim (our observation shows $m_J \simeq 16.1$). A non-detection in MOSAIC-II places an optical upper limit of $r' > 22.66$ and $i' > 21.47$ (AB mags). The extinction in this direction is $E(B - V) = 0.5, 1.0, 1.5$ at $1.1\text{kpc}, 2.78\text{kpc}$ and 6.4kpc respectively suggesting that an M-dwarf at $E(B - V) \geq 1.0$ is also too distant to be picked up in *GALEX*.

To test the M8III hypothesis we create a synthetic M8III observation using `pysynphot`, normalized to its J band observation and ‘observe’ it in the optical r’ band. With no extinction $r'_{sim} = 21.57$ and at $E(B - V) \simeq 0.43$ ($d \simeq 1\text{kpc}$) we find the $r'_{sim} = 22.5$, the optical limit of MOSAIC-II. This supports the best-fit M8III at $E(B - V) \sim 0.4$ or $d \sim 1\text{kpc}$ from our spectral fitting (Figure

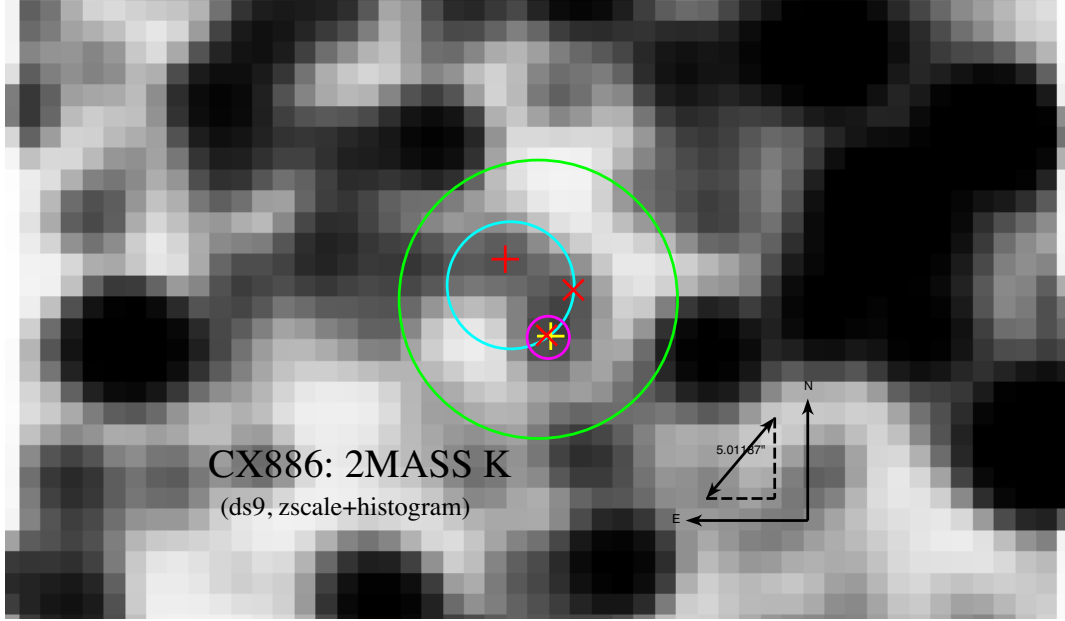


Figure 2.26: (left) 2MASS K_s and (right) DSS optical image of CX886. Data shown are *Chandra* (green circle, 3.076''), *GALEX* (cyan circle, 3.0''), VPHAS (magenta circle), VVV (red +) and MOSAIC-II (yellow +). The red Xs are two other VVV sources (Greiss et al., 2013) that were not selected in the matching algorithm.

2.27) and suggests that this interpretation is at least consistent with the optical survey limits. At this distance, $L_X = 4 \times 10^{30}$ erg/s - this is low for symbiotics, however we still retrieve sensible spectral fits up to $E(B - V) = 0.9$ for the MIII companion, suggesting the luminosity could be up to $L_X \sim 10^{31}$ erg/s.

CX1029: ?

The VPHAS/MOSAIC/VVV data correspond to a single point on the edge of the *GALEX* circle; querying a few different optical catalogues in ds9 revealed a USNO A2.0 (reference, epoch 1980) catalogue match to the *GALEX* position at $B, r = 18.4, 14.1$ mags (or 18.97 and 14.12 upon conversion from USNO

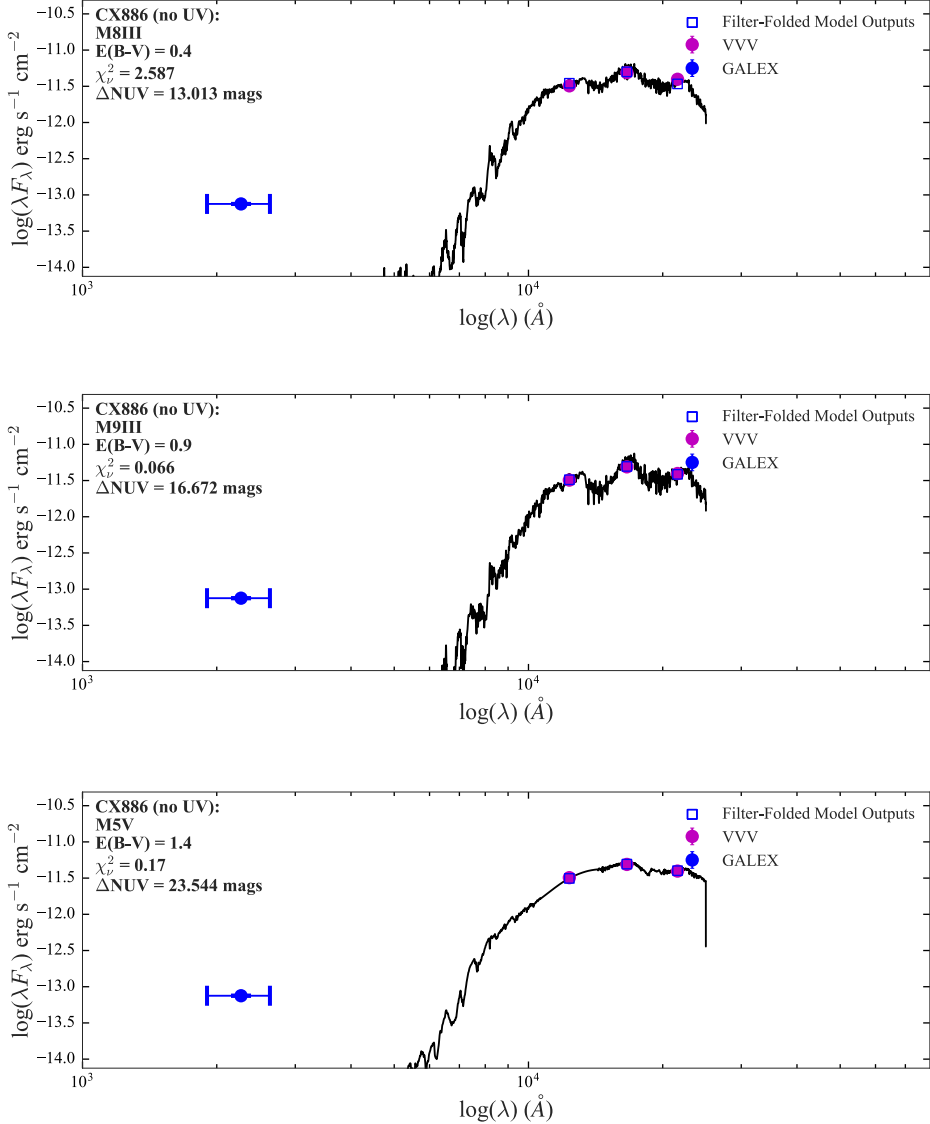


Figure 2.27: Three different spectral fits for CX886, using only the *GALEX* and the VVV source nearest to its center (corresponding to the red + in Figure 2.26). Assuming these emissions are correlated, this looks like an MIII with a UV excess, although the *GALEX* source could actually be associated with the VPHAS/MOSAIC source (see Figure 2.26).

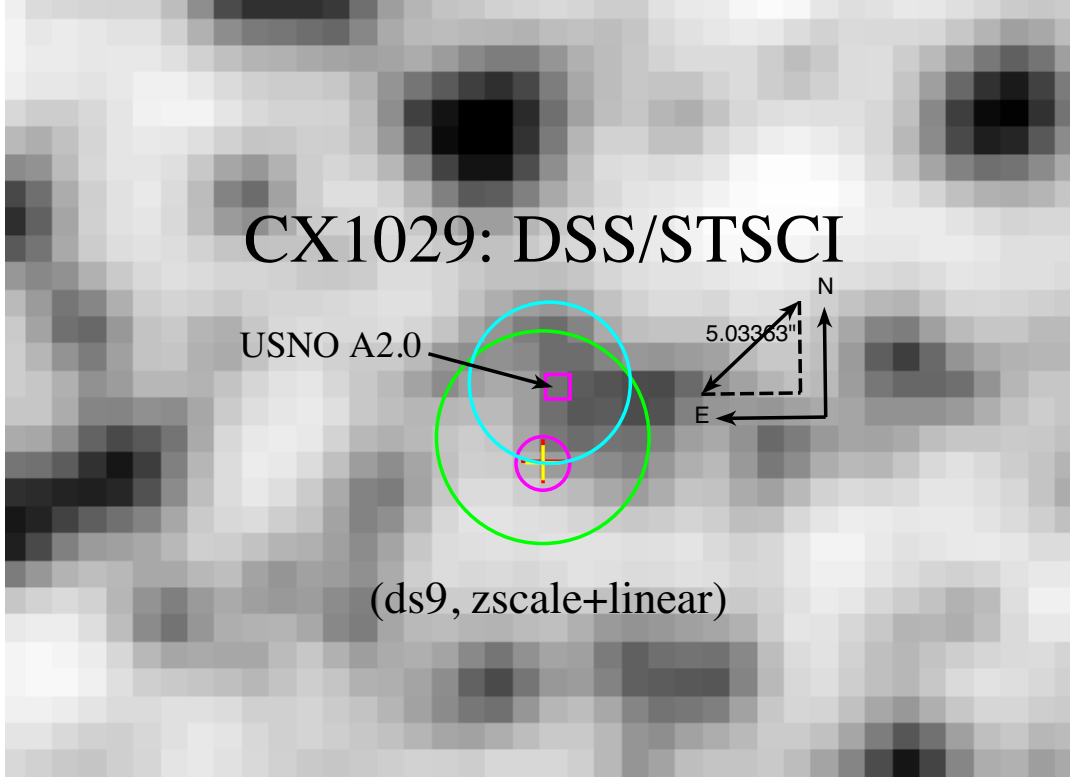


Figure 2.28: DSS optical image of CX1029. Data shown are *Chandra* (green circle, 3.96''), *GALEX* (cyan circle, 3.0''), VPHAS (magenta circle), VVV (red +) and MOSAIC-II (yellow +). The magenta square shows the USNO A2.0 ($B, R \sim 18, 14$) optical source found from a ds9 query.

standard to Landolt filters¹⁰). Assuming $E(B - V) = 1$ ($d \sim 3\text{kpc}$) yields $L_X \sim 3 \times 10^{31} \text{ erg/s}$; CX1029 is quite red and if a binary has a M or K type giant donor. Spectral fitting indicates an M0III-M3III at low extinction and K0III-K3III at $E(B - V) \geq 1.0 - 1.5$ suggesting a symbiotic system (see Figure 2.11).

CX1042: Active M-dwarf

CX1042 is probably an active M-dwarf. The optical image shows the VPHAS, MOSAIC and VVV data correspond to the same point although the *GALEX* is offset by almost 3'' - there are no other visual optical emitters in the cor-

¹⁰http://quasars.org/docs/USNO_Landolt.htm

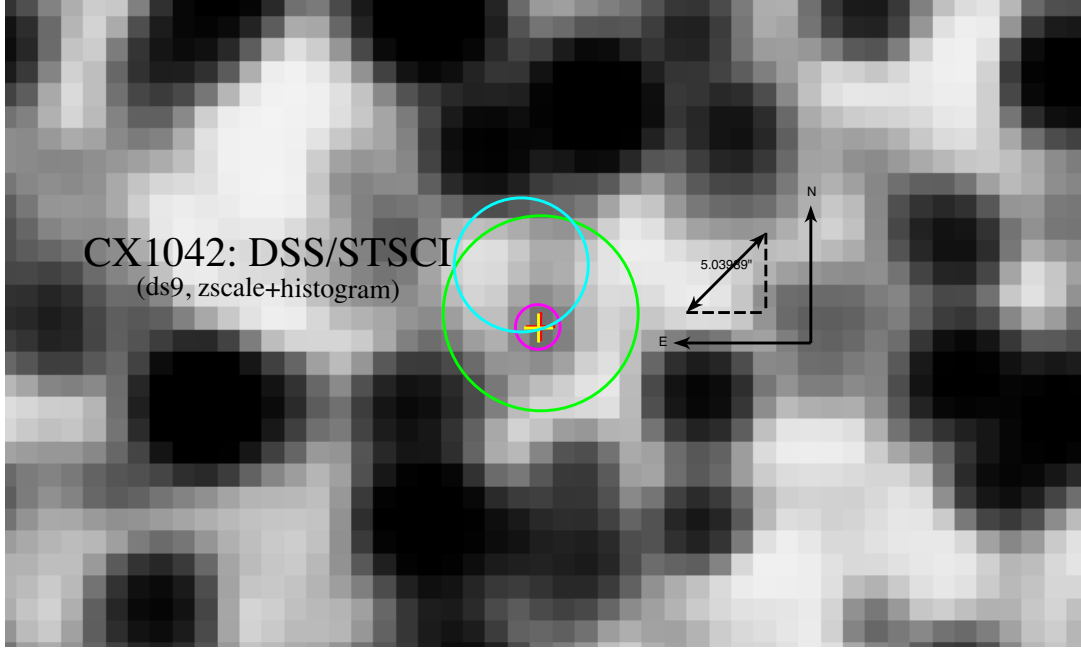


Figure 2.29: DSS optical image of CX1042. Data shown are *Chandra* (green circle, $4.364''$), *GALEX* (cyan circle, $3.0''$), VPHAS (magenta circle), VVV (red +) and MOSAIC-II (yellow +).

responding image leading us to believe these datapoints are likely all related. The SED reveals a slight discrepancy between the two optical surveys, and this discrepancy is likely the reason it was not statistically well-fit excluding UV. The IR region is well-fit by an M4V-M5V at $E(B - V) \sim 0$ and its position in Figure 2.15 leaves it comfortably in the regime of active M-dwarfs. Even in the event the UV is associated with this system, CX1042 is plausibly an active M-dwarf.

CX1229: ?

Udalski et al. (2012) found that CX1229 shows irregular optical variability with an average $V - I = 1.770$. Spectral fitting without the UV suggests CX1229 could be an active KV-MV, and the UV flux may come from an interloping optical source at $V = 14.38$ found in the GSC 2.3 catalogue flagged as ‘non-star’, likely due to source confusion making the PSF non-point-like. This source lies in the *Chandra* error circle and is noted as such in Figure 2.30; whatever

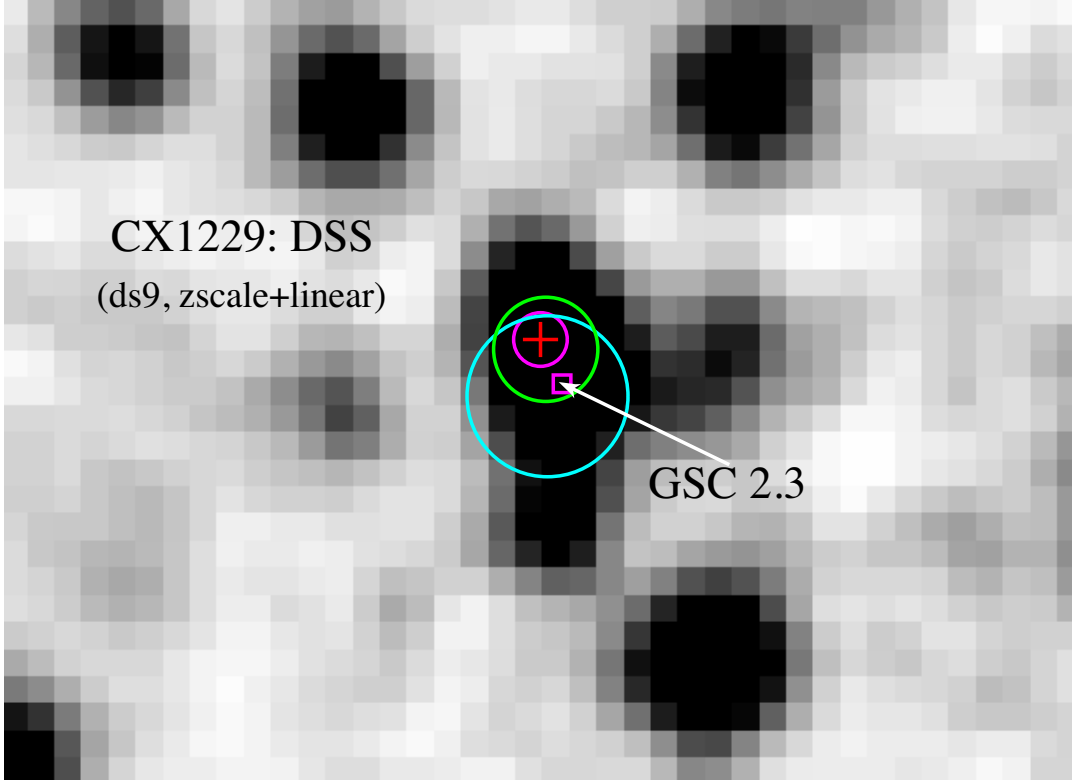


Figure 2.30: DSS optical image of CX1229. Data shown are *Chandra* (green circle, 1.94"), *GALEX* (cyan circle, 3.0"), *VPHAS* (magenta circle), *VVV* (red +). The magenta square is the optical GSC 2.3 source in the *Chandra* circle.

this emitter is could also be the source of X-rays. If this is a binary system with variability it could be flagged as non-star which supports variability from the Udalski et al. (2012) observation.

CXB10: CV

CXB10 is a dwarf novae CV. Its position coincides with the dwarf novae OGLE-BLG-DN-0376 (Mróz et al., 2015) also observed in the MACHO survey as MACHO 401.48296.2600 (Cieslinski et al., 2004). CXB10 was observed in multiple outbursts where the maximum I-band intensity, outburst amplitude, frequency and mean duration are 5.070 mag, 4.183 mag, 1.169 yr^{-1} and 7.7 days. We retrieved a single optical point in the VPHAS u' band (the rest are off-image in the original VPHAS data) but no other multi-wavelength observations.

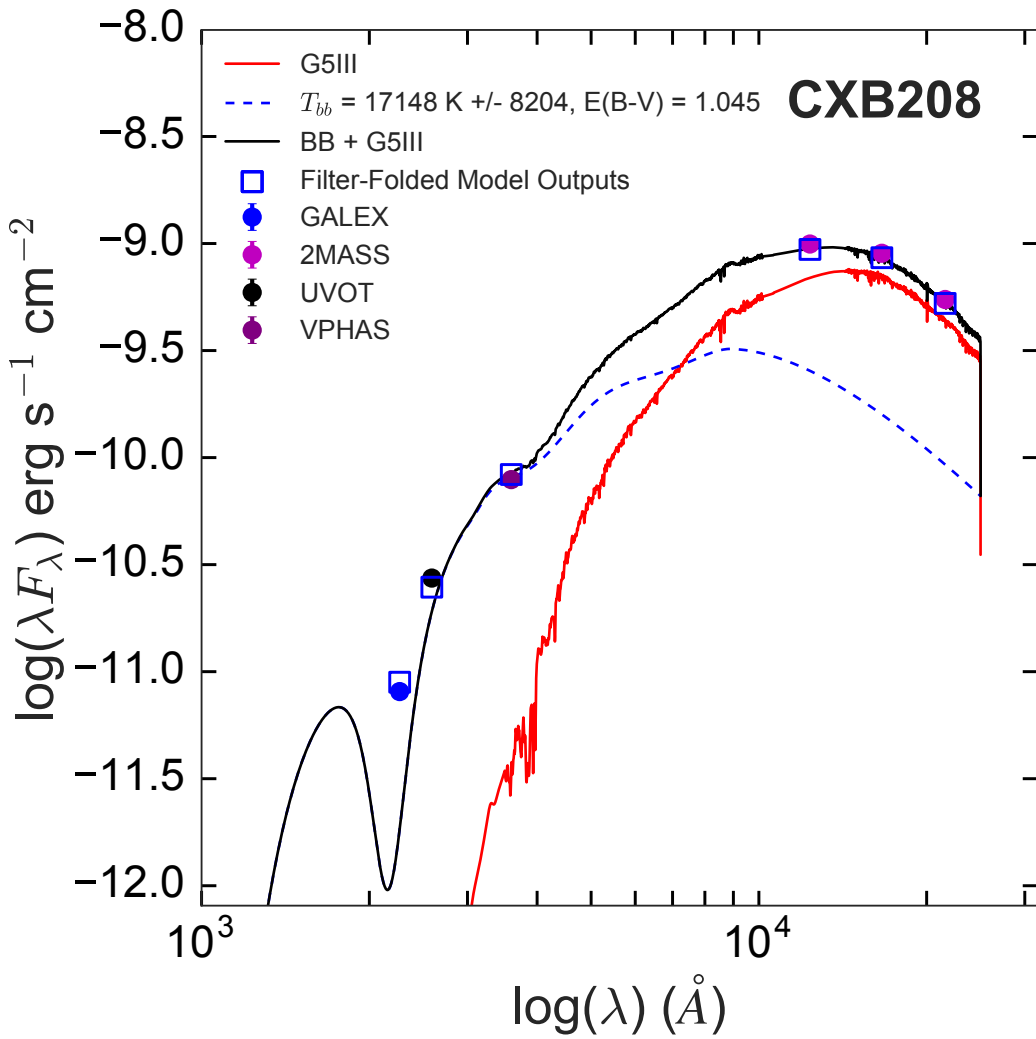


Figure 2.31: CXB208 modelled with MCMC as system of two blackbodies with extinction. Despite the large spread in the hot-component temperature, the posterior distribution is smooth in all variables and the UV rise is difficult to achieve with one source in general.

The *Chandra* error is small enough ($\sim 1''$) to confidently exclude other bright stars nearby.

CXB208: Symbiotic CV

Spectral fitting indicates CXB208 could be an A-K giant (depending on $E(B - V)$), and we have included a UVOT UVW1 flux in spectral fitting between *GALEX* and VPHAS u'. Only in the case of an AIII at $E(B - V) = 1.0$ is the *GALEX* UV properly matched, but this comes at the expense of a poorer fit in the IR region. The *GALEX*-UVOT-u' and IR regions both ‘turn over’ implying binarity - MCMC modeling reveals this is plausible ($T_{hot} = 15100 \pm 6000\text{K}$, $T_{cool} = 4500 \pm 800\text{K}$) although this overestimates the *GALEX* flux (this could indicate inherent UV variability). This variability in combination with a giant donor makes CXB208 a symbiotic candidate; the cool blackbody temperature also agrees with a G or K giant interpretation. Assuming a G5III at $d = 1$ kpc yields $E(B - V) = 0.27 \pm 0.06$ - combining this with observed $m_V = 11.3$ (from the GSC 2.3 catalogue) yields an expected $M_V \sim 0 - 1$ in the range of G-K giants. Spectral fitting at $E(B - V) = 0.3$ also reveals a G5III as the best-fit template. We re-model CXB208 using MCMC assuming a G5III donor (Figure 2.31) and hot blackbody, finding a WD temperature of $T_{WD} \sim 17000 \pm 8000$. We claim CXB208 is a symbiotic system at $d \sim 1$ kpc and $L_X \sim 10^{30} - 10^{31}$ erg/s. Optical spectroscopy and timeseries data in either the optical/UV can confirm its symbiotic nature.

2.7 Summary & Conclusions

We identified 269 positional matches between the *GALEX* NUV and *Chandra* X-ray dataset in the GBS. By assuming the *GALEX* UV emission correlates with X-ray emission the ambiguity of optical and IR counterparts was significantly reduced, such that each survey was iteratively matched to the

GALEX positions. With the accrued photometric data we constructed SEDs for each system and modelled them against the Pickles Library of single-stellar templates. The majority of the *GALEX/Chandra* dataset consists of active, late-type single stars/binaries with X-ray and UV emission primarily from hot, magnetically-confined coronae. This population is also local (for by definition they have fit a single spectrum at $E(B - V) < 1$) and possibly young, with G and F dwarfs dominating the spectral type distribution. We showed that SED fitting at least in the NUV-IR regime is not necessarily a good indicator of an active binary system like an RS CVn, at least as far as observing the cool companion. Hence, many of the coronally-active sample are binaries with companion-enhanced UV fluxes. If it is unlikely that we have heavily sampled young stellar populations altogether, a higher active binary fraction could be invoked as an explanation of these activity levels and vice versa.

The ability of X-ray/UV crossmatching to identify compact binaries was successful, in that it recovered 9 previously identified CVs and/or qLMXBs. The total UV-excess sample is comprised of highly active M-dwarfs, new CVs and symbiotic candidates (CX398, CX495, CX1132, CXB208) and a yet unidentified population. Tabulated counterpart charts are available as supplementary online material, and we suggest pointed, simultaneous photometry (e.g., *Swift*) and/or optical spectroscopy be performed on the final UV-excess dataset.

Chapter 3

Thesis Conclusions & Future Research Directions

In Chapter 1, we reviewed ways in which compact objects emit high energy radiation from accretion-related processes in close binary orbits with another star. We finished with a brief introduction to the GBS, a shallow *Chandra* survey designed to locate a large quiescent LMXB population in the Galaxy. In doing so, it would homogenize the current sample of XRBs which is skewed towards bright and/or transient sources. In Chapter 2, we conducted a multi-wavelength analysis of 269 *Chandra* X-ray sources in the GBS using the *GALEX* UV dataset as a basepoint for counterpart matching. We performed SED fitting on photometric data from several optical and IR surveys, each with different photometric errors and standards. We found that the main areas of concern/error in accurately interpreting SED fitting of photometric data are a) the degeneracy of temperature, normalization and extinction and b) the high probability of inherent variability from a UV/X-ray-matched source in a Galactic dataset. For Galactic sources, knowledge of either $E(B - V)$ or distance yields the other with up-to-date dust maps of the galaxy, reducing this degeneracy. When extinction is known in advance, we recover many of the already-identified spectral types to an accuracy of ($\sim \pm 3$ sub-types) despite

real variation of stars within a single spectral type and differences in template libraries (a $\sim \pm 3$ sub-type difference also partially represents the precision to which these papers originally identified them).

The *GALEX/Chandra* dataset is dominated by coronally active single stars/non-compact binaries (RS CVn, Algols, BY Dra). These are B-M field stars peaking in the G-type, with very few M-dwarfs. There were 61 sources which could not be modelled by single-stellar templates alone, of which 30 are presented individually on the basis of UV flux excesses beyond empirical limits on single stars. The *GALEX* UV rise is often correlated with a rise in the nearby SDSS u' band as well revealing a smaller, hotter blackbody component. Although we did not directly identify a single LMXB in the dataset, these systems are the only sources whose SEDs would reasonably suggest so. We interpret 7 of these as accreting COs (likely accreting WDs), 5 of which appear to be plausibly symbiotic in nature with a KIII or MIII giant companion from spectral fitting. Shell-burning symbiotics show strong emission lines (e.g., H I, He II, OIII) (Section 1.1.2) and are steady in the UV. Non-shell burning symbiotics do not show such lines, and instead show short-timescale UV variability from the accretion disk. *GALEX* NUV *timeseries* data is now available in the *gPhoton* package (Million et al., 2016) in observing windows of $\sim 1 - 2$ ks in total and at least 100+ s per observation. The combination of (even low-resolution) optical spectra with UV timeseries could confirm either case and possibly identify them as part of the ‘hidden’ population (Mukai et al., 2016).

Finally, we suggest both *Swift* optical spectra and simultaneous *Swift* UVOT photometry in X-ray, UV and optical bands using the co-aligned XRT (0.3-10keV) and UVOT ($1930 \sim 5470$ Å) instruments for all 30 systems in the final UV excess set. Certainty of observational simultaneity removes the problem of variability and extensive UV coverage can identify $E(B - V)$ accurately: this is more or less the ideal SED analysis setup. Fine spectra may show any number of features: the equivalent width (EW) of $H\alpha$ elucidates the presence

of a disk, and can also distinguish between coronal activity and a CVs/qLMXB ($EW < 15 - 18$ Å limit for active chromospheres in M-dwarfs West et al., 2008). We may also estimate $E(B - V)$ using diffuse interstellar bands (DIBs). This spectral analysis would be conducted in a similar fashion to Torres et al. (2014) which identified 23 accreting binaries in the GBS by these spectral signatures. Even though an optical spectrum can provide as much or more information about a system than our SED analysis, it usually isn't clear *where* the spectrum observation should be centered. Only in cases where the X-ray positional error radius is small is this obvious, and the corresponding *GALEX* position is the suggested origin. We have also made available all photometric data, fitting results and plots to significantly reduce the collaboration's time in finding counterparts, converting them to a common flux system, assessing the relative photometric errors and performing the spectral fitting for reasonable extinction values.

Bibliography

Marcel A Agüeros, Scott F Anderson, Kevin R Covey, Suzanne L Hawley, Bruce Margon, Emily R Newsom, Bettina Posselt, Nicole M Silvestri, Paula Szkody, and Wolfgang Voges. X-Ray-Emitting Stars Identified from the ROSAT All-Sky Survey and the Sloan Digital Sky Survey. *The Astrophysical Journal Supplement*, 181(2):444–465, April 2009.

Stavros Akras, Lizette Guzman-Ramirez, Marcelo Leal-Ferreira, and Gerardo Ramos-Larios. Reclassifying symbiotic stars with 2MASS and WISE: An atlas of spectral energy distribution. *arXiv.org*, January 2017.

S C Barden. A study of short-period RS Canum Venaticorum and W Ursae Majoris binary systems - The global nature of H-alpha. *Astrophysical Journal*, 295:162–170, August 1985.

Robert A Benjamin, E Churchwell, Brian L Babler, T M Bania, Dan P Clemens, Martin Cohen, John M Dickey, Remy Indebetouw, James M Jackson, Henry A Kobulnicky, Alex Lazarian, A P Marston, John S Mathis, Marilyn R Meade, Sara Seager, S R Stolovy, C Watson, Barbara A Whitney, Michael J Wolff, and Mark G Wolfire. GLIMPSE. I. An SIRTF Legacy Project to Map the Inner Galaxy. *The Publications of the Astronomical Society of the Pacific*, 115(8):953–964, August 2003.

Michael S Bessell. The Hipparcos and Tycho Photometric System Passbands.

The Publications of the Astronomical Society of the Pacific, 112(7):961–965, July 2000.

Luciana Bianchi, A Conti, B Shiao, G R Keller, and D A Thilker. The Ultraviolet Sky: final catalogs of unique UV sources from GALEX, and characterization of the UV-emitting sources across the sky, and of the Milky Way extinction. *American Astronomical Society*, 223(6):254.09–912, January 2014.

C T Britt, M A P Torres, R I Hynes, P G Jonker, T J Maccarone, S Greiss, D Steeghs, P Groot, C Knigge, A Dieball, G Nelemans, V J Mikles, and L Gossen. Identification of Five Interacting Binaries in the Galactic Bulge Survey. *The Astrophysical Journal*, 769(2):120, June 2013.

C T Britt, R I Hynes, C B Johnson, A Baldwin, P G Jonker, G Nelemans, M A P Torres, T Maccarone, D Steeghs, S Greiss, C Heinke, C G Bassa, A Collazzi, A Villar, M Gabb, and L Gossen. Variability of Optical Counterparts in the Chandra Galactic Bulge Survey. *The Astrophysical Journal Supplement*, 214(1):10, September 2014.

C T Britt, T J Maccarone, J D Green, P G Jonker, R I Hynes, M A P Torres, J Strader, L Chomiuk, R Salinas, P Lucas, C Contreras Peña, R Kurtev, C Heinke, L Smith, N J Wright, C Johnson, D Steeghs, and G Nelemans. Discovery of a long-lived, high-amplitude dusty infrared transient. *Monthly Notices of the Royal Astronomical Society*, 460(3):2822–2833, August 2016.

David N Burrows, J E Hill, J A Nousek, J A Kennea, A Wells, J P Osborne, A F Abbey, A Beardmore, K Mukerjee, A D T Short, G Chincarini, S Campana, O Citterio, A Moretti, C Pagani, G Tagliaferri, P Giommi, M Capalbi, F Tamburelli, L Angelini, G Cusumano, H W Bräuninger, W Burkert, and G D Hartner. The Swift X-Ray Telescope. *Space Science Reviews*, 120(3):165–195, October 2005.

Jason A Cardelli, Geoffrey C Clayton, and John S Mathis. The relationship between infrared, optical, and ultraviolet extinction. *Astrophysical Journal*, 345:245–256, October 1989.

J Casares. Mass Ratio Determination from H α Lines in Black Hole X-Ray Transients. *The Astrophysical Journal*, 822(2):99, May 2016.

J Casares, D Steeghs, R I Hynes, P A Charles, and K O’Brien. Bowen Fluorescence from the Companion Star in X1822-371. *arXiv.org*, (2):1041–1048, March 2003.

J Casares, D Steeghs, R I Hynes, P A Charles, R Cornelisse, and K O’Brien. Bowen Fluorescence from Companion Stars in X-ray Binaries. *arXiv.org*, February 2004.

Jorge Casares. A FWHM-K2 correlation in Black-Hole transients. *arXiv.org*, (1):80, June 2015.

Ed Churchwell, Brian L Babler, Marilyn R Meade, Barbara A Whitney, Robert Benjamin, Remy Indebetouw, Claudia Cyganowski, Thomas P Robitaille, Matthew Povich, Christer Watson, and Steve Bracker. The Spitzer/GLIMPSE Surveys: A New View of the Milky Way. *Publications of the Astronomical Society of Pacific*, 121(8):213–, March 2009.

Deonizio Cieslinski, Marcos P Diaz, Andrew J Drake, and Kem H Cook. Discovery of New Eruptive Cataclysmic Variables Using the MACHO Database. *The Publications of the Astronomical Society of the Pacific*, 116(8):610–621, July 2004.

Gaia Collaboration, A G A Brown, A Vallenari, T Prusti, J H J de Bruijne, F Mignard, R Drimmel, C Babusiaux, C A L Bailer-Jones, U Bastian, M Biermann, D W Evans, L Eyer, F Jansen, C Jordi, D Katz, S A

Klioner, U Lammers, L Lindegren, X Luri, W O'Mullane, C Panem, D Pourbaix, S Randich, P Sartoretti, H I Siddiqui, C Soubiran, V Valette, F van Leeuwen, N A Walton, C Aerts, F Arenou, M Cropper, E Høg, M G Lattanzi, E K Grebel, A D Holland, C Huc, X Passot, M Perryman, L Bramante, C Cacciari, J Castañeda, L Chaoul, N Cheek, F De Angeli, C Fabricius, R Guerra, J Hernández, A Jean-Antoine-Piccolo, E Masana, R Messineo, N Mowlavi, K Nienartowicz, D Ordóñez-Blanco, P Panuzzo, J Portell, P J Richards, M Riello, G M Seabroke, P Tanga, F Thévenin, J Torra, S G Els, G Gracia-Abril, G Comoretto, M Garcia-Reinaldos, T Lock, E Mercier, M Altmann, R Andrae, T L Astraatmadja, I Bellas-Velidis, K Benson, J Berthier, R Blomme, G Busso, B Carry, A Cellino, G Clementini, S Cowell, O Creevey, J Cuypers, M Davidson, J De Ridder, A de Torres, L Delchambre, A Dell'Oro, C Ducourant, Y Frémat, M García-Torres, E Gosset, J L Halbwachs, N C Hambly, D L Harrison, M Hauser, D Hestroffer, S T Hodgkin, H E Huckle, A Hutton, G Jasniewicz, S Jordan, M Kontizas, A J Korn, A C Lanzafame, M Manteiga, A Moitinho, K Muinonen, J Osinde, E Pancino, T Pauwels, J M Petit, A Recio-Blanco, A C Robin, L M Sarro, C Siopis, M Smith, K W Smith, A Sozzetti, W Thuillot, W van Reeven, Y Viala, U Abbas, A Abreu Aramburu, S Accart, J J Aguado, P M Allan, W Allasia, G Altavilla, M A Álvarez, J Alves, R I Anderson, A H Andrei, E Anglada Varela, E Antiche, T Antoja, S Antón, B Arcay, N Bach, S G Baker, L Balaguer-Núñez, C Barache, C Barata, A Barbier, F Barblan, D Barrado y Navascués, M Barros, M A Barstow, U Becciani, M Bellazzini, A Bello García, V Belokurov, P Bendjoya, A Berihuete, L Bianchi, O Bienaymé, F Billebaud, N Blagorodnova, S Blanco-Cuaresma, T Boch, A Bombrun, R Borrachero, S Bouquillon, G Bourda, H Bouy, A Bragaglia, M A Breddels, N Brouillet, T Brüsemeister, B Bucciarelli, P Burgess, R Burgon, A Burlacu, D Bucsonero, R Buzzi, E Caffau, J Cambras, H Campbell, R Cancelliere, T Cantat-Gaudin, T Carlucci, J M Carrasco, M Castellani, P Charlot, J Charnas,

A Chiavassa, M Clotet, G Cocozza, R S Collins, G Costigan, F Crifo, N J G Cross, M Crosta, C Crowley, C Dafonte, Y Damerdji, A Dapergolas, P David, M David, P De Cat, F de Felice, P de Laverny, F De Luise, R De March, D de Martino, R de Souza, J Debosscher, E del Pozo, M Delbo, A Delgado, H E Delgado, P Di Matteo, S Diakite, E Distefano, C Dolding, S Dos Anjos, P Drazinos, J Duran, Y Dzigan, B Edvardsson, H Enke, N W Evans, G Eynard Bontemps, C Fabre, M Fabrizio, S Faigler, A J Falcão, M Farràs Casas, L Federici, G Fedorets, J Fernández-Hernández, P Fernique, A Fienga, F Figueras, F Filippi, K Findeisen, A Fonti, M Fouesneau, E Fraile, M Fraser, J Fuchs, M Gai, S Galleti, L Galluccio, D Garabato, F García-Sedano, A Garofalo, N Garralda, P Gavras, J Gerssen, R Geyer, G Gilmore, S Girona, G Giuffrida, M Gomes, A González-Marcos, J González-Núñez, J J González-Vidal, M Granvik, A Guerrier, P Guillout, J Guiraud, A Gúrpide, R Gutiérrez-Sánchez, Guy, L. P., R Haigron, D Hatzidimitriou, M Haywood, U Heiter, A Helmi, D Hobbs, W Hofmann, B Holl, G Holland, J A S Hunt, A Hypki, V Icardi, M Irwin, G Jevardat de Fombelle, P Jofré, P G Jonker, A Jorissen, F Julbe, A Karampelas, A Kochoska, R Kohley, K Kolenberg, and ... Kontizas. Gaia Data Release 1. Summary of the astrometric, photometric, and survey properties. *Astronomy & Astrophysics*, 595:A2, November 2016.

Arthur N Cox. Allen's astrophysical quantities. *Allen's astrophysical quantities*, 2000.

J E Drew, E Gonzalez-Solares, R Greimel, M J Irwin, A Küpcü Yoldas, J Lewis, G Barentsen, J Eisloffel, H J Farnhill, W E Martin, J R Walsh, N A Walton, M Mohr-Smith, R Raddi, S E Sale, N J Wright, P Groot, M J Barlow, R L M Corradi, J J Drake, J Fabregat, D J Frew, B T Gänsicke, C Knigge, A Mampaso, R A H Morris, T Naylor, Q A Parker, S Phillipps, C Ruhland, D Steeghs, Y C Unruh, J S Vink, R Wesson, and A A Zijlstra. The VST Photo-

tometric H α Survey of the Southern Galactic Plane and Bulge (VPHAS+). *Monthly Notices of the Royal Astronomical Society*, 440(3):2036–3058, May 2014.

J A Eaton and D S Hall. Starspots as the cause of the intrinsic light variations in RS Canum Venaticorum type stars. *Astrophysical Journal*, 227:907–922, February 1979.

K Ebisawa, M Tsujimoto, A Paizis, K Hamaguchi, A Bamba, R Cutri, H Kaneda, Y Maeda, G Sato, A Senda, M Ueno, S Yamauchi, V Beckmann, T J L Courvoisier, P Dubath, and E Nishihara. Chandra Deep X-Ray Observation of a Typical Galactic Plane Region and Near-Infrared Identification. *The Astrophysical Journal*, 635(1):214–242, December 2005.

Ian N Evans, Francis A Primini, Kenny J Glotfelty, Craig S Anderson, Nina R Bonaventura, Judy C Chen, John E Davis, Stephen M Doe, Janet D Evans, Giuseppina Fabbiano, Elizabeth C Galle, Danny G II Gibbs, John D Grier, Roger M Hain, Diane M Hall, Peter N Harbo, Xiangqun Helen He, John C Houck, Margarita Karovska, Vinay L Kashyap, Jennifer Lauer, Michael L McCollough, Jonathan C McDowell, Joseph B Miller, Arik W Mitschang, Douglas L Morgan, Amy E Mossman, Joy S Nichols, Michael A Nowak, David A Plummer, Brian L Refsdal, Arnold H Rots, Aneta Siemiginowska, Beth A Sundheim, Michael S Tibbetts, David W Van Stone, Sherry L Winkelman, and Panagoula Zografou. The Chandra Source Catalog. *The Astrophysical Journal Supplement*, 189(1):37–82, July 2010.

Daniel Foreman-Mackey. corner.py: Scatterplot matrices in Python. *The Journal of Open Source Software*, 2016(2), June 2016.

Daniel Foreman-Mackey, David W Hogg, Dustin Lang, and Jonathan Goodman. emcee: The MCMC Hammer. *Publications of the Astronomical Society of Pacific*, 125(9):306–, March 2013.

N Gehrels. Confidence limits for small numbers of events in astrophysical data. *Astrophysical Journal*, 303:336–346, April 1986.

Gregory M Green, Edward F Schlafly, Douglas P Finkbeiner, Hans-Walter Rix, Nicolas Martin, William Burgett, Peter W Draper, Heather Flewelling, Klaus Hodapp, Nicholas Kaiser, Rolf Peter Kudritzki, Eugene Magnier, Nigel Metcalfe, Paul Price, John Tonry, and Richard Wainscoat. A Three-dimensional Map of Milky Way Dust. *The Astrophysical Journal*, 810(1):25, September 2015.

S Greiss, D Steeghs, P G Jonker, M A P Torres, T J Maccarone, R I Hynes, C T Britt, G Nelemans, and B T Gaensicke. Near-infrared counterparts to the Galactic Bulge Survey X-ray source population. *arXiv.org*, (4):2839–2852, December 2013.

J E Grindlay, J Hong, P Zhao, S Laycock, M van den Berg, X Koenig, E M Schlegel, H N Cohn, P M Lugger, and A B Rogel. Chandra Multiwavelength Plane (ChaMPlane) Survey: An Introduction. *The Astrophysical Journal*, 635(2):920–930, December 2005.

Manuel Güdel. X-ray astronomy of stellar coronae. *The Astronomy and Astrophysics Review*, 12(2):71–237, September 2004.

J E Gunn and L L Stryker. Stellar spectrophotometric atlas, wavelengths from 3130 to 10800 Å. *Astrophysical Journal Supplement Series (ISSN 0067-0049)*, 52:121–153, June 1983.

Jeffrey C Hall. Stellar Chromospheric Activity. *Living Reviews in Solar Physics*, 5(1):2, 2008.

A D P Hands, R S Warwick, M G Watson, and D J Helfand. X-ray source populations in the Galactic plane. *Monthly Notices of the Royal Astronomical Society*, 351(1):31–56, June 2004.

M K Harrop-Allin, M Cropper, P J Hakala, C Hellier, and T Ramseyer. Indirect imaging of the accretion stream in eclipsing polars - II. HU Aquarii. *Monthly Notices*, 308(3):807–817, September 1999.

Arne A Henden, D L Welch, D Terrell, and S E Levine. The AAVSO Photometric All-Sky Survey (APASS). *American Astronomical Society*, 214:407.02–, May 2009.

E Høg, C Fabricius, V V Makarov, S Urban, T Corbin, G Wycoff, U Bastian, P Schekendiek, and A Wicenec. The Tycho-2 catalogue of the 2.5 million brightest stars. *Astronomy & Astrophysics*, 355:L27–L30, March 2000.

R K Honeycutt. Similarities between Stunted Outbursts in Nova-like Cataclysmic Variables and Outbursts in Ordinary Dwarf Novae. *The Publications of the Astronomical Society of the Pacific*, 113(7):473–481, April 2001.

M Hunsch, J H M M Schmitt, and W Voges. The ROSAT all-sky survey catalogue of optically bright late-type giants and supergiants. *Astronomy and Astrophysics Supplement*, 127(2):251–255, January 1998a.

Matthias Hunsch, Jurgen H M M Schmitt, Klaus-Peter Schroder, and Franz-Josef Zickgraf. On the X-ray emission from M-type giants. *Astronomy & Astrophysics*, 330:225–231, February 1998b.

Robert I Hynes, N J Wright, T J Maccarone, P G Jonker, S Greiss, D Steeghs, M A P Torres, C T Britt, and G Nelemans. IDENTIFICATION OF GALACTIC BULGE SURVEY X-RAY SOURCES WITH TYCHO-2STARS. *The Astrophysical Journal*, 761(2):162–22, December 2012.

Robert I Hynes, M A P Torres, C O Heinke, T J Maccarone, V J Mikles, C T Britt, C Knigge, S Greiss, P G Jonker, D Steeghs, G Nelemans, R M Bandyopadhyay, and C B Johnson. CXOGBS J173620.2-293338: A Candi-

date Symbiotic X-Ray Binary Associated with a Bulge Carbon Star. *The Astrophysical Journal*, 780(1):11, January 2014.

N Ivanova. Common Envelope: On the Mass and the Fate of the Remnant. *The Astrophysical Journal*, 730(2):76, April 2011.

N Ivanova, S Justham, X Chen, O De Marco, C L Fryer, E Gaburov, H Ge, E Glebbeek, Z Han, X D Li, G Lu, T Marsh, P Podsiadlowski, A Potter, N Soker, R Taam, T M Tauris, E P J van den Heuvel, and R F Webbink. Common envelope evolution: where we stand and how we can move forward. *The Astronomy and Astrophysics Review*, 21(1):59, February 2013.

P G Jonker, C G Bassa, G Nelemans, D Steeghs, M A P Torres, T J Maccarone, R I Hynes, S Greiss, J Clem, A Dieball, V J Mikles, C T Britt, L Gossen, A C Collazzi, R Wijnands, J J M In't Zand, M Méndez, N Rea, E Kuulkers, E M Ratti, L M van Haaften, C Heinke, F Özel, P J Groot, and F Verbunt. The Galactic Bulge Survey: Outline and X-ray Observations. *The Astrophysical Journal Supplement*, 194(2):18, June 2011.

Peter G Jonker, Manuel A P Torres, Robert I Hynes, Thomas J Maccarone, Danny Steeghs, Sandra Greiss, Christopher T Britt, Jianfeng Wu, Christopher B Johnson, Gijs Nelemans, and Craig Heinke. THE GALACTIC BULGE SURVEY: COMPLETION OF THE X-RAY SURVEY OBSERVATIONS . *The Astrophysical Journal Supplement*, 210(2):18, February 2014.

S J Kenyon and R F Webbink. The nature of symbiotic stars. *Astrophysical Journal*, 279:252–283, April 1984.

G Knevitt, G A Wynn, S Vaughan, and M G Watson. Black holes in short period X-ray binaries and the transition to radiatively inefficient accretion. *Monthly Notices of the Royal Astronomical Society*, 437(4):3087–3102, February 2014.

Xavier Koenig, Jonathan E Grindlay, Maureen van den Berg, Silas Laycock, Ping Zhao, JaeSub Hong, and Eric M Schlegel. Investigating ChaMPlane X-Ray Sources in the Galactic Bulge with Magellan LDSS2 Spectra. *The Astrophysical Journal*, 685(1):463–477, September 2008.

K Kuijken. OmegaCAM: ESO’s Newest Imager. *The Messenger*, 146:8–11, December 2011.

Arlo U Landolt. Broadband UBVRI photometry of the Baldwin-Stone Southern Hemisphere spectrophotometric standards. *Astronomical Journal (ISSN 0004-6256)*, 104:372–376, July 1992.

C H Lee, G E Brown, and R A M J Wijers. Discovery of a Black Hole Mass-Period Correlation in Soft X-Ray Transients and Its Implication for Gamma-Ray Burst and Hypernova Mechanisms. *The Astrophysical Journal*, 575(2):996–1006, August 2002.

Walter H G Lewin and Michiel van der Klis. Compact Stellar X-ray Sources. *Compact stellar X-ray sources. Edited by Walter Lewin & Michiel van der Klis. Cambridge Astrophysics Series*, April 2006.

Jing Li, Martin C Smith, Jing Zhong, Jinliang Hou, Jeffrey L Carlin, Heidi Jo Newberg, Chao Liu, Li Chen, Linlin Li, Zhengyi Shao, Emma Small, and Hao Tian. SELECTING M GIANTS WITH INFRARED PHOTOMETRY: DISTANCES, METALLICITIES, AND THE SAGITTARIUS STREAM. *The Astrophysical Journal*, 823(1):59, May 2016.

P L Lim, R I Diaz, and V Laidler. PySynphot User’s Guide. pages 1–174, 2015.

J L Linsky, W McClintock, R M Robertson, and S P Worden. Stellar model chromospheres. X - High-resolution, absolute flux profiles of the CA II H and

K lines in stars of spectral types F0-M2. *Astrophysical Journal Supplement Series*, 41:47–74, September 1979.

Q Z Liu, J van Paradijs, and E P J van den Heuvel. A catalogue of low-mass X-ray binaries. *Astronomy & Astrophysics*, 368(3):1021–1054, March 2001.

P W Lucas, M G Hoare, A Longmore, A C Schröder, C J Davis, A Adamson, R M Bandyopadhyay, R de Grijs, M Smith, A Gosling, S Mitchison, A Gáspár, M Coe, M Tamura, Q Parker, M Irwin, N Hambly, J Bryant, R S Collins, N Cross, D W Evans, E Gonzalez-Solares, S Hodgkin, J Lewis, M Read, M Riello, E T W Sutorius, A Lawrence, J E Drew, S Dye, and M A Thompson. The UKIDSS Galactic Plane Survey. *Monthly Notices of the Royal Astronomical Society*, 391(1):136–163, November 2008.

G J M Luna, J L Sokoloski, K Mukai, and T Nelson. Symbiotic stars in X-rays. *Astronomy & Astrophysics*, 559:A6, November 2013.

Tommaso Maccacaro, Isabella M Gioia, Anna Wolter, Giovanni Zamorani, and John T Stocke. The X-ray spectra of the extragalactic sources in the Einstein extended medium sensitivity survey. *Astrophysical Journal*, 326:680–690, March 1988.

Thomas J Maccarone, Manuel A P Torres, Christopher T Britt, Sandra Greiss, Robert I Hynes, Peter G Jonker, Danny Steeghs, Rudy Wijnands, and Gijs Nelemans. Radio sources in the Chandra Galactic Bulge Survey. *Monthly Notices of the Royal Astronomical Society*, 426(4):3057–3069, November 2012.

D Christopher Martin, James Fanson, David Schiminovich, Patrick Morrissey, Peter G Friedman, Tom A Barlow, Tim Conrow, Robert Grange, Patrick N Jelinsky, Bruno Milliard, Oswald H W Siegmund, Luciana Bianchi, Yong-Ik Byun, Jose Donas, Karl Forster, Timothy M Heckman, Young-Wook Lee, Barry F Madore, Roger F Malina, Susan G Neff, R Michael Rich, Todd Small, Frank Surber, Alex S Szalay, Barry Welsh, and Ted K Wyder. The Galaxy

Evolution Explorer: A Space Ultraviolet Survey Mission. *The Astrophysical Journal*, 619(1):L1–L6, January 2005.

Chase Million, Scott W Fleming, Bernie Shiao, Mark Seibert, Parke Loyd, Michael Tucker, Myron Smith, Randy Thompson, and Richard L White. gPhoton: The GALEX Photon Data Archive. *The Astrophysical Journal*, 833(2):292, December 2016.

D Minniti, P W Lucas, J P Emerson, R K Saito, M Hempel, P Pietrukowicz, A V Ahumada, M V Alonso, J Alonso-Garcia, J I Arias, R M Bandyopadhyay, R H Barbá, B Barbuy, L R Bedin, E Bica, J Borissova, L Bronfman, G Carraro, M Catelan, J J Clariá, N Cross, R de Grijs, I Dékány, J E Drew, C Fariña, C Feinstein, E Fernández Lajús, R C Gamen, D Geisler, W Gieren, B Goldman, O A Gonzalez, G Gunthardt, S Gurovich, N C Hambley, M J Irwin, V D Ivanov, A Jordán, E Kerins, K Kinemuchi, R Kurtev, M López-Corredoira, T Maccarone, N Masetti, D Merlo, M Messineo, I F Mirabel, L Monaco, L Morelli, N Padilla, T Palma, M C Parisi, G Pignata, M Rejkuba, A Roman-Lopes, S E Sale, M R Schreiber, A C Schröder, M Smith, M Soto, M Tamura, C Tappert, M A Thompson, I Toledo, M Zoccali, and G Pietrzynski. VISTA Variables in the Via Lactea (VVV): The public ESO near-IR variability survey of the Milky Way. *New Astronomy*, 15(5):433–443, July 2010.

Patrick Morrissey, Tim Conrow, Tom A Barlow, Todd Small, Mark Seibert, Ted K Wyder, Tamas Budavari, Stephane Arnouts, Peter G Friedman, Karl Forster, D Christopher Martin, Susan G Neff, David Schiminovich, Luciana Bianchi, Jose Donas, Timothy M Heckman, Young-Wook Lee, Barry F Madore, Bruno Milliard, R Michael Rich, Alex S Szalay, Barry Y Welsh, and Sukyoung K Yi. The Calibration and Data Products of the Galaxy Evolution Explorer. *arXiv.org*, page arXiv:0706.0755, June 2007.

C Motch, R Warwick, M S Cropper, F Carrera, P Guillout, F X Pineau,

M W Pakull, S Rosen, A Schwope, J Tedds, N Webb, I Negueruela, and M G Watson. The X-ray source content of the XMM-Newton Galactic plane survey. *Astronomy & Astrophysics*, 523:A92, November 2010.

P Mróz, A Udalski, R Poleski, P Pietrukowicz, M K Szymanski, I Soszynski, Ł Wyrzykowski, K Ulaczyk, S Kozłowski, and J Skowron. One Thousand New Dwarf Novae from the OGLE Survey. *Acta Astronomica*, 65:313–328, December 2015.

K Mukai, G J M Luna, G Cusumano, A Segreto, U Munari, J L Sokoloski, A B Lucy, T Nelson, and N E Nuñez. SU Lyncis, a hard X-ray bright M giant: clues point to a large hidden population of symbiotic stars. *Monthly Notices of the Royal Astronomical Society: Letters*, 461(1):L1–L5, September 2016.

R W Noyes, N O Weiss, and A H Vaughan. The relation between stellar rotation rate and activity cycle periods. *Astrophysical Journal*, 287:769–773, December 1984.

G Pace and L Pasquini. The age-activity-rotation relationship in solar-type stars. *Astronomy & Astrophysics*, 426(3):1021–1034, October 2004.

Brian M Patten and Theodore Simon. The Evolution of Rotation and Activity in Young Open Clusters: IC 2391. *The Astrophysical Journal Supplement Series*, 106:489, September 1996.

J Patterson, D Q Lamb, G Fabbiano, J C Raymond, K Beuermann, J Swank, and N E White. VV Puppis - The soft X-ray machine. *The Astrophysical Journal*, 279:785–797, April 1984.

K Pavlovskii, N Ivanova, K Belczynski, and K X Van. Stability of mass transfer from massive giants: double black hole binary formation and ultraluminous X-ray sources. *Monthly Notices of the Royal Astronomical Society*, 465(2):2092–2100, February 2017.

A J Pickles. VizieR Online Data Catalog: A Stellar Spectral Flux Library: 1150 - 25000 Å (Pickles 1998). *VizieR On-line Data Catalog*, 611, September 1998.

N Pizzolato, A Maggio, G Micela, S Sciortino, and P Ventura. The stellar activity-rotation relationship revisited: Dependence of saturated and non-saturated X-ray emission regimes on stellar mass for late-type dwarfs. *Astronomy & Astrophysics*, 397(1):147–157, January 2003.

G Pojmanski. The All Sky Automated Survey. Catalog of Variable Stars. I. 0 h - 6 hQuarter of the Southern Hemisphere. *Acta Astronomica*, 52:397–427, December 2002.

Francis A Primini, John C Houck, John E Davis, Michael A Nowak, Ian N Evans, Kenny J Glotfelty, Craig S Anderson, Nina R Bonaventura, Judy C Chen, Stephen M Doe, Janet D Evans, Giuseppina Fabbiano, Elizabeth C Galle, Danny G Gibbs, John D Grier, Roger M Hain, Diane M Hall, Peter N Harbo, Xiangqun Helen He, Margarita Karovska, Vinay L Kashyap, Jennifer Lauer, Michael L McCollough, Jonathan C McDowell, Joseph B Miller, Arik W Mitschang, Douglas L Morgan, Amy E Mossman, Joy S Nichols, David A Plummer, Brian L Refsdal, Arnold H Rots, Aneta Siemiginowska, Beth A Sundheim, Michael S Tibbetts, David W Van Stone, Sherry L Winkelman, and Panagoula Zografou. Statistical Characterization of the Chandra Source Catalog. *The Astrophysical Journal Supplement*, 194(2):37, June 2011.

Charles F Prosser, Sofia Randich, Joh R Stauffer, J H M M Schmitt, and Theodore Simon. ROSAT Pointed Observations of the Alpha Persei Cluster. *The Astronomical Journal*, 112:1570, October 1996.

E M Ratti, T F J van Grunsven, P G Jonker, C T Britt, R I Hynes, D Steeghs, S Greiss, M A P Torres, T J Maccarone, P J Groot, C Knigge, L Gossen,

V Mikles, V A Villar, and A C Collazzi. CXOGBS J174444.7-260330: a new long orbital period cataclysmic variable in a low state. *Monthly Notices of the Royal Astronomical Society*, 428(4):3543–3550, February 2013.

D Reimers, M Hunsch, F Toussaint, and J H M M Schmitt. ROSAT observations of hybrid stars. *Cool stars; stellar systems; and the sun : 9 : Astronomical Society of the Pacific Conference Series*, 109:537–, 1996.

Mikhail G Revnivtsev, Ivan Yu Zolotukhin, and Alexander V Meshcheryakov. Period-luminosity relation for persistent low-mass X-ray binaries in the near-infrared. *Monthly Notices of the Royal Astronomical Society*, 421(4):2846–2853, April 2012.

H Ritter and U Kolb. Catalogue of cataclysmic binaries, low-mass X-ray binaries and related objects (Seventh edition). *Astronomy & Astrophysics*, 404(1):301–303, May 2003.

Peter W A Roming, Thomas E Kennedy, Keith O Mason, John A Nousek, Lindy Ahr, Richard E Bingham, Patrick S Broos, Mary J Carter, Barry K Hancock, Howard E Huckle, S D Hunsberger, Hajime Kawakami, Ronnie Killough, T Scott Koch, Michael K McLellan, Kelly Smith, Philip J Smith, Juan Carlos Soto, Patricia T Boyd, Alice A Breeveld, Stephen T Holland, Mariya Ivanushkina, Michael S Pryzby, Martin D Still, and Joseph Stock. The Swift Ultra-Violet/Optical Telescope. *Space Science Reviews*, 120(3):95–142, October 2005.

J Sahade, G E McCluskey, and Yoji Kondo. The Realm of Interacting Binary Stars. *The Realm of Interacting Binary Stars*, 177, January 1993.

D Mata Sánchez, T Muñoz-Darias, J Casares, D Steeghs, C Ramos Almeida, and J A Acosta Pulido. Mass constraints to Sco X-1 from Bowen fluorescence and deep near-infrared spectroscopy. *arXiv.org*, (1):L1–L5, January 2015.

S Sazonov, M Revnivtsev, M Gilfanov, E Churazov, and R Sunyaev. X-ray luminosity function of faint point sources in the Milky Way. *Astronomy & Astrophysics*, 450(1):117–128, April 2006.

J H M M Schmitt. Coronae on solar-like stars. *Astronomy & Astrophysics*, 318:215–230, February 1997.

T Shahbaz, R P Fender, C A Watson, and K O'Brien. The First Polarimetric Signatures of Infrared Jets in X-Ray Binaries. *The Astrophysical Journal*, 672(1):510–515, January 2008.

Edward M Sion and Sumner G Starrfield. Evolutionary sequences of very hot, low-mass, accreting white dwarfs with application to symbiotic variables and ultrasoft/supersoft low-luminosity x-ray sources. *Astrophysical Journal*, 421:261–268, January 1994.

M F Skrutskie, R M Cutri, R Stiening, M D Weinberg, S Schneider, J M Carpenter, C Beichman, R Capps, T Chester, J Elias, J Huchra, J Liebert, C Lonsdale, D G Monet, S Price, P Seitzer, T Jarrett, J D Kirkpatrick, J E Gizis, E Howard, T Evans, J Fowler, L Fullmer, R Hurt, R Light, E L Kopan, K A Marsh, H L McCallon, R Tam, S Van Dyk, and S Wheelock. The Two Micron All Sky Survey (2MASS). *The Astronomical Journal*, 131(2):1163–1183, February 2006.

Myron A Smith, Luciana Bianchi, and Bernard Shiao. Interesting Features in the Combined GALEX and Sloan Color Diagrams of Solar-like Galactic Populations. *The Astronomical Journal*, 147(6):159, June 2014.

David R Soderblom. The Ages of Stars. *Annual Review of Astronomy and Astrophysics*, 48(1):581–629, August 2010.

J L Sokoloski. Symbiotic Stars as Laboratories for the Study of Accretion

and Jets: A Call for Optical Monitoring. *The Journal of the American Association of Variable Star Observers*, 31:89–102, December 2003.

M Soto, R Barbá, G Gunthardt, D Minniti, P Lucas, D Majaess, M Irwin, J P Emerson, E Gonzalez-Solares, M Hempel, R K Saito, S Gurovich, A Roman-Lopes, C Moni-Bidin, M V Santucho, J Borissova, R Kurtev, I Toledo, D Geisler, M Dominguez, and J C Beamin. Milky Way demographics with the VVV survey. II. Color transformations and near-infrared photometry for 136 million stars in the southern Galactic disk. *Astronomy & Astrophysics*, 552:A101, April 2013.

B Stelzer, A Marino, G Micela, J López-Santiago, and C Liefke. The UV and X-ray activity of the M dwarfs within 10 pc of the Sun. *Monthly Notices of the Royal Astronomical Society*, 431(3):2063–2079, May 2013.

B Stelzer, A Marino, G Micela, J López-Santiago, and C Liefke. Erratum: The UV and X-ray activity of the M dwarfs within 10 pc of the Sun. *Monthly Notices of the Royal Astronomical Society*, 442(1):343–346, July 2014.

K Stepień. Applicability of the Rossby number in activity-rotation relations for dwarfs and giants. *Astronomy and Astrophysics (ISSN 0004-6361)*, 292: 191–207, December 1994.

K G Strassmeier, D S Hall, M Zeilik, E Nelson, Z Eker, and F C Fekel. A catalog of chromospherically active binary stars. *Astronomy and Astrophysics Supplement Series (ISSN 0365-0138)*, 72:291–345, February 1988.

Paula Szkody, Anjum S Mukadam, Odette Toloza, Boris T Gänsicke, Zhibin Dai, Anna F Pala, Elizabeth O Waagen, Patrick Godon, and Edward M Sion. Hubble Space TelescopeUltraviolet Light Curves Reveal Interesting Properties of CC Sculptoris and RZ Leonis. *The Astronomical Journal*, 153 (3):123, March 2017.

Mark Taylor. TOPCAT – Tool for OPerations on Catalogues And Tables.
Starlink User Note 253, 253, 2013.

M A P Torres, P G Jonker, C T Britt, C B Johnson, R I Hynes, S Greiss, D Steeghs, T J Maccarone, F Özel, C Bassa, and G Nelemans. Identification of 23 accreting binaries in the Galactic Bulge Survey. *Monthly Notices of the Royal Astronomical Society*, 440(1):365–386, May 2014.

A Udalski, K Kowalczyk, I Soszynski, R Poleski, M K Szymanski, M Kubiak, G Pietrzynski, S Kozłowski, P Pietrukowicz, K Ulaczyk, J Skowron, and Ł Wyrzykowski. The Optical Gravitational Lensing Experiment. Optical Counterparts to the X-ray Sources in the Galactic Bulge. *Acta Astronomica*, 62:133–151, June 2012.

G S Vaiana, J P Cassinelli, G Fabbiano, R Giacconi, L Golub, P Gorenstein, B M Haisch, F R Jr Harnden, H M Johnson, J L Linsky, C W Maxson, R Mewe, R Rosner, F Seward, K Topka, and C Zwaan. Results from an extensive Einstein stellar survey. *Astrophysical Journal*, 245:163–182, April 1981.

G S Vaiana, A Maggio, G Micela, and S Sciortino. Coronal emission and stellar evolution. *Società Astronomica Italiana*, 63:545–562, 1992.

J van Paradijs and J E McClintock. Absolute visual magnitudes of low-mass X-ray binaries. *Astronomy & Astrophysics*, 290:133–136, October 1994.

J van Paradijs and N White. The Galactic Distribution of Low-Mass X-Ray Binaries. *Astrophysical Journal Letters v.447*, 447(1):L33–, July 1995.

O Vilhu and S M Rucinski. Rotation-Activity Connections in Main Sequence Binaries. *International Astronomical Union Colloquium*, 71:475–477, January 1983.

Osmi Vilhu. Coronal Loops in Binary Stars. *Physica Scripta*, 1984(T7):70–72, 1984.

F M Walter, W Cash, P A Charles, and C S Bowyer. X-rays from RS Canum Venaticorum systems - A HEAO 1 survey and the development of a coronal model. *Astrophysical Journal*, 236:212–218, February 1980.

R S Warwick. Low-luminosity X-ray sources and the Galactic ridge X-ray emission. *Monthly Notices of the Royal Astronomical Society*, 445(1):66–80, September 2014.

Martin C Weisskopf. The Chandra X-Ray Observatory: progress report and highlights. In Tadayuki Takahashi, Stephen S Murray, and Jan-Willem A den Herder, editors, *Space Telescopes and Instrumentation 2012: Ultraviolet to Gamma Ray. Proceedings of the SPIE*, page 84430Y. NASA Marshall Space Flight Ctr. (United States), SPIE, September 2012.

Andrew A West, Suzanne L Hawley, John J Bochanski, Kevin R Covey, I Neill Reid, Saurav Dhal, Eric J Hilton, and Michael Masuda. Constraining the Age-Activity Relation for Cool Stars: The Sloan Digital Sky Survey Data Release 5 Low-Mass Star Spectroscopic Sample. *The Astronomical Journal*, 135(3):785–795, March 2008.

T Wevers, S T Hodgkin, P G Jonker, C Bassa, G Nelemans, T van Grunsven, E A Gonzalez-Solares, M A P Torres, C Heinke, D Steeghs, T J Maccarone, C T Britt, R I Hynes, C Johnson, and Jianfeng Wu. The Chandra Galactic Bulge Survey: optical catalogue and point-source counterparts to X-ray sources. *Monthly Notices of the Royal Astronomical Society*, 458(4):4530–4546, June 2016a.

T Wevers, M A P Torres, P G Jonker, J D Wetuski, G Nelemans, D Steeghs, T J Maccarone, C Heinke, R I Hynes, A Udalski, Z Kostrzewska-Rutkowska, P J Groot, R Gazer, M K Szymanski, C T Britt, L Wyrzykowski, and R Poleski.

Discovery of a high state AM CVn binary in the Galactic Bulge Survey. *Monthly Notices of the Royal Astronomical Society: Letters*, 462(1):L106–L110, October 2016b.

T Wevers, M A P Torres, P G Jonker, G Nelemans, C Heinke, D Mata Sanchez, C B Johnson, R Gazer, D T H Steeghs, T J Maccarone, R I Hynes, J Casares, A Udalski, J Wetuski, C T Britt, Z Kostrzewska-Rutkowska, and L Wyrzykowski. Spectroscopic classification of X-ray sources in the Galactic Bulge Survey. *arXiv.org*, page arXiv:1705.10791, May 2017.

D T Wickramasinghe and Lilia Ferrario. Magnetism in Isolated and Binary White Dwarfs. *The Publications of the Astronomical Society of the Pacific*, 112(7):873–924, July 2000.

Kurtis A Williams, M Bolte, J Liebert, S Howell, and K H R Rubin. Spectroscopy of White Dwarfs in the Old Open Cluster M67. *American Astronomical Society*, 211:15.08–, December 2007.

Edward L Wright, Peter R M Eisenhardt, Amy K Mainzer, Michael E Ressler, Roc M Cutri, Thomas Jarrett, J Davy Kirkpatrick, Deborah Padgett, Robert S McMillan, Michael Skrutskie, S A Stanford, Martin Cohen, Russell G Walker, John C Mather, David Leisawitz, Thomas N III Gautier, Ian McLean, Dominic Benford, Carol J Lonsdale, Andrew Blain, Bryan Mendez, William R Irace, Valerie Duval, Fengchuan Liu, Don Royer, Ingolf Heinrichsen, Joan Howard, Mark Shannon, Martha Kendall, Amy L Walsh, Mark Larsen, Joel G Cardon, Scott Schick, Mark Schwalm, Mohamed Abid, Beth Fabinsky, Larry Naes, and Chao-Wei Tsai. The Wide-field Infrared Survey Explorer (WISE): Mission Description and Initial On-orbit Performance. *The Astronomical Journal*, 140(6):1868–1881, December 2010.

Nicholas J Wright, Jeremy J Drake, Eric E Mamajek, and Gregory W Henry.

The Stellar-activity-Rotation Relationship and the Evolution of Stellar Dynamos. *The Astrophysical Journal*, 743(1):48, December 2011.

Appendices

Appendix A

Full Chandra/Galex Dataset

GBS ID	N _X	R _X (")	RA _{glx}	DEC _{glx}	Δ r (")	m _{NUV} (AB)	F _X (erg/s/cm ²)	log(F _X /F _V)
CX4	238	0.91	264.879985	-29.164736	0.448	18.024 ± 0.056	2.523E-12	-2.26 ± 0.15
CX7	150	1	264.608699	-29.030336	1.455	16.627 ± 0.011	1.59E-12	-2.0 ± 0.11
CX8	138	0.89	263.784476	-29.499467	0.136	20.676 ± 0.127	1.463E-12	-
CX9	134	1.04	263.784988	-29.391103	0.424	15.114 ± 0.004	1.42E-12	-1.97 ± 0.1
CX10	122	1.53	264.121166	-29.174695	0.604	15.639 ± 0.005	1.293E-12	-2.46 ± 0.12
CX12	100	0.82	265.946997	-31.673658	0.682	15.402 ± 0.012	1.06E-12	-2.9 ± 0.11
CX14	93	1.06	266.598613	-31.583564	0.076	19.582 ± 0.159	9.858E-13	-1.6 ± 0.14
CX21	60	2.01	265.390778	-28.676401	1.37	20.74 ± 0.1	6.36E-13	-
CX22	57	0.91	266.474526	-31.25125	2.227	20.189 ± 0.12	6.042E-13	-1.73 ± 0.19
CX24	49	2.11	267.205991	-30.019137	1.509	21.239 ± 0.226	5.194E-13	-1.28 ± 0.18
CX26	48	2.26	266.388013	-30.982532	2.252	14.453 ± 0.003	5.088E-13	-3.4 ± 0.17
CX25	48	1.73	266.26155	-31.993009	0.159	17.386 ± 0.03	5.088E-13	-2.13 ± 0.17
CX27	47	1.49	264.220129	-28.811567	0.096	19.734 ± 0.165	4.982E-13	-2.25 ± 0.19
CX31	44	0.84	264.5149	-29.118524	1.102	14.171 ± 0.009	4.664E-13	-3.1 ± 0.18
CX32	42	1.13	265.270422	-28.250795	0.567	16.552 ± 0.029	4.452E-13	-2.62 ± 0.21
CX33	42	1.25	267.148504	-29.958356	2.037	12.257 ± 0.005	4.452E-13	-3.36 ± 0.19
CX36	37	2.18	264.474674	-28.399661	0.653	21.892 ± 0.522	3.922E-13	-1.85 ± 0.2

CX46	31	1.82	268.318463	-28.63751	2.931	19.135 ± 0.055	3.286E-13	-
CX59	27	1.05	266.252304	-26.207994	0.404	13.809 ± 0.008	2.862E-13	-
CX66	24	1.72	266.872098	-26.113916	0.712	20.933 ± 0.386	2.544E-13	-1.79 ± 0.25
CX71	24	3.58	264.955021	-27.906362	2.395	22.424 ± 0.328	2.544E-13	-
CX72	23	0.95	267.085285	-30.476451	1.449	14.609 ± 0.003	2.438E-13	-3.17 ± 0.28
CX77	23	3.27	264.159236	-28.995016	3.417	12.437 ± 0.001	2.438E-13	-
CX82	22	2.61	269.289781	-27.426055	1.181	19.111 ± 0.087	2.332E-13	-2.35 ± 0.35
CX93	20	1.33	266.186765	-26.057844	2.177	23.328 ± 0.466	2.12E-13	-
CX91	20	2.38	269.045881	-27.24049	1.786	14.344 ± 0.007	2.12E-13	-
CX90	20	3.6	266.376379	-25.924834	1.627	23.355 ± 0.473	2.12E-13	-1.81 ± 0.3
CX94	19	1.67	267.518305	-30.140514	1.124	17.191 ± 0.043	2.014E-13	-2.51 ± 0.31
CX95	19	1.6	263.589637	-30.161742	0.702	22.041 ± 0.24	2.014E-13	-1.6 ± 0.3
CX100	19	1.92	265.065157	-27.079123	0.652	19.445 ± 0.113	2.014E-13	-1.98 ± 0.3
CX104	18	1.67	269.389285	-27.385314	0.925	19.176 ± 0.04	1.908E-13	-
CX107	18	3.15	266.56563	-31.014711	0.844	21.706 ± 0.215	1.908E-13	-1.79 ± 0.33
CX114	17	2.74	265.424412	-28.556857	1.515	20.537 ± 0.28	1.802E-13	-2.08 ± 0.31
CX115	17	1.61	264.920153	-28.853329	0.255	14.001 ± 0.002	1.802E-13	-3.43 ± 0.31
CX117	17	2.03	265.173378	-27.634151	1.574	21.902 ± 0.534	1.802E-13	-
CX118	17	2.21	264.709079	-28.802424	1.004	22.876 ± 0.38	1.802E-13	-
CX137	15	4.22	268.971861	-28.276128	0.905	20.725 ± 0.167	1.59E-13	-
CX143	14	1.46	265.707061	-26.806462	0.399	22.209 ± 0.366	1.484E-13	-
CX147	14	2.56	263.232228	-30.1966	1.731	22.726 ± 0.363	1.484E-13	-
CX149	14	1.01	265.611583	-26.791919	0.735	20.08 ± 0.163	1.484E-13	-1.88 ± 0.36
CX159	13	5.66	268.802264	-27.616733	2.491	16.905 ± 0.007	1.378E-13	-2.67 ± 0.39
CX161	13	1.23	264.967673	-28.573608	0.344	23.481 ± 0.433	1.378E-13	-
CX167	13	1.94	264.48883	-27.870483	0.793	20.755 ± 0.096	1.378E-13	-2.34 ± 0.38
CX170	13	1.51	264.479624	-29.594784	1.276	20.116 ± 0.228	1.378E-13	-1.89 ± 0.37
CX173	12	1.79	266.962725	-30.365697	2.563	21.647 ± 0.265	1.272E-13	-1.76 ± 0.41
CX174	12	4.78	264.243154	-29.397697	1.359	19.045 ± 0.112	1.272E-13	-2.02 ± 0.39

CX178	12	3.27	263.91246	-30.171141	4.394	23.058 ± 0.323	1.272E-13	-
CX183	12	3.17	267.671182	-29.278521	2.238	12.168 ± 0.004	1.272E-13	-4.21 ± 0.39
CX185	12	1.5	263.865224	-29.753788	3.328	18.684 ± 0.025	1.272E-13	-
CX192	12	3.6	265.742472	-27.115648	0.946	22.163 ± 0.287	1.272E-13	-2.35 ± 0.39
CX205	11	5.17	267.321231	-30.597292	2.845	11.715 ± 0.001	1.166E-13	-4.93 ± 0.41
CX210	11	4.33	266.2966	-25.481554	3.353	23.647 ± 0.501	1.166E-13	-
CX215	11	2.79	262.94127	-30.177291	1.554	22.551 ± 0.347	1.166E-13	-1.75 ± 0.41
CX216	11	1.31	264.340525	-28.899311	0.578	22.611 ± 0.339	1.166E-13	-
CX221	10	2.71	269.147284	-28.007495	1.294	20.25 ± 0.269	1.06E-13	-
CX236	10	1.8	264.759769	-28.514467	0.675	23.061 ± 0.411	1.06E-13	-1.67 ± 0.46
CX237	10	5.25	264.5683	-29.660742	5.732	20.535 ± 0.299	1.06E-13	-1.83 ± 0.45
CX252	9	1.33	269.02358	-27.907066	0.446	18.759 ± 0.023	9.54E-14	-2.58 ± 0.48
CX253	9	2.06	268.614005	-27.792667	2.899	19.179 ± 0.038	9.54E-14	-
CX255	9	2.8	268.555654	-28.158709	1.154	17.583 ± 0.025	9.54E-14	-2.63 ± 0.47
CX256	9	2.19	268.450194	-28.688533	2.204	15.466 ± 0.007	9.54E-14	-4.51 ± 0.46
CX272	9	1.46	265.974145	-27.029116	0.577	16.472 ± 0.007	9.54E-14	-3.03 ± 0.47
CX275	9	5.43	265.521872	-26.845435	3.322	11.855 ± 0.004	9.54E-14	-4.41 ± 0.46
CX276	9	1.45	265.382723	-28.007079	1.471	20.87 ± 0.32	9.54E-14	-1.86 ± 0.48
CX284	9	2.63	264.10397	-28.418397	3.622	22.628 ± 0.343	9.54E-14	-
CX296	8	1.39	267.463336	-29.936683	1.43	15.943 ± 0.022	8.48E-14	-3.09 ± 0.53
CX304	8	2.82	269.008763	-27.656093	2.295	21.1 ± 0.293	8.48E-14	-
CX307	8	4.96	268.633564	-28.634072	2.306	17.799 ± 0.023	8.48E-14	-
CX315	8	5.36	266.608158	-25.57066	0.578	17.182 ± 0.053	8.48E-14	-2.72 ± 0.55
CX317	8	2.34	266.427996	-31.847579	3.596	23.507 ± 1.07	8.48E-14	-1.53 ± 0.51
CX322	8	1.46	266.028411	-27.440661	1.673	20.063 ± 0.23	8.48E-14	-2.02 ± 0.54
CX326	8	1.13	265.380528	-27.167204	2.761	21.321 ± 0.157	8.48E-14	-
CX331	8	1.72	264.097632	-29.375786	1.856	21.429 ± 0.423	8.48E-14	-
CX333	8	2.47	264.073016	-28.572102	2.108	13.78 ± 0.002	8.48E-14	-3.92 ± 0.5
CX337	8	5.93	263.863423	-29.513194	0.569	13.936 ± 0.009	8.48E-14	-3.37 ± 0.5

CX345	7	3.39	265.524066	-26.687938	3.866	22.768 ± 0.522	7.42E-14	-
CX351	7	1.23	268.959526	-28.118458	1.325	18.8 ± 0.06	7.42E-14	-2.45 ± 0.55
CX352	7	2.99	268.904477	-28.299869	0.847	16.417 ± 0.01	7.42E-14	-
CX355	7	4.13	268.396461	-29.166615	5.091	21.148 ± 0.329	7.42E-14	-
CX356	7	1.49	268.388479	-28.985605	2.749	20.567 ± 0.293	7.42E-14	-
CX361	7	5.88	267.781933	-29.677008	0.262	18.329 ± 0.033	7.42E-14	-
CX364	7	4.69	266.962324	-30.81888	0.834	20.672 ± 0.143	7.42E-14	-2.23 ± 0.56
CX365	7	1.66	266.902301	-25.973914	2.529	21.611 ± 0.276	7.42E-14	-
CX371	7	3.75	266.420474	-26.588854	0.526	18.331 ± 0.075	7.42E-14	-2.88 ± 0.55
CX378	7	4.5	265.614533	-27.33595	5.029	21.304 ± 0.497	7.42E-14	-
CX381	7	4.17	265.099652	-27.296301	4.211	21.909 ± 0.402	7.42E-14	-
CX387	7	4.41	264.27277	-29.413621	4.716	20.74 ± 0.418	7.42E-14	-
CX388	7	1.1	264.247887	-29.101394	2.921	16.512 ± 0.026	7.42E-14	-
CX396	7	4.96	263.546519	-29.458475	3.934	23.832 ± 1.681	7.42E-14	-
CX397	7	5.59	263.498061	-29.82983	0.51	19.976 ± 0.173	7.42E-14	-
CX398	7	1.52	263.438657	-29.53755	2.105	21.378 ± 0.424	7.42E-14	-
CX402	7	2.32	263.888411	-30.393741	0.704	15.057 ± 0.003	7.42E-14	-3.79 ± 0.56
CX403	6	1.64	268.276864	-29.091993	1.501	21.977 ± 0.466	6.36E-14	-
CX414	6	1.44	269.290987	-27.547054	1.057	22.493 ± 0.338	6.36E-14	-
CX415	6	1.6	269.124848	-27.137883	0.245	17.103 ± 0.027	6.36E-14	-2.56 ± 0.64
CX417	6	1.58	268.616152	-28.130233	1.993	15.256 ± 0.006	6.36E-14	-
CX418	6	2.17	268.576593	-28.678196	1.231	19.335 ± 0.067	6.36E-14	-
CX424	6	2.83	268.329249	-29.007922	2.658	20.348 ± 0.203	6.36E-14	-
CX426	6	1.26	268.150211	-29.327683	0.17	20.37 ± 0.2	6.36E-14	-
CX431	6	2.5	268.115445	-29.422817	1.214	21.191 ± 0.326	6.36E-14	-2.83 ± 0.66
CX434	6	3.53	267.794207	-29.021488	1.156	21.453 ± 0.434	6.36E-14	-
CX452	6	2.42	266.441079	-31.141076	0.458	17.839 ± 0.021	6.36E-14	-3.25 ± 0.62
CX454	6	2.39	266.354908	-26.652408	1.145	21.769 ± 0.234	6.36E-14	-2.26 ± 0.62
CX462	6	4.03	265.674562	-27.685176	4.74	22.802 ± 0.532	6.36E-14	-

CX466	6	3.89	265.404498	-28.243073	4.792	22.038 ± 0.383	6.36E-14	-
CX467	6	3.22	265.349962	-26.965326	1.5	14.851 ± 0.012	6.36E-14	-3.78 ± 0.62
CX469	6	3.81	265.194365	-28.64767	1.51	22.052 ± 0.256	6.36E-14	-1.93 ± 0.62
CX470	6	2.72	265.17787	-27.695638	1.296	21.795 ± 0.282	6.36E-14	-
CX485	6	2.32	264.328265	-28.490463	0.396	14.855 ± 0.003	6.36E-14	-3.63 ± 0.61
CX493	6	4.83	263.748128	-29.817556	3.038	21.796 ± 0.711	6.36E-14	-
CX495	6	2.66	263.698702	-29.587028	1.784	22.643 ± 0.651	6.36E-14	-
CX497	6	1.84	263.592864	-30.084866	2.752	21.992 ± 0.488	6.36E-14	-1.47 ± 0.6
CX502	6	5.65	268.099677	-28.401754	6.069	18.9 ± 0.041	6.36E-14	-
CX505	6	3.43	265.971838	-26.898072	0.973	22.785 ± 0.445	6.36E-14	-1.96 ± 0.61
CX506	6	1.4	265.192205	-28.029407	3.287	14.361 ± 0.01	6.36E-14	-4.02 ± 0.6
CX519	5	1.65	268.682271	-27.685403	1.477	21.625 ± 0.177	5.3E-14	-
CX524	5	3.96	268.580914	-28.614343	2.824	18.001 ± 0.046	5.3E-14	-3.74 ± 0.71
CX533	5	2.16	268.044333	-28.791317	3.562	19.037 ± 0.181	5.3E-14	-
CX549	5	1.59	266.982993	-30.286193	2.422	21.064 ± 0.417	5.3E-14	-
CX551	5	1.45	266.826059	-30.510148	1.622	22.723 ± 0.421	5.3E-14	-
CX554	5	4.37	266.648096	-30.804626	0.716	19.996 ± 0.076	5.3E-14	-2.72 ± 0.7
CX558	5	3.08	266.581744	-31.736517	0.108	18.743 ± 0.068	5.3E-14	-2.84 ± 0.7
CX574	5	6.38	266.252492	-26.11192	4.565	21.361 ± 0.407	5.3E-14	-
CX579	5	2.33	266.135398	-31.664567	0.998	21.303 ± 0.361	5.3E-14	-1.91 ± 0.72
CX584	5	2.37	266.002401	-25.733928	0.261	20.694 ± 0.077	5.3E-14	-2.49 ± 0.7
CX611	5	5.19	264.960228	-27.154768	2.296	20.848 ± 0.118	5.3E-14	-
CX622	5	1.73	264.226114	-29.876053	2.47	18.096 ± 0.064	5.3E-14	-
CX630	5	3.94	263.893585	-29.004975	2.025	18.517 ± 0.078	5.3E-14	-2.6 ± 0.7
CX632	5	3.52	263.475177	-29.398777	1.111	18.522 ± 0.085	5.3E-14	-3.98 ± 0.68
CX633	5	2.06	263.32806	-30.089508	0.567	22.228 ± 0.393	5.3E-14	-
CX637	5	4.81	263.285652	-29.95708	2.941	22.681 ± 0.361	5.3E-14	-1.99 ± 0.71
CX645	5	1.64	266.639173	-26.387221	0.457	22.566 ± 0.311	5.3E-14	-
CX646	5	2.4	263.775618	-29.353212	0.575	22.994 ± 0.466	5.3E-14	-1.82 ± 0.69

CX662	4	1.67	269.175691	-27.764842	0.951	19.31 ± 0.093	4.24E-14	-
CX666	4	2.34	269.007084	-27.746997	0.839	23.143 ± 0.724	4.24E-14	-
CX672	4	6.71	268.941081	-28.267858	2.672	21.912 ± 0.327	4.24E-14	-
CX673	4	3.08	268.868341	-28.393448	0.435	21.963 ± 0.348	4.24E-14	-
CX675	4	1.35	268.641476	-28.53884	1.026	20.281 ± 0.108	4.24E-14	-
CX680	4	3.09	268.550089	-28.655965	3.314	15.041 ± 0.006	4.24E-14	-3.49 ± 0.88
CX681	4	2.03	268.523706	-28.792387	0.856	20.356 ± 0.258	4.24E-14	-
CX698	4	4.08	268.08737	-29.074208	1.531	17.595 ± 0.048	4.24E-14	-3.43 ± 0.82
CX719	4	2.6	267.381778	-30.031096	1.104	15.355 ± 0.017	4.24E-14	-3.14 ± 0.83
CX716	4	1.18	267.46493	-30.301624	2.276	22.08 ± 0.403	4.24E-14	-
CX724	4	1.44	267.226437	-30.311024	1.541	20.108 ± 0.456	4.24E-14	-
CX728	4	3.15	267.050341	-30.408692	1.879	15.962 ± 0.005	4.24E-14	-3.04 ± 0.82
CX736	4	2.24	266.830063	-31.261052	2.846	18.799 ± 0.036	4.24E-14	-
CX738	4	2	266.732036	-30.485659	1.481	19.391 ± 0.048	4.24E-14	-2.28 ± 0.82
CX742	4	1.35	266.583037	-26.208344	1.476	22.402 ± 0.281	4.24E-14	-
CX751	4	1.74	266.502485	-30.93183	3.052	22.103 ± 0.523	4.24E-14	-
CX763	4	5.64	266.292552	-25.497784	1.614	20.533 ± 0.251	4.24E-14	-2.33 ± 0.82
CX768	4	2.86	266.157485	-31.236935	1.065	18.976 ± 0.074	4.24E-14	-
CX771	4	5.45	266.077118	-31.726259	0.891	17.285 ± 0.03	4.24E-14	-2.86 ± 0.81
CX783	4	1.92	265.741412	-26.209542	1.195	23.252 ± 0.456	4.24E-14	-
CX785	4	2.02	265.707513	-27.843876	2.282	12.537 ± 0.001	4.24E-14	-4.48 ± 0.8
CX789	4	4.73	265.58623	-28.104494	0.556	21.042 ± 0.112	4.24E-14	-2.14 ± 0.85
CX791	4	4.2	265.5594	-27.890351	1.937	19.725 ± 0.175	4.24E-14	-3.05 ± 0.81
CX796	4	1.56	265.364793	-27.97741	0.741	22.324 ± 0.302	4.24E-14	-
CX814	4	2.87	264.855014	-28.254805	3.372	19.266 ± 0.04	4.24E-14	-
CX839	4	3.65	264.151934	-29.071409	0.622	18.639 ± 0.08	4.24E-14	-2.7 ± 0.81
CX841	4	2.32	264.071753	-28.678503	1.178	17.261 ± 0.038	4.24E-14	-2.99 ± 0.8
CX843	4	3.65	264.024728	-30.304675	0.727	19.584 ± 0.184	4.24E-14	-2.27 ± 0.82
CX844	4	3.78	263.986695	-30.389939	4.313	21.292 ± 0.493	4.24E-14	-

CX849	4	1.9	263.871632	-30.347258	0.759	15.965 ± 0.005	4.24E-14	-2.96 ± 0.81
CX880	3	1.89	267.253658	-29.909112	0.1	19.141 ± 0.127	3.18E-14	-2.52 ± 0.98
CX886	3	6.57	266.283183	-27.193868	1.606	22.015 ± 0.357	3.18E-14	-
CX887	3	3.78	266.121077	-26.059014	4.239	21.218 ± 0.177	3.18E-14	-
CX901	3	2.86	269.213359	-27.397442	0.993	19.787 ± 0.129	3.18E-14	-2.56 ± 1.0
CX904	3	2.49	269.105846	-27.178673	0.588	18.718 ± 0.07	3.18E-14	-3.63 ± 1.01
CX912	3	2.89	269.016348	-27.476179	1.75	17.69 ± 0.035	3.18E-14	-2.77 ± 0.99
CX914	3	5.87	268.99797	-27.629187	1.018	20.034 ± 0.164	3.18E-14	-2.26 ± 0.98
CX938	3	2.35	268.466601	-28.748371	2.368	19.534 ± 0.081	3.18E-14	-
CX945	3	2.03	268.223016	-28.711993	0.674	18.802 ± 0.108	3.18E-14	-
CX951	3	1.65	268.09886	-28.945907	0.379	18.958 ± 0.104	3.18E-14	-2.87 ± 1.01
CX970	3	3.54	267.367123	-29.774745	0.629	19.731 ± 0.054	3.18E-14	-2.7 ± 0.99
CX974	3	3.35	267.323158	-29.614217	1.953	22.033 ± 0.372	3.18E-14	-2.59 ± 0.99
CX977	3	19.6	267.257919	-30.389794	18.923	21.084 ± 0.44	3.18E-14	-
CX991	3	1.89	266.880981	-30.677536	3.285	22.619 ± 0.535	3.18E-14	-
CX1001	3	5.7	266.644606	-30.574737	1.044	19.568 ± 0.05	3.18E-14	-2.74 ± 1.0
CX1007	3	1.26	266.579728	-25.797262	0.618	21.834 ± 0.528	3.18E-14	-1.94 ± 1.0
CX1018	3	1.6	266.474045	-31.719954	0.386	22.651 ± 0.395	3.18E-14	-
CX1026	3	2.63	266.388706	-31.549914	1.071	21.458 ± 0.303	3.18E-14	-
CX1029	3	3.96	266.341768	-26.015778	2.049	22.635 ± 0.531	3.18E-14	-
CX1031	3	3.27	266.267192	-25.540683	0.382	20.477 ± 0.077	3.18E-14	-3.5 ± 1.01
CX1034	3	2.68	266.256464	-26.538385	0.759	15.302 ± 0.004	3.18E-14	-3.48 ± 0.99
CX1039	3	2.72	266.200435	-31.624655	0.873	22.688 ± 0.411	3.18E-14	-1.88 ± 0.98
CX1042	3	4.36	266.15106	-26.294039	2.377	21.936 ± 0.348	3.18E-14	-
CX1048	3	1.4	266.056339	-25.770578	1.901	21.249 ± 0.577	3.18E-14	-
CX1059	3	3.01	265.909909	-31.75351	3.383	21.793 ± 0.49	3.18E-14	-
CX1087	3	2.95	265.418745	-27.61347	0.807	18.222 ± 0.018	3.18E-14	-3.83 ± 0.99
CX1092	3	3.22	265.289635	-26.784377	0.388	17.312 ± 0.037	3.18E-14	-3.8 ± 0.98
CX1113	3	3.95	265.04782	-28.036674	0.475	17.647 ± 0.046	3.18E-14	-3.39 ± 0.99

CX1117	3	2.57	264.995092	-27.425608	0.575	18.392 ± 0.074	3.18E-14	-2.95 ± 1.0
CX1132	3	1.31	264.770372	-29.134083	2.674	23.328 ± 0.383	3.18E-14	-
CX1133	3	1.74	264.751695	-29.156861	0.05	18.782 ± 0.022	3.18E-14	-2.66 ± 0.99
CX1136	3	3.57	264.735787	-28.591956	0.546	22.201 ± 0.264	3.18E-14	-2.14 ± 1.0
CX1155	3	3.66	264.379383	-29.407953	0.28	21.238 ± 0.397	3.18E-14	-2.26 ± 1.0
CX1200	3	1.75	263.804615	-29.673345	1.043	18.418 ± 0.085	3.18E-14	-2.74 ± 1.0
CX1210	3	2.13	263.58865	-30.304849	3.117	21.333 ± 0.555	3.18E-14	-
CX1214	3	2.58	263.44208	-30.324743	1.106	17.407 ± 0.01	3.18E-14	-3.04 ± 1.0
CX1217	3	2.47	263.370824	-29.524466	1.133	21.756 ± 0.24	3.18E-14	-2.07 ± 1.01
CX1219	3	2.88	263.320563	-30.344731	1.848	15.832 ± 0.004	3.18E-14	-3.67 ± 1.0
CX1225	3	2.84	263.029086	-30.135903	0.443	21.814 ± 0.47	3.18E-14	-1.9 ± 1.03
CX1229	3	1.94	267.986795	-28.696417	1.755	21.874 ± 0.314	3.18E-14	-
CXB4	70	0.95	263.567747	-30.760728	0.348	18.917 ± 0.072	7.42E-13	-1.7 ± 0.15
CXB5	66	0.96	263.036257	-30.474553	0.3	18.23 ± 0.035	6.996E-13	-2.63 ± 0.17
CXB8	65	1.63	268.633294	-29.473449	2.336	17.739 ± 0.04	6.89E-13	-
CXB10	53	1.05	269.635005	-27.878853	0.173	20.433 ± 0.196	5.618E-13	-
CXB12	36	1.41	268.138475	-29.662391	0.817	18.942 ± 0.106	3.816E-13	-2.59 ± 0.22
CXB14	33	2.54	268.486353	-29.019718	1.341	20.886 ± 0.331	3.498E-13	-
CXB25	21	3.34	267.949536	-30.179427	3.263	17.981 ± 0.042	2.226E-13	-2.8 ± 0.28
CXB35	16	3.61	269.395976	-27.615426	1.774	19.679 ± 0.14	1.696E-13	-1.68 ± 0.36
CXB34	16	5.57	266.870784	-32.244114	2.595	22.297 ± 0.478	1.696E-13	-
CXB45	14	1	268.280631	-29.565341	0.921	18.498 ± 0.086	1.484E-13	-
CXB56	11	2.69	266.727824	-25.744728	3.5	23.051 ± 0.384	1.166E-13	-
CXB58	11	2.37	268.583049	-29.637726	0.931	17.47 ± 0.03	1.166E-13	-
CXB59	11	4.81	268.483851	-29.474085	3.747	20.212 ± 0.39	1.166E-13	-
CXB62	11	1.87	267.512637	-30.492062	3.332	20.03 ± 0.117	1.166E-13	-
CXB66	10	1.54	267.983378	-29.85401	0.285	20.071 ± 0.099	1.06E-13	-2.6 ± 0.45
CXB76	10	3.69	263.415283	-30.594372	4.726	21.106 ± 0.217	1.06E-13	-
CXB80	9	5.31	269.488444	-27.828198	1.563	20.3 ± 0.114	9.54E-14	-2.01 ± 0.47

CXB84	9	1.05	268.912006	-28.944198	1.637	20.053 ± 0.18	9.54E-14	-
CXB87	9	4.77	268.249134	-29.671758	2.566	20.862 ± 0.276	9.54E-14	-1.99 ± 0.48
CXB91	9	1.85	266.820482	-25.726873	2.355	21.377 ± 0.393	9.54E-14	-2.62 ± 0.46
CXB93	9	1.67	266.552398	-32.103454	1.781	19.481 ± 0.082	9.54E-14	-3.43 ± 0.47
CXB112	8	2.45	263.273456	-30.586069	1.897	21.05 ± 0.32	8.48E-14	-2.52 ± 0.53
CXB114	7	1.9	269.405283	-27.162093	0.844	20.553 ± 0.219	7.42E-14	-2.65 ± 0.58
CXB116	7	1.54	269.28112	-27.147447	1.319	13.991 ± 0.006	7.42E-14	-3.67 ± 0.58
CXB123	7	1.86	268.342321	-29.399377	2.963	21.557 ± 0.415	7.42E-14	-
CXB128	7	3.35	266.714419	-25.779296	2.095	14.562 ± 0.002	7.42E-14	-3.83 ± 0.55
CXB130	7	2.21	262.784017	-30.34228	0.855	21.695 ± 0.367	7.42E-14	-
CXB131	7	3.4	269.093692	-28.451158	2.475	22.211 ± 0.396	7.42E-14	-
CXB136	6	2.15	269.383417	-27.727524	3.591	23 ± 0.442	6.36E-14	-
CXB139	6	2.15	269.17695	-28.4768	0.768	18.616 ± 0.039	6.36E-14	-
CXB146	6	5.39	268.570047	-29.427263	6.014	21.257 ± 0.602	6.36E-14	-
CXB151	6	3.44	268.084611	-29.99465	0.753	17.746 ± 0.024	6.36E-14	-3.07 ± 0.61
CXB161	6	3.18	263.739056	-30.728892	0.443	20.005 ± 0.052	6.36E-14	-2.83 ± 0.61
CXB164	6	2.32	267.462738	-31.03598	2.172	20.13 ± 0.11	6.36E-14	-2.0 ± 0.62
CXB167	5	2.75	269.548312	-27.609236	4.048	22.797 ± 0.385	5.3E-14	-
CXB176	5	3.89	268.9985	-28.862489	0.853	20.426 ± 0.126	5.3E-14	-
CXB181	5	2.47	268.730752	-29.202747	0.592	17.12 ± 0.023	5.3E-14	-3.95 ± 0.7
CXB186	5	5.14	268.541988	-29.430703	1.776	21.087 ± 0.296	5.3E-14	-
CXB194	5	1.35	267.493794	-30.720747	2.009	22.906 ± 0.462	5.3E-14	-
CXB200	5	9.15	263.464785	-30.841622	1.257	15.682 ± 0.012	5.3E-14	-3.11 ± 0.7
CXB202	5	4.15	263.306701	-30.412676	2.232	21.803 ± 0.436	5.3E-14	-
CXB206	5	5.27	262.906697	-30.399291	2.023	21.944 ± 0.361	5.3E-14	-2.48 ± 0.74
CXB208	5	5.14	268.422192	-29.922248	0.713	16.936 ± 0.012	5.3E-14	-
CXB211	5	6.9	265.871051	-32.231292	7.454	11.964 ± 0.003	5.3E-14	-4.59 ± 0.68
CXB223	4	2.56	269.134064	-28.714223	2.966	21.587 ± 0.362	4.24E-14	-
CXB224	4	3.11	269.085291	-28.665985	1.022	18.692 ± 0.04	4.24E-14	-

CXB225	4	5.73	269.079865	-28.47086	3.177	16.852 ± 0.013	4.24E-14	-3.62 ± 0.84
CXB226	4	5.08	269.061988	-28.963425	2.084	21.826 ± 0.415	4.24E-14	-
CXB228	4	3.16	269.029966	-28.541213	0.342	20.521 ± 0.133	4.24E-14	-
CXB231	4	4.81	268.920856	-29.123831	5.074	21.6 ± 0.458	4.24E-14	-
CXB233	4	3.17	268.839614	-28.572556	3.902	12.139 ± 0.002	4.24E-14	-3.94 ± 0.82
CXB249	4	3.11	268.123317	-29.669674	3.518	18.897 ± 0.097	4.24E-14	-2.42 ± 0.81
CXB284	4	2.97	266.022923	-32.121859	1.19	20.919 ± 0.261	4.24E-14	-
CXB287	4	3.83	263.390219	-30.533064	3.766	13.119 ± 0.003	4.24E-14	-4.23 ± 0.8
CXB290	4	1.85	262.910405	-30.496068	1.203	20.038 ± 0.14	4.24E-14	-2.46 ± 0.83
CXB293	3	2.05	268.710732	-29.336797	1.978	19.756 ± 0.201	3.18E-14	-
CXB302	3	3.21	269.670584	-27.902647	0.965	16.029 ± 0.005	3.18E-14	-3.32 ± 1.0
CXB308	3	2.86	269.525863	-27.783222	0.332	17.616 ± 0.034	3.18E-14	-2.81 ± 0.98
CXB310	3	3.36	269.513506	-27.574914	0.689	17.604 ± 0.034	3.18E-14	-
CXB334	3	3.71	268.888395	-29.030434	1.167	20.662 ± 0.163	3.18E-14	-
CXB342	3	1.84	268.702924	-29.363957	3.291	16.884 ± 0.021	3.18E-14	-
CXB354	3	2.93	268.377335	-29.684178	2.297	21.662 ± 0.406	3.18E-14	-
CXB417	3	3.1	263.076092	-30.364235	2.027	17.089 ± 0.018	3.18E-14	-3.26 ± 1.0
CXB419	3	5.4	262.924281	-30.597317	3.657	22.021 ± 0.339	3.18E-14	-
CXB421	3	2.09	262.89641	-30.30463	0.734	21.796 ± 0.341	3.18E-14	-
CXB422	3	1.95	262.820067	-30.321093	3.19	13.97 ± 0.002	3.18E-14	-4.26 ± 0.98

Table A.1: All 269 GALEX/Chandra matches in this work, with columns as follows: (1) Colloquial GBS name, (2) number of Chandra X-Ray counts, (3) Chandra X-Ray error, (4)+(5) RA and DEC of Galex counterpart, (6) offset between GALEX/Chandra positions, (7) GALEX magnitude in AB system, (8) X-Ray flux using 1.06×10^{-13} erg/s/cm²/photon conversion, (9) X-Ray to V flux ratio for systems with an observed V magnitude.